6/9-22-95 JSL

DE/ER61029-19

A SYSTEM FOR AERODYNAMICALLY SIZING ULTRAFINE ENVIRONMENTAL RADIOACTIVE PARTICLES

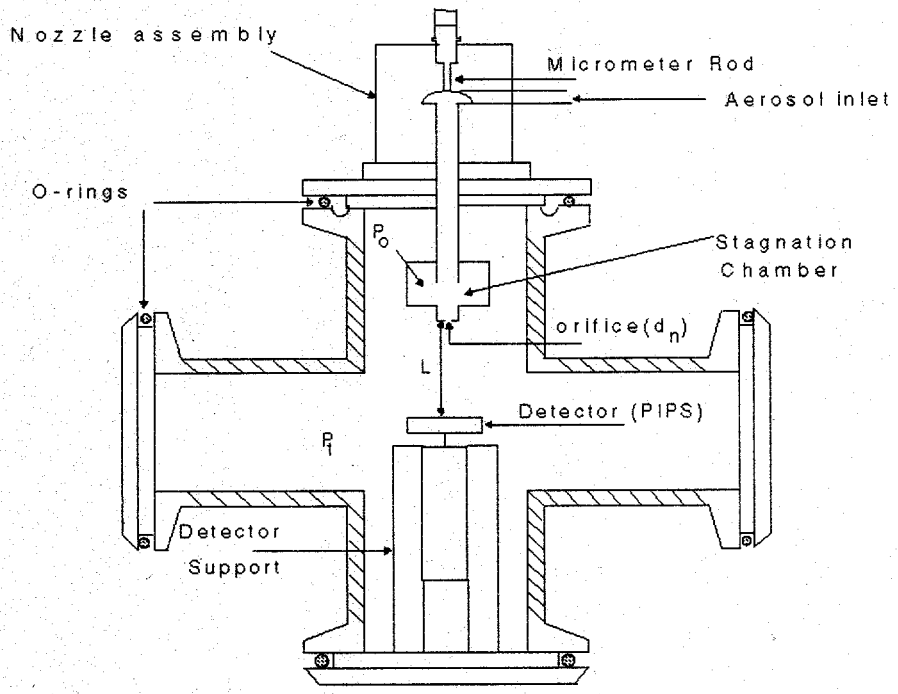

by

Olanrewaju Olawoyin
Department of Chemical Engineering
Clarkson University

September, 1995

DISCLAIMER

Portions of this document may be illegible in electronic image products. Images are produced from the best available original document.

ABSTRACT

A SYSTEM FOR AERODYNAMICALLY SIZING ULTRAFINE ENVIRONMENTAL RADIOACTIVE PARTICLES

Lanre Olawoyin, Ph.D.
Department of Chemical Engineering
Clarkson University, 1995
Professor P. K. Hopke, Advisor

The unattached environmental radioactive particles/clusters, produced mainly by ^{222}Rn in indoor air, are usually few nanometers in size. The inhalation of these radioactive clusters can lead to deposition of radioactivity on the mucosal surface of the tracheobronchial tree. The ultimate size of the cluster together with the flow characteristics will determine the depositional site in the human lung and thus, the extent of damage that can be caused. Thus, there exists the need for the determination of the size of the radioactive clusters. However, the existing particle measuring device have low resolution in the sub-nanometer range.

In this research, a system for the alternative detection and measurement of the size of particles/cluster in the less than 2 nm range have been developed. The system is a one stage impactor which has a solid state spectrometer as its impaction plate. It's major feature is the nozzle-to-plate separation, L. The particle size collected changes with L and thus, particle size spectroscopy is achieved by varying L. The number of collected particles is determined by alpha spectroscopy. The size-discriminating ability of the system was tested with laboratory generated radon particles and it was subsequently used to characterize the physical (size) changes associated with the interaction of radon progeny with water vapor and short chain alcohols in various support gases.

The theory of both traditional and high velocity jet impactors together with the design and evaluation of the system developed in this study are discussed in various chapters of this dissertation. The major results obtained in the course of the study are also presented.

First, the test results suggested that the system performance was fairly good. The cluster size estimated in ultra pure nitrogen (7 nm) agreed with the previously measured diffusion diameters and literature value. The cluster size measured in nitrogen was the same as the one in helium and purified air. However, the radon progeny was found to behave differently in oxygen.

In air with RH > 15%, it was found that the cluster size will be about 1 nm. In N_2 gas

with trace VOCs, the cluster size was found to increase with the hydrocarbon chain length. However, the cluster size was 1 nm in a similar environment in air, irrespective of the VOC present.

Lastly, the impactor was tested with radon progeny attached natural gas burner particles having a geometric mean of 13 nm and geometric standard deviation of 1.6. The estimated aerodynamic diameter and particle density were 18 nm and 1.38 g/cm^3, respectively.

ACKNOWLEDGEMENTS

First, I would like to acknowledge the invaluable contribution of Professor **Philip K. Hopke** to the successful completion of this work. If not for his counsel, encouragement and financial support, achieving the goals of this research would have been impossible.

I would also like to express my appreciation: to Drs **Babu, Rasmussen, Ahmadi** and **McLaughlin** for their time and help as members of my research committee; to **J. F. de la Mora** for helping in the system design and operation; to **Fred Englart**, for his assistance in constructing the system and his moral support; to **Dr R. F. Holub** for his numerous helpful suggestions regarding some of our experimental results; to **Dr Jurcik** and co workers for permission to reprint their simulation results presented in the journal of Aerosol Sci. and Tech. and to the US Departmental of Energy for funding this work under Grant DE FG02 90ER61029.

For the camaraderie of past and present members of Hopkes group, I particularly remember Mesbah B., Janis Borgia, S. K. Dua, Feng He, Alexandre Polissar, Hong Jia, Brian Fitzgerald and Yoshio Nomura. Also, I thank my parents, Daniel and Comfort Olawoyin, for their moral and financial support. Thanks for instructing me not to give up in difficult times.

Above all, my greatest gratitude goes to the omnipresent and omnipotent God for making this possible and for other things He has done for me. His love strengthens me.

TABLE OF CONTENTS

CHAPTER ONE

INTRODUCTION 1

CHAPTER TWO

BASIC CONCEPTS AND THEORY OF LOW PRESSURE PARTICLE IMPACTORS 8

2.1. Gas flow field for free and impinging jets 11

2.1.1. Free Jets 12

2.1.2 Impinging Jet 15

2.1.2.1 Mathematical model of gas flow with passive particle contaminants 16

2.1.2.2 Particle trajectories - Equations of motion 19

2.1.2.3 The "modified" Stokes Number, ψ 23

2.1.2.4. Computational Results 26

2.2. Summary remarks 30

CHAPTER THREE

HYPERSONIC IMPACTOR DESIGN AND TESTING 31

3.1. Stainless Steel Cross 32

3.1.1. Pirani vacuum gauge 36

3.2. Nozzle assembly 37

3.3. Collection assembly and the counting system 39

3.4. HI System Operating Procedure 43

3.5. Experimental System used for HI System Testing. 44

3.5.1 Radon chamber and its flow system. 46

3.6. Aerosol Generation and Sampling Procedure 49

3.7. Data Inversion - Procedure for estimating aerodynamic diameter 51

3.8 Sample Calculations 52

3.9 Summary Remarks. 54

CHAPTER FOUR

RESULTS AND DISCUSSION 55

4.1. System Test Results 55

4.2 Nature of Cluster Aerosol in various Support Gases. 60

4.2.1. Cluster Aerosol in Pure O_2 61

4.2.2. Cluster Aerosol in Purified Air 63

4.2.3. Cluster Aerosol in Pure He 64

4.3. Volatile Organic Compounds 66

4.3.1 Short-chain Alcohols 66

4.3.2 Classical Theory of Cluster Formation - Thomson Theory 68

4.3.3 VOCs in N_2 72

4.3.4 VOCs in Helium 79

4.3.5 Purified Air(4% RH at 22°C) 81

4.4. Summary Remarks 85

CHAPTER FIVE

FURTHER CHARACTERIZATION OF SYSTEM PERFORMANCE WITH TEST AEROSOL. 86

5.1. Experimental System 86

5.1.1 Differential Mobility Analyzer 88

5.2. Results and Discussion 92

5.3. Summary Remarks 94

CHAPTER SIX

CONCLUSIONS AND RECOMMENDATIONS 95

REFERENCES 97

APPENDIX A 104

TABLES

3.1: Detector specifications and performance data. 39
3.2: Specifications for the gases used in this study. 50
4.1: Properties of the VOCs used in this study. 67
4.2: Dominant ^{218}Po cluster sizes in N_2 with trace VOC. 74
4.3: Dominant ^{218}Po cluster sizes in N_2 with trace VOC and water 77
4.4: Comparison of the measured and calculated cluster sizes in air at various RH levels . . . 82
4.5: Comparison of the measured and calculated cluster sizes in air with trace VOC 83
5.1: Fraction of total particle concentration that carries +1,+2,+3,+4 and +6 elementary charges 89

FIGURES

2.1: Schematic diagram of a typical impaction stage showing streamlines and particle trajectories. 8
2.2: Typical efficiency curve for the impactors 9
2.3: Wave diagram of an under-expanded free jet. 11
2.4: Wave diagram of an under-expanded impinging jet 11
2.5: Plots of (a) equation (2.10) (b) equation (2.11) and (c) equation (2.12) 14
2.6: Plots of density and temperature ratios as a function of the mach number before the shock15
2.7: Calculated aerodynamic diameter for an inertial impactor stage with D=0.1 cm for several values of S/D for a constant pressure ratio χ = 0.2 (Jurcik *et al.* 1989 - Used with permission) 27
2.8: Calculated aerodynamic diameter as a function of downstream P_o, for several values of χ and S/D=0.8 (Jurcik *et al.* 1989 - Used with permission) 28
2.9: Calculated aerodynamic diameter as a function of upstream P_o, for several values of χ and S/D=0.8 (Jurcik *et al.* 1989. Used with permission) 28
2.10: Calculated gas flow field for an inertial impactor stage with S/D=0.8 and χ=0.2. The solid lines denote typical particle trajectories for a particle size that is approx. 50% collected. (Jurcik *et al.* 1989 - Used with permission) 29
2.11: Calculated gas flow field for an inertial impactor stage with S/D=2.5 and χ=0.2 (Jurcik *et al.* 1989 - Used with permission) 29
3.1: Cross-sectional view of the Hypersonic Impactor 33
3.2: Photograph of the HI system with the stainless steel cross connected to the vacuum gauge and pump, and the aerosol inlet pipe connected to the radon chamber. 34
3.3: Cross-sectional view of the Stainless Steel Cross 35
3.4: Gauge head 36
3.5: Cross-sectional view of the nozzle assembly 38
3.6: Cross-sectional view of the collection assembly 40
3.7: The typical -spectrum of Po-218 and Pb-214 of the HI system. 42
3.8: Impactor curve with single step 44
3.9: Impactor curve with several steps 44
3.10: Experimental System 45
3.11: Photograph of the radon/aerosol chamber 47
3.12: Schematic diagram of the condensation nucleus counter 47
3.13: The diffusion cell 49
3.14: Plot of aerodynamic diameter, d_{ae} against $L_{1/2}/d_n$ for d_n=0.02 mm, γ=1.4, P_o=1 atm, c_o=340 m/s. 53
4.1: Collection efficiency for ^{218}Po particle/cluster in a 99.999% pure N_2 , d_n=0.35 mm and P_o/P_1~ 800. 56
4.2: Response curve for ^{218}Po particle/cluster in a 99.998%N_2 , d_n=0.35 mm, P_o/P_1~800 and RH=25% 57
4.3: Normalized impactor response curve for ^{218}Po particle/cluster in a N_2 environment at various RH, d_n=0.2 mm and P_o/P_1~1000. 59
4.4: Response curve for cluster aerosol in O_2, d_n=0.2 mm and P_o/P_1~1600 61
4.5: Response curve for cluster aerosol in N_2 with trace NO, d_n=0.2 mm and

P_o/P_1~1600. 62
4.6: Impactor response curve for cluster aerosol in purified air, d_n=0.2 mm and P_o/P_1~1600. 64
4.7: Response curve for cluster aerosol in prepurified helium, d_n=0.2 mm and Po/P_1~760. 65
4.8: Variation in G as a function of cluster radius r for water, G=G1+G2+G3 71
4.9: Response curve for cluster aerosol in N_2(99.998%) with 0.58 ppm methanol, d_n = 0.2 mm and P_o/P_1~1000 73
4.10: Response curve for cluster aerosol in N_2(99.998% pure) with 0.2 ppm butanol, d_n =0.2 mm and P_o/P_1~1000. 73
4.11: Response curves for cluster aerosol in N_2 with various CH_3OH-H_2O concentration ratio (a:0.7; b:1.28; c:6.4) 75
4.12: Response curve for cluster aerosol in N_2 (99.998% purity) with trace ethanol and water ([C_2H_5OH]/[H_2O]=7), d_n = 0.2 mm and Po/P_1 1000. 77
4.13: Response curve for cluster aerosol in N_2 (99.9985 purity) with trace propanol and water ([C_3H_7OH]/[H_2O])=1.75), d_n=0.2 mm and P_o/P_1~1000. 78
4.14: Response curve for cluster aerosol in N_2 (99.998% pure) with trace n-butanol and water ([C_4H_9OH]/[H_2O]=1.25), d_n=0.2 mm and P_o/P_1~1000. 78
4.15: Response curve for cluster aerosol in N_2 (99.998% pure) with trace 2-Butanol and water ([2-C_4H_9OH]/[H_2O]=2.0), d_n=0.2 mm and P_o/P_1~1000. 79
4.16: Response curves for helium gas with trace amounts of (a) 0.1 ppm methanol (b) 0.15 ppm ethanol (c) 0.11 ppm propanol. 80
4.17: Plot of peak ratio against concentration ratio 85
5.1: System for generating, radiolabeling, and sampling of gas burner particles. 87
5.2: Flow Schematic for the Electrostatic Classifier 89
5.3: The size distribution of the gas burner particles 92
5.4: The fitted response curve to the experimental data. 93

Chapter ONE

INTRODUCTION

Particle size is the most important parameter for characterizing the behavior of aerosols. The particle size of interest in aerosol behavior range from molecular clusters of 0.5 nm to fog droplets and dust particles larger than 100 μm. This range represents a variation of 10^5 in size and of at least 10^{15} in mass.

Particle size can be characterized based on the technique used to measure it. This operational definition approach leads to such size types as aerodynamic diameter, optical-equivalent diameter, electrical-mobility-equivalent, diffusion-equivalent diameter and so on. Generally, four methods of aerosol size measurement methods are commonly used: (1) light-scattering (2) impaction (3) microscopy (4) diffusion-based (Baron and Willeke, 1993). The optical particle counter and surface analysis measurements are quite useful in contamination control work, as the damage done by particles in the semiconductor industry is often related to their number concentration and size. Impactor and diffusion measurements are quite useful in health-related assessments, as the risk posed by particles is often related to both the diffusion and aerodynamic diameters since they govern deposition of particles within the human respiratory system.

From the standpoint of health and environmental effects, particles in the sub to few nanometer size range are of growing importance both in the atmosphere and indoor air. These particles are normally formed in the atmosphere by the action of cosmic radiation, while radioactive gases like radon, and combustion products, are major sources in indoor air. On deposition in the respiratory tract, the radon gas decay products emit ionizing radiation during their decay. .

It has become recognized that inhalation exposure in buildings to the radioactive progeny of radon is responsible for a major portion of the effective radiation dose to the public (Sinnaeve *et al.* 1984). In the general population, the estimated risk of lung cancer attributable to indoor radon exposure is much larger than the cancer risk attributable to exposure to most other environmental contaminants (Nazaroff and Nero, 1988).

Radon and Radon Progeny in Indoor Air

Based on the studies in the past fifteen years, it is certain that the radon in most of the ordinary home comes from soil under the influence of a pressure differential between the interior of the house and surrounding soil (Nazaroff and Nero, 1988). Water from wells and natural gas are other sources of indoor radon. In addition to the pressure differential between the inside and outside, the infiltration rate of radon into indoor air is controlled by the permeability of the soil and the emissivity of radon from the soil grains. Negative sub-slab depressurization is widely used to effectively reduce the concentrations of radon in indoor air. Compared to indoor air, the outdoor air concentration of radon is small and it ranges from 4 to 15 Bq m^{-3}; the median outdoor level is 14.8 Bq m^{-3} (Hopper *et al.* 1991) while the annual average indoor radon level is 46.3 Bq m^{-3} (Marcinowski *et al.* 1993). Between 1.7 and 2.5 million homes, that is 2 to 3% of the 85 million homes in the United States, could potentially have indoor radon concentrations above 300 Bq m^{-3} (EPA,1992).

Radon itself is an essentially a chemically inert gas with half life of 3.84 days. It does not pose a significant radiation health hazard to humans because of its low retained fraction in the body. Radon has four important decay products, polonium-218 (^{218}Po, RaA, $t_{1/2}$=3.11 min), lead-214 (^{214}Pb, RaB, $t_{1/2}$=19.8 min), bismuth-214 (^{214}Bi, RaC, $t_{1/2}$=26.8 min), and polonium-214(^{214}Po, RaC', $t_{1/2}$=162 μs). These short-lived radon progeny can exist in both neutral and charged species. They can also exist in both "unattached" and "attached" states. The latter is the fraction that has become attached to any available particle surface. Unlike in the other studies, the nuclei present in the "unattached" fraction, mostly ^{218}Po, are referred to as ultrafine particles, and their sizes fall in the range < 2 nm. They have much higher mobilities in the air and can effectively deposit in the respiratory system.

In the presence of indoor atmospheric trace species like volatile organic compounds, VOCs, (Berglund *et al.* 1986) and semi volatile organic compounds, SVOC, (Wilson, 1987), the radon progeny can interact and undergo reaction or clustering that lead to a change in their physical or chemical state. This modified state governs their transport and removal processes (Castleman, 1991).

The hazard caused by the inhalation of radioactive radon progeny particles depends on the region in which they deposit. The mechanisms for particle deposition in

human airways is similar to that involved in the collection of particles in a filter. It is a function of the particle size and the flow characteristics in the various sections of the airways (Schlesinger and Lippmann, 1972; Chan and Lippmann, 1980; Egan and Nixon, 1989). In order to model or estimate the particle deposition pattern in respiratory tract, it is necessary to have full particle size distribution information. However, the initial size distributions are not sufficient since the sizes of airborne particles can change with the nature of their environment (Li and Hopke, 1993) but it is a very essential starting point for dose assessment. For example, the increased relative humidity and temperature in the respiratory tract may cause a significant increase in particle size because of the absorption of water vapor onto the particle providing that the particle contains water soluble species (Ferron, 1977; Martonen *et al.* 1982; Anselm *et al.*, 1986).

Size Distribution Measurements

Because of the growing concern about the indoor air quality, several attempts have been made to measure the size distribution in order to understand the ultrafine particles mode properties, both physical and chemical. All of these measurements can be broadly categorized into three, namely diffusion-based (Frey *et al.* 1981), electrical mobility-based (Strydom *et al.* 1990) and mass spectrometry (Castleman, 1982).

Using the two-filter method described by Thomas and LeClare (1970), Frey *et al.* (1981) measured the diffusion coefficient of ^{218}Po in N_2 with trace concentration of nitric oxide and in O_2. However, recent mathematical analysis by Sasse *et al* (1994) suggested about 10-20% error in the Frey *et al* estimated D values. Most other diffusion-based measurements have been done for $^{212}Pb^{+}$ cluster in purified air at various relative humidity (Su *et al.* 1988). The main problem with the resolution of the estimated size distribution from the measured D values is in data inversion. A particle's diffusion coefficient is non-unique in the presence of both charged and neutral species. Depending on it's charge state (neutral, ± 1, 2, etc), a particle of a specific mass and size may have more than one diffusion coefficient (Ramamurthi *et al.*, 1993). In addition, the diffusional nature of these instruments results in poor resolution for sub-nanometer particles because of the inherent limitations of particle diffusion. For example, the commercially available screen diffusion battery (DB) suffers from negligible penetration of highly diffusive ultrafine particles in the 0.5-5 nm size range, even past the first DB

stage.

Mobility analyzers were used by Yoon *et al* (1992) to measure SO_2 effects on the ^{218}Po ion mobility spectrum and by Styrdom *et al* (1990) for measurement of the initial properties of ^{218}Po in purified air with well defined amounts of water vapor. Compared to diffusion-based measurements, better particle size distribution resolution has been achieved with electrical mobility-based measurements, but it is only applicable to charged particles. Only less than 1% of the aerosol particles less than 10 nm can be charged. This makes mobility analyzers unsuitable for neutral ultrafine radioactive particles. However, mass spectroscopy (Castleman, 1982) performed at atmospheric pressure permits higher resolution than the mobility analyzer but the limits of detection are too high to permit measurement of ^{218}Po ions at the low mass concentration, but the high radioactivity concentrations of $^{218}Po^{+}$ that can be easily produced in the laboratory. In addition, the instrumentation for mass spectroscopy is very expensive

The above-mentioned problems could be circumvented by characterizing the ultrafine particles by their aerodynamic diameter, which is an indirect measure of their inertia. Aerodynamic diameter of a particle of arbitrary shape and density refers to the size of a spherical particle of unit density with the same settling velocity as the particle in question. Also, knowing the particle aerodynamic size as well as the volume equivalent diameter, both the mass and density of the particles can be estimated. Thus, attempts were made in this study to determine the aerodynamic diameter of these ultrafine particles using a highly supersonic (hypersonic) aerosol impactor as a size discriminating instrument. To achieve this purpose, a hypersonic impactor, which was patterned after that of de la Mora *et al.* (1990a), was designed and built.

A hypersonic jet is formed by the expansion of aerosol from atmospheric pressure into a chamber kept at a few tenths of torr. de la Mora *et al.* (1990a&b) designed and built the first hypersonic impactor, and subsequently used it to collect particles > 2 nm. However they did not test it for particle sizes less than 2 nm, because of the difficulties in generating the required monodisperse test aerosol. Not only will this study elucidate the techniques involved in the generation and hypersonic impaction of < 2 nm particles but it will also examines its limitations.

Aerosol Impactors, Subsonic and Supersonic

For many years, aerosol impactors, devices used for the inertial separation of airborne particles, have been widely used for collecting airborne particles for chemical or gravimetric analysis. Such impactors have been used extensively in air pollution and industrial hygiene studies to determine the particle size distribution of the airborne particulate matter. In an aerosol impactor, a jet of particle-laden air is directed at a plate to cause impaction of particles on the plate. If an impactor is properly designed, nearly all particles larger than a certain size will impact while smaller will pass through without impaction (Marple and Willeke, 1979).

Subsonic

Since the pioneering work of May (1945), a large number of studies have been made on the various types of impactors. Most of the studies have been on impactors with incompressible jets (Lodge and Chan, 1986) and only a few studies are available on particle impactors operating in supersonic streams (Serafini, 1954; Hering *et al.*, 1979; Flagan, 1982; Biswas and Flagan, 1984; Forney and McGregor, 1987; Ishii *et al.*, 1989). The major interest of these studies was focused on the effects of the flow and geometric conditions on the collection efficiency curve.

Davies and Aylward (1951) obtained theoretical solutions of the flow fields using the assumption of the potential flow while Ranz and Wong (1952) and Mercer and Stafford (1969) assumed a simplified flow field that made it possible to obtain an analytical solution to the particle momentum equation. For the same incompressible jet, Marple *et al.* (1974) presented a more rigorous digital computation of the numerical solution of Navier-Stokes equations. Using the flow field computed by Marple *et al.* (1974), Marple and Liu (1974) investigated some parameters affecting the operation of the inertial impactor, such as Reynolds number, nozzle-to-plate distance, and nozzle throat length.

As a result, Marple and Liu (1974) and later, Biswas and Flagan (1984) pointed out that impactors operating under moderate Reynolds numbers or sonic conditions showed unsatisfactory instrument characteristics, apparently implying that the smallest size of particles that can sharply be inertially separated is determined solely by the fluid dynamical considerations.

However, rather steep capture efficiency curves have been measured experimentally in compressible (Wang and John, 1988) and even in slightly supersonic impactors (Kauppinen and Hillamo, 1989). The numerical computations of Jurcik *et al.* (1989) and Ishii *et al.* (1989) have led to similar results for supersonic impactors.

Supersonic

After proving otherwise the claim made by early workers that high velocity jets have deleterious effect on impactor performance, investigators started exploring sonic and hypersonic impaction due to the desire to develop schemes to produce sharp size-separation of particles and macromolecules with diameters of only a few nanometers. The flow regime with Mach number, M greater than 6, there exist large discrepancies between the behavior of a real and a perfect gas. This regime is called hypersonic flow. Conversely, for $1 < M < 6$, the flow is said to be supersonic and fluid can be assumed to obey the perfect-gas law.

Generally, operation of impactors based on highly supersonic jets is substantially different from their subsonic counterpart. Supersonic or hypersonic impactor operation has been studied numerically by Jurcik *et al.* (1989) and experimentally by de la Mora *et al.* (1990b). The latter developed and tested an hypersonic impactor with aerosol particles of size > 2 nm.

The major feature of an hypersonic impactor is that its collection efficiency, E, for a particular particle size is a function of the nozzle-to-plate distance, L. The reason for this phenomenon is that as L increases, the central compression shock waves (the Mach disk) moves further downstream, and the pressure at the stagnation point decreases. Thus, the particle will be accelerated to a higher velocity before the central compression shock and the drag force is thereby decreased in the wall region as L increases allowing smaller particles to impact. The impactor was found, however, to show sharp separation efficiency curves only when L is smaller than a critical distance, L^*.

Since the system developed in this study, a hypersonic impactor, is a low pressure impactor, the basic concepts and the theory of fluid dynamics of both free and impinging jets in low pressure region are reviewed in chapter 2. First, the general structure of the highly underexpanded free and impinging jets are described. Then, the system of equations governing the impaction process as well as the mathematical relations for

temperature, pressure and density as functions of the local Mach number and the nozzle-to-plate distance are presented. These system of equations are derived based on the assumption that the particles are passive contaminant in the gas, i.e., the gas flow is not affected in any way by the presence of particles but not vice-versa. The numerical results obtained in earlier studies together with the modifications to Stokes number, the parameter governing the impaction process in incompressible flow, is also detailed in chapter 2. The numerical results clearly show the important design parameters utilized in the design of the hypersonic impactor (Chapter 3).

Chapter 3 presents the detailed design of the various parts of the hypersonic impactor (henceforth referred to as "HI") developed in this study. The systems parts include the nozzle, collection and counting assemblies. The operating procedure and the experimental system used for the HI testing and evaluation are also described. Also presented in chapter 3 are the aerosol generation, sampling, and data inversion procedures. The results of system test and other results obtained in the course of this study are subsequently presented in Chapter 4.

Furthermore, chapter 4 discusses the results of the experimental studies. This work include the results of the experimental investigation of the interaction of radon progeny with commonly found indoor pollutants in various carrier gases.

Chapter 5 presents the results on the further characterization of system performance with gas burner particles; which are radiolabeled with radon progeny in order to make them radioactive. The size distribution of the gas burner particles were determined prior to sampling with the impactor. The major achievements and important findings of this study are presented in Chapter 6.

Chapter
TWO

BASIC CONCEPTS AND THEORY OF LOW PRESSURE PARTICLE IMPACTORS

Impactors are samplers that provide a density-dependent measure of particle "size", known as the aerodynamic diameter, different from that of mobility analyzers, diffusion batteries, or microscopes. The aerodynamic diameter is defined as the diameter of unit-density (1 g cm^{-3}) sphere that has the same gravitational settling velocity as the particle in question.

Generally, the most common type of impactor consist of a single jet of particle-laden gas (aerosol) impinging upon a flat plate, as shown in Figure 2.1. Particles larger than the cut-size of the impactor will slip across the streamlines and impact upon the plate while the smaller particles will remain in suspension.

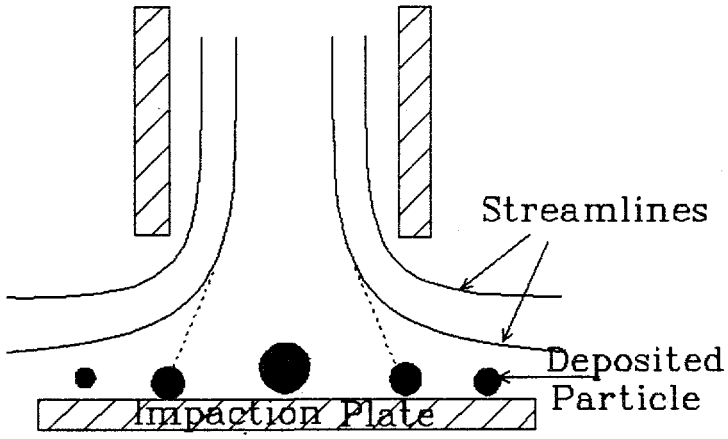

Figure 2.1: Schematic diagram of a typical impaction stage showing streamlines and particle trajectories.

The most important characteristic of an impactor is the collection efficiency. It is defined as the fraction of particles passing through the nozzle that are collected upon the impaction plate. An example of an impactor's efficiency curve is shown in Figure 2.2. The ideal impactor has a perfectly sharp efficiency curve, i.e., all particles larger than a critical diameter are collected while smaller particles remain in suspension.

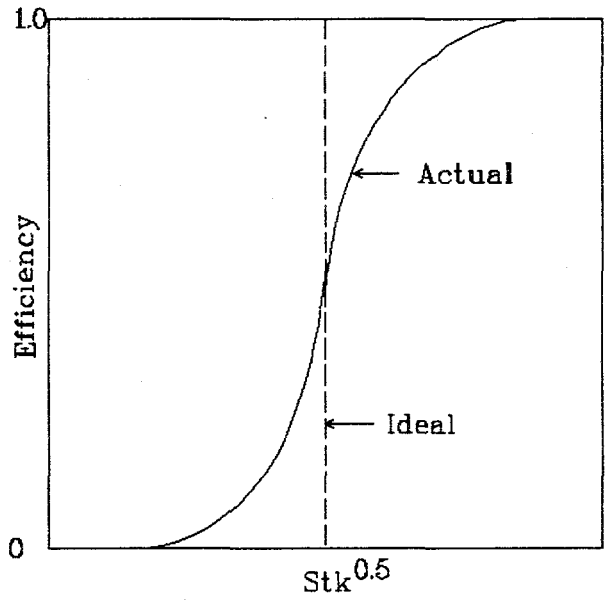

Figure 2.2: Typical efficiency curve for the impactors

Particle collection in an inertial impactor is governed by the Stokes number, a dimensionless parameter defined as (Lodge and Chan, 1986):

$$S = \frac{\rho_p d_p^2 V_j C_c}{18 \mu d_j} \qquad (2.1)$$

where ρ_p is the particle density; d_p is the particle physical diameter; V_j is the jet velocity; μ is the carrier gas viscosity; d_j is the jet diameter and C_c is the Cunningham slip correction factor given by Friedlander (1977) as:

$$C_c = 1 + \frac{\lambda}{d_p}[2.514 + 0.8\exp(-0.55 d_p/\lambda)] \qquad (2.2)$$

and λ is the mean free path, a measure of the distance between the carrier gas molecules. Note that the current form and constants of the Cunningham equation (Equation 2.2) were determined empirically from a compilation of experimental data (Davies, 1945) to fit the range of values of d_p/λ from the continuum to the free molecular regimes. Equation (2.2) is true for air only and for $d_p > 2$ nm. Ramamurthi *et al.* 1993 has modified the above equation (2.2) to make it valid for $d_p < 2$ nm by substituting

$$d_p^* = d_p\left(1 + 3e^{-2.20 \times 10^7 d_p}\right) \qquad (2.3)$$

for d_p in the equation. Note that dp in equation (2.3) is in cm.

In the continuum regime, $d_p > \lambda$, $C_c = 1$ while in the free molecular region, $d_p < \lambda$, C_c is usually large and is inversely proportional to d_p. For other carrier gases, equation (2.2) is accurate to within 3% in the molecular regime ($2\lambda/d_p > 20$) and to within 5% over the transition regime (Rader, 1990).

For a particle to be collected on a plate, the Stokes number, S, has to be greater than a critical value. An analysis of equations (2.1) and (2.2) reveals that a particle's Stokes number, S, can be increased by either increasing the value of the slip correction, C_c (i.e., by operating the impactors at low pressure), or by decreasing the nozzle diameter. Impactors utilizing these techniques are known as either low-pressure impactors or micro-orifice impactors, respectively.

Low pressure impactors make use of sonic jets for the separation and collection of small particles (de la Mora *et al.* 1990). At the low pressure, the particle Knudsen number ($Kn = 2\lambda/d_p$) is much greater than 1 so non-continuum effects become important in determining the drag force exerted by the gas on a particle. The low pressure and the non-continuum effects reduce the drag force on the particle. This reduction in drag allows smaller particles to be collected in low pressure impactors than is the case for impactors operated at atmospheric pressures.

A study of particle impaction at low pressure is of great importance in many engineering fields. Low pressure impactors have been successfully used for atmospheric, in-stack sampling and in the recovery of UF_6 particles produced in molecular laser isotope separation of uranium (Koga *et al.* 1989). Several other applications also make use of deposition of sonic and supersonic jets of fine particles on surfaces for thin film formation (Fukushima *et al.* 1985) and for fine line pattern formation by aerosol etching (Chen *et al.* 1987 and 1988).

This chapter presents the description of the physical system and the mathematical model of the impaction process and the various numerical methods for solving the equations describing the model. The computational results and the modified Stokes number used to characterize the collection efficiency in low pressure impactors are also presented.

2.1. Gas flow field for free and impinging jets

Figure 2.3 shows a wave diagram for an under-expanded free supersonic jet, while Figure 2.4 depicts a wave diagram for an underexpanded impinging jet. It is common practice in supersonic flows to characterize the gas flow field by the gas reservoir conditions and the local gas Mach number (Leipmann, 1957; Shapiro, 1953).

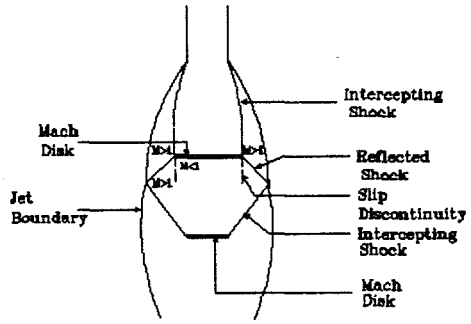

Figure 2.3: Wave diagram of an under-expanded free jet.

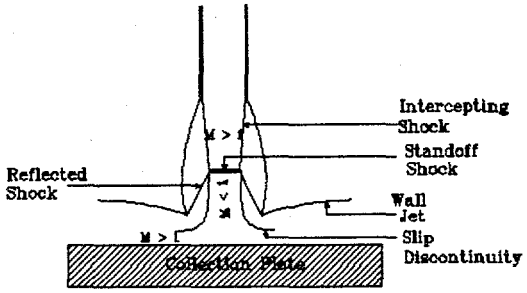

Figure 2.4: Wave diagram of an under-expanded impinging jet

2.1.1. Free Jets

For a free jet, the gas expands to ambient pressure along the jet boundary which bends back towards the axis downstream of the nozzle. Compression waves are reflected from the jet boundary and coalesce to form the hanging or intercepting shock. The flow is supersonic on both sides of the oblique intercepting shock. These intercepting shocks meet at the axis for slightly underexpanded jets where reflected shocks are formed. The reflected shocks intercept the jet boundary and the process is repeated. For higher pressure ratios, the intercepting shocks intersect a normal shock (a Mach disk) as shown in Figure 2.3. At the intersection of the intercepting shock and the Mach disk, a reflected shock is formed and the process repeats itself as before.

Two common types of free jets, slit (rectangular) and round jets, have been previously investigated. The equations and wave describing both jets are similar. The flow field of slit free jets with aspect ratios greater than 50 had been investigated previously (Beylich, 1981; Dupeyrat and Devillers, 1978; Teshima, 1987). For large downstream distances, the expansion from an infinitely long slit leads to the following asymptotic expressions for $L_{ns}/W \gg 1$, L_{ns} and W are the length and width of the nozzle, for temperature, T, pressure, P, and density, ρ (Beylich, 1981):

$$\frac{T}{T_n} = \left(\frac{\gamma+1}{\gamma-1}\right)^{-(\gamma-1)/2} \left(\frac{L}{d_n}\right)^{(-\gamma+1)} \tag{2.4}$$

$$\frac{P}{P_n} = \left(\frac{\gamma+1}{\gamma-1}\right)^{-\gamma/2} \left(\frac{L}{d_n}\right)^{-\gamma} \tag{2.5}$$

$$\frac{\rho}{\rho_n} = \left(\frac{\gamma+1}{\gamma-1}\right)^{-0.5} \left(\frac{L}{d_n}\right)^{-1} \tag{2.6}$$

The subscript n refers to the properties at the orifice exit. These properties can be related to the upstream stagnation conditions for isentropic flows of a perfect gas of specific heat ratio, γ, as follows (Shapiro, 1957):

$$\frac{T_o}{T_n} = 1 + \frac{\gamma - 1}{2} M_n^2 \tag{2.7}$$

$$\frac{P_o}{P_n} = \left(1 + \frac{\gamma - 1}{2} M_n^2\right)^{\gamma/(\gamma-1)} \tag{2.8}$$

$$\frac{\rho_o}{\rho_n} = \left(1 + \frac{\gamma - 1}{2} M_n^2\right)^{1/(\gamma-1)} \tag{2.9}$$

By combining equations (2.4) through (2.9) one can obtain the gas properties for isentropic expansion from sonic slit nozzles (M_n=1) up to the locations of the Mach disk, L_m.

$$\frac{T}{T_o} = \left(\frac{2}{\gamma+1}\right)\left(\frac{\gamma+1}{\gamma-1}\right)^{\frac{\gamma-1}{2}}\left(\frac{L}{d_n}\right)^{-(\gamma-1)} \tag{2.10}$$

$$\frac{P}{P_o} = \left(\frac{2}{\gamma+1}\right)^{\gamma/(\gamma-1)}\left(\frac{\gamma+1}{\gamma-1}\right)^{-\gamma/2}\left(\frac{L}{d_n}\right)^{-\gamma} \tag{2.11}$$

$$\frac{\rho}{\rho_o} = \left(\frac{2}{\gamma-1}\right)^{1/(\gamma-1)}\left(\frac{\gamma+1}{\gamma-1}\right)^{-1/2}\left(\frac{L}{d_n}\right)^{-1} \tag{2.12}$$

Equations (2.10)-(2.12) are plotted in Figure 2.5. Using these expressions and assuming the pressure behind the Mach disk is equal to the background pressure, P_b, Dupeyrat and Devillers(1978) derived the theoretical locations of the Mach disks, L_m, for axisymmetric free jet, for a nozzle d_n, to be:

$$\frac{L_m}{d_n} = 0.65\left(\frac{P_o}{P_b}\right)^{0.5} \tag{2.13}$$

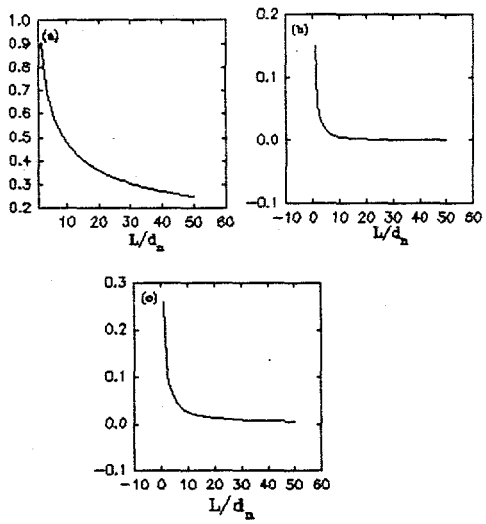

Figure 2.5: Plots of (a)equation **(2.10)** (b)equation **(2.11)** (c) equation **(2.12)**

Equation (2.13) agrees with the following empirical formula determined from experimental data taken over a wide range of parameters (Ashkenas and Sherman, 1966):

$$\frac{L_m}{d_n} = 0.67\left(\frac{P_o}{P_b}\right)^{0.5} \tag{2.14}$$

For normal shock, the ratio of gas properties across the shock wave in terms of the gas Mach number ahead of the shock, M_1 are (Forney and McGregor, 1987):

$$\frac{\rho_1}{\rho_2} = \frac{(\gamma-1)M_1^2+2}{(\gamma+1)M_1^2} \tag{2.15}$$

$$\frac{T_2}{T_1} = \frac{2(\gamma-1)\left[1+\frac{\gamma-1}{2}M_1^2\right]\left[\frac{2\gamma}{\gamma-1}M_1^2-1\right]}{(\gamma+1)^2M_1^2} \tag{2.16}$$

where subscripts 1 and 2 refer to the gas properties ahead of and behind the shock, respectively. The plots for equations (2.15) and (2.16) are shown in Figure 2.6 as solid (1) and broken (2) lines respectively.

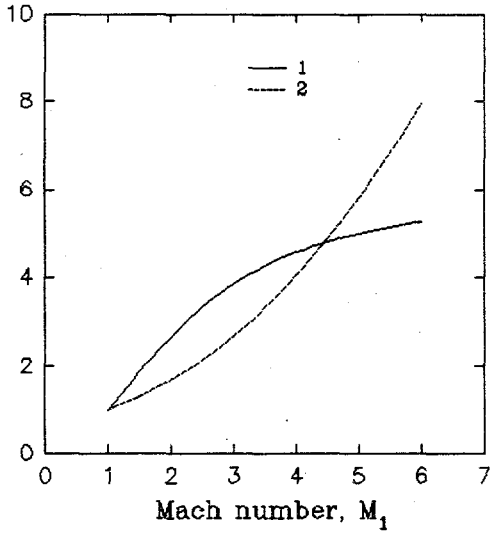

Figure 2.6: Plots of density (solid line) and temperature ratio (broken line) as a funtion of the mach number before the shock.

2.1.2 Impinging Jet

An underexpanded impinging jet shown in Figure 2.4. is formed if the impaction plate is located well ahead of where the shock (Mach disk) will form in its absence. The upstream source region contains a gas at a constant stagnation pressure, P_o. The gas expands through a nozzle into an evacuated region which is held at a constant pressure, P_1. An effectively infinite plate is perpendicular to the jet axis at a distance L from the nozzle exit.

At the nozzle exit, the gas velocity is sonic if the ratio of the upstream pressure to the downstream pressure is greater than 0.5. The gas flow expands to supersonic velocities in the core of the jet upstream of a strong standoff shock. After passing through the strong standoff shock, the gas flow decelerates abruptly to subsonic velocities on either side forming a wall jet. The flow between the jet boundary and internal barrel shock is also supersonic. It passes through a reflected shock (formed by the interaction of the internal barrel shock and the strong standoff shock) and expands into a supersonic region separated by a slip discontinuity from the subsonic region behind the strong standoff shock. For hypersonic flow, $M > 6$, the kinetic

energy of the gas particles is large compared to their thermal energy. For fixed values of the state parameters, the ratio of the kinetic to the internal energy in the freestream increases in proportion to the square of the Mach number, M. This fact leads to the appearance of some properties in steady hypersonic flow which are different from those flows at moderate and low velocities where the kinetic energy of the gas particles is of the same order, or lower than, the thermal energy. Thus, when a gas particle is decelerated adiabatically in a steady hypersonic flow, the conversion of its kinetic energy into heats results in a very considerable increase in the gas temperature. It then follows that relatively small perturbations in the velocity are connected with relatively large perturbations in the density, temperature, and speed of sound. Hence, in a hypersonic flow, the Mach number changes as a result of the change in the speed of sound. The system of equations describing compressible flow past a collection plate is presented in the next section.

2.1.2.1 Mathematical model of gas flow with passive particle contaminants

With neglect of viscosity effects and assuming the ideal gas law, the equations describing the fluid dynamics of the axisymmetric impinging jet shown in Figure 2.4 are the Euler equations of gas dynamics. The dimensionless equations governing the fluid dynamics of the impinging jet are as follows:

$$\frac{\partial e}{\partial \bar{t}} + \frac{\partial f(e)}{\partial \bar{z}} + \frac{\partial g(e)}{\partial \bar{r}} + \frac{h(e)}{\bar{r}} = 0 \tag{2.17}$$

where

$$e = \begin{bmatrix} \bar{\rho} \\ m \\ n \\ q \end{bmatrix} \quad f(e) = \begin{bmatrix} m \\ \frac{m^2}{\bar{\rho}} + \bar{\rho}\bar{T} \\ \frac{mn}{\bar{\rho}} \\ (q + \bar{\rho}\bar{T})\frac{m}{\bar{\rho}} \end{bmatrix} \quad g(e) = \begin{bmatrix} n \\ \frac{mn}{\bar{\rho}} \\ \frac{n^2}{\bar{\rho}} + \bar{\rho}\bar{T} \\ (q + \bar{\rho}\bar{T})\frac{n}{\bar{\rho}} \end{bmatrix} \quad h(e) = \begin{bmatrix} n \\ \frac{mn}{\bar{\rho}} \\ \frac{n^2}{\bar{\rho}} \\ (q + \bar{\rho}\bar{T})\frac{n}{\bar{\rho}} \end{bmatrix} \tag{2.18}$$

and

$$m=\bar{\rho}\bar{u} \quad n=\bar{\rho}\bar{v} \quad q=\bar{\rho}(\bar{T}/(\gamma-1)+(\bar{u}^2+\bar{v}^2)/2) \tag{2.19}$$

All the variables used in the above equations are nondimensioned as follows:

$$\bar{\rho}=\rho/\rho_n,\ \bar{u}=u/u_n,\ \bar{v}=v/u_n,\ \bar{T}=R_g/u_n^2,$$
$$\bar{t}=tu_n/R,\ \bar{r}=r/R,\ \bar{z}=z/R$$

Here, t, r, z, R and R_g are the time, radial coordinate, axial coordinate, orifice radius and gas constant respectively; t, T, u, v are the time, temperature; axial velocity and radial velocity. The governing differential equations are subject to the following boundary equations:

Inflow Boundary Conditions (z=0; 0≤ r≤1).

$$\begin{aligned}\bar{\rho}&=1\\ \bar{u}&=1\\ \bar{v}&=0\\ \bar{T}&=\frac{1}{\gamma M^2}\end{aligned} \tag{2.20}$$

Centerline(r=0; 0≤z<L/R)

$$\begin{aligned}\frac{\partial\bar{\rho}}{\partial\bar{r}}&=0\\ \frac{\partial\bar{u}}{\partial\bar{r}}&=0\\ \bar{v}&=0\\ \frac{\partial\bar{T}}{\partial\bar{r}}&=0\end{aligned} \tag{2.21}$$

Outflow $(r=R_d/R;\ 0 \le z < L/R)$

$$\begin{aligned} \frac{\partial \bar{\rho}}{\partial \bar{r}} &= 0 \\ \frac{\partial \bar{u}}{\partial \bar{r}} &= 0 \\ \frac{\partial \bar{v}}{\partial \bar{r}} &= 0 \\ \frac{\partial \bar{T}}{\partial \bar{r}} &= 0 \end{aligned} \qquad \textbf{(2.22)}$$

Impaction Surface $(z=L/R;\ 0 \le r < R_d/R)$

$$\begin{aligned} \frac{\partial \bar{\rho}}{\partial \bar{z}} &= 0 \\ \bar{u} &= 0 \\ \frac{\partial \bar{v}}{\partial \bar{z}} &= 0 \\ \frac{\partial \bar{T}}{\partial \bar{z}} &= 0 \end{aligned} \qquad \textbf{(2.23)}$$

where L is the dimensioned distance between the orifice and the detector, and R_d is the radius of the detector which serves as the collection plate.

The solution to equations (2.17) through (2.23) is not single-valued (Courant and Friedrichs, 1957) at least at some distance from the collection plate. The solution can be made single-valued if appropriate discontinuity surfaces are introduced. Even in this case, the uniqueness of the solution is not guaranteed since the discontinuity surfaces can be chosen differently. But the solution of a correctly formulated physical problem must be unique and correspond exactly to the phenomena which result from the given physical conditions. Also, the fact that a generalized solution of the equations of motion of an ideal gas has physical sense when it represents the limit of a continuous solution of the differential equations of motion of a viscous gas, is of fundamental importance in selecting the required solution from all possible generalized solutions. Consequently, dissipative terms containing a small parameter are added to the differential equations defined above. The dissipative terms which are introduced need not

describe the actual viscous and heat conductive processes. It is only important that in the limit, when the small parameter tends to zero, the solution should reduce to the generalized solution obtained if viscosity and heat conduction were correctly taken into account.

The differential equations modified in this manner can then be solved by the method of finite differences. The strong discontinuity surfaces will appear in the form of layers of finite thickness within which large gradients of the flow quantities occur. This method of artificially introducing dissipative terms in order to solve the equations of motion of an ideal gas by finite differences was proposed by Richtmeyer and Morton (1967), and subsequently used by Flagan (1982) among many others, to obtain the numerical solution of the equations governing the gas flow of an impinging jet. However, it was found that the method is susceptible to oscillations in the computed solution near shocks. Thus, several other attempts have been made to devise new methods.

Recently, Oh and Kim (1994) used a lower-upper symmetric Gauss-Seidel (LU-SGS) scheme combined with a flux-limited dissipation model to solve the same sets of equations. The LU-SGS scheme employs an implicit Newton iteration technique to solve the finite volume approximation of the governing equations which requires only scaler diagonal inversion with no spurious oscillations.

Another method that has been used is Finite Element Method - Flux Corrected Transport (FEM-FCT) (Lohner *et al.*1987). The advantages of this method over LU-SGS and finite difference include its ability to give monotonic results (no spurious oscillations) with a minimum of added diffusion, its easy extension to multiple dimensions, and its use of unstructured grids. The basic idea behind FEM-FCT algorithm is to calculate a solution using a low order method that gives smooth, overly diffuse results, and a high order method that gives an accurate solution whenever no regions of sharp gradients are present in the solution. The two solutions are then compared and corrected to give one solution with no oscillations in the regions of sharp gradients and a high order of accuracy elsewhere. Some of the results of the numerical solution of the equations governing compressible flow obtained by Jurcik *et al.* (1989) using FEM-FCT are presented and discussed later in this chapter.

2.1.2.2 Particle trajectories - Equations of motion

As mentioned earlier, particles will be assumed to be passive contaminants which implies that the their presence does not, in any way, alter the velocity and temperature fields that would

have existed in the absence of the particles. Thus, the particle equation of motion in the gas flow could be represented in general form as follows:

$$m_p \frac{du_i^p}{dt} = \frac{\rho}{2} A_p C_D |\mathbf{u}^g - \mathbf{u}^p| (u_i^g - u_i^p) + F_i + N_i(t) + F_{inte_i} \tag{2.24}$$

Here, m_p is the particle mass; ρ is the gas density; A_p is the projected particle cross-sectional area, $\mathbf{u}^g$ and $\mathbf{u}^p$ are the dimensioned carrier gas and particle velocity **vectors**, respectively, and i is the direction (r or z). The force, F_i, includes external forces due to gravity force and Colombic interactions and other phoretic force between the particle and collector, as well as the drag force due to the motion of the fluid over a stationary particle. $N_i(t)$ is a random force due to particle collisions with the surrounding gas particles (sometimes called the "Brownian force"), and F_{inte} represents a Columbic interaction force between a given particle and all of the surrounding particles and finally C_D, the drag coefficient.

If the gas-particle flow is dilute, the particles do not interact with each other; thus F_{inte_i} is negligible. Furthermore, F_i is infinitesimally small for nanometer-sized particle because of the negligible particle mass. Thus, on neglecting F_i and F_{inte_i} and rearranging, equation (2.24) reduces to:

$$\frac{du_z^p}{dt} = \frac{C_D(Re,Kn)}{24} \frac{Re_p}{\psi} |\mathbf{u}^g - \mathbf{u}^p| (u_z^g - u_z^p) + \frac{N_1(t)}{m_p} \tag{2.25}$$

$$\frac{du_r^p}{dt} = \frac{C_D(Re,Kn)}{24} \frac{Re_p}{\psi} |\mathbf{u}^g - \mathbf{u}^p| (u_r^g - u_r^p) + \frac{N_2(t)}{m_p} \tag{2.26}$$

where ψ is the modified Stokes number defined in the next section and

$$u_r^p = \frac{dr}{dt} \tag{2.27}$$

$$u_z^p = \frac{dz}{dt} \tag{2.28}$$

subject to the following initial condition at t=0

$$\begin{aligned} u_z^p &= u_n \\ u_r^p &= 0 \\ r &= r_{stat} \\ z &= 0 \end{aligned} \tag{2.29}$$

The drag coefficient C_D (Re,Kn) depends on the local values of the particle Knudsen and Reynolds number. Crowe (1967) has developed an empirical expression for the drag coefficient that correlates drag data in supersonic flows and reduces to Stokes law and free molecular results in limiting cases:

$$C_D = (C_D^0 - 2)\exp[-3.07\gamma^{1/2}(M_p/Re_p)g(Re_p)] + [(h(M_p)/(\gamma^{1/2}M_p))\exp[-Re_p/(2M_p)] + 2 \tag{2.30}$$

where the drag coefficient in incompressible flow is (Forney and McGregor, 1987)

$$C_D^0 = (24/Re_p)(1 + 0.158Re_p^{2/3}) \tag{2.31}$$

The remaining terms are

$$\ln g(Re) = 2.88[1 + \tanh(0.33\ln Re - 1.92)] \tag{2.32}$$

and

$$h(M_p) = 2.3 + 1.7(T_p/T_g) - 2.3\tanh(0.51\ln M_p) \tag{2.33}$$

where T_p and T_g are the particle and gas temperatures, and Re_p and M_p are the particle Reynolds and Mach number defined as follows:

$$M_p = \frac{|\mathbf{u}^p - \mathbf{u}^g|}{c} \tag{2.34}$$

and

$$Re_p = \frac{\rho |\mathbf{u}^p - \mathbf{u}^g| d_p}{\mu} \tag{2.35}$$

The random force, $N_i(t)$, in equation (2.24) is generally an independent white noise process with their spectral intensities, SP, given by (Ounis *et al.* 1991)

$$SP_{N_f N_f} = \frac{2kTf}{\pi}\delta_{ij} \tag{2.36}$$

where T is the absolute gas temperature, k is the Boltzmann's constant, and is the drag force. Equation (2.36) implies that the intensity of the Brownian force increases in direct proportion with temperature, T, of the gas.

The particle trajectory is calculated by numerically integrating the equations governing the particle motion, equations (2.25) through (2.36), providing the **gas flow field** is known. The collection efficiency for a given particle size under given flow conditions is determined by calculating the particle trajectories starting at different positions (from the center to the wall of the nozzle) and determining whether or not the particles impact on the substrate. The impaction process is usually characterized in terms of Stokes number, S. Physically, the Stokes number, S, is proportional to the ratio of the particle stopping distance and the jet diameter (Friedlander, 1977). Alternatively, it may be viewed as the ratio of the particle relaxation time to the transit time of the airflow across the impaction plate in non-Stokesian regime. The relaxation time is the time taken for a particle initially at rest to achieve 63% of the velocity of the gas stream. The issue of defining an appropriate ("universal") Stokes number capable of characterizing the particle impaction process in compressible fluid flows has been discussed by many investigators (Isreal and Rosner, 1983; Flagan, 1982; Biswas and Flagan, 1984; de la Mora *et al.* (1990a&b); Forney and McGregor, 1987). The Stokes number as it is presented by de la Mora et al. (1990a) is relevant to this work and it is detailed in the next section.

2.1.2.3 The "modified" Stokes Number, Ψ

The collection efficiency of a collector in a low velocity flow field is mainly determined by an inertia parameter characterizing the particle motion, termed the Stokes number. However, for non-Stokesian particles, the collection efficiency also depends on a Reynolds number based on the particle diameter and the free-stream velocity. For a potential flow field approximation to the fluid motion about the collector, the collection efficiency of cylindrical and spherical targets have been calculated numerically as a function of both the Stokes and particle Reynolds numbers (Brun *et al.*, 1955; Dorsch *et al.*, 1955) and the collection efficiency curves for both Stokesian and non-Stokesian particles were found to be qualitatively alike. Thus, attempts were made to predict the deposition rate of particles over a wide size spectrum (as would occur, e.g., in gas turbine and gas cleaning applications). A representation of the collection efficiency that dramatically reduces its dependence on geometric and fluid dynamic parameters would greatly facilitate computations. Thus, the Stokes number which correlates particle motion in low Reynolds number flow, has been modified to account for non-Stokesian particle drag and gas compressibility in high velocity flows.

The modified Stokes number by Chang *et al.* (1993) takes into account the effects of Knudsen number, Reynolds number and detachment distance of the standoff shock, and is defined as follows:

$$\Psi = \left(\frac{\rho_p d_p^2 V_j}{18\mu d_j}\right)\Phi_c(Kn_{p2})\,\Phi_r(Re_{p2})\,\Phi_s(P_o/P_\infty, S/W) \qquad \textbf{(2.37)}$$

the subscripts 1 and 2 refer to gas properties ahead of and behind the strong standoff shock, respectively. Φ_c is the empirical Cunningham slip correction factor taking into account departures from continuum flow:

$$\Phi_c = 1 + 2Kn_{p2}\left(1.257 + 0.4e^{-0.55/Kn_{p2}}\right) \qquad \textbf{(2.38)}$$

where Kn_{p2} is the particle Knudsen number defined as the ratio of the mean free path of gas, λ_2, to the particle diameter, d_p

$$Kn_{p2} = \frac{2\lambda_2}{d_p} \tag{2.39}$$

The non-Stokesian particle drag is accounted for by including in equation (2.37)

$$\Phi_r = \frac{18}{Re_{p2}}\left(R_{p2}^{1/3} - 2.52\tan^{-1}\left(\frac{Re_{p2}^{1/3}}{2.52}\right)\right) \tag{2.40}$$

where Re_{p2} is the particle Reynolds number behind the shock

$$Re_{p2} = \frac{\rho_p d_p u_1}{\mu_2} \tag{2.41}$$

Φ_s rescales the impaction parameter in terms of detachment distance of the standoff shock, δ

$$\Phi_s = \frac{d_n}{\delta} \tag{2.42}$$

Note that to calculate the modified Stokes number described in equation (2.37), the information on the shock location together with the known flow field of the free jet in the absence of the collector and linear description of the post-shock velocity field is required.

On the other hand, de la Mora (1990a) defined the relevant Stokes number as the one characterizing the deceleration process in the impaction region in terms of the particle's terminal velocity, U_∞, and shock standoff distance, δ, as follows:

$$\psi = \frac{\tau_2 U_\infty}{\delta} \tag{2.43}$$

where

$$U_\infty^2 = \frac{2\gamma kT}{M_g(\gamma - 1)} \tag{2.44}$$

and M_g the molecular mass of the carrier gas and T its absolute stagnation temperature.

According to de la Mora *et al.* (1990a), the particle relaxation time, τ_2, must be determined at the source stagnation temperature and post-shock stagnation pressure, p_2. Impaction occurs for a value of ψ larger than a critical threshold close to **unity**. Since the conditions in the impaction region are usually unknown, another Stokes number, ψ_o, based on the known stagnation conditions, is defined:

$$\psi_o = \frac{\tau_o c_o}{d_n} \tag{2.45}$$

where

$$\tau = \frac{m_p}{f_d} \tag{2.46}$$

$$c = \sqrt{\frac{\gamma kT}{M_g}} \tag{2.47}$$

and in the free-molecule region, the drag coefficient, f_d, derived from the kinetic theory is:

$$f_d = \frac{2}{3}\rho d_p^2 \left(\frac{2\pi kT}{M_g}\right)^{0.5}\left[1+\frac{\pi\alpha}{8}\right] \tag{2.48}$$

where ρ, the gas density is:

$$\rho = \frac{\gamma P}{c^2} \tag{2.49}$$

The accommodation coefficient, α, in equation (2.47) represent the fraction of molecules that leave the surface in equilibrium with the surface, and it must, in general, be evaluated experimentally but is usually near 0.9 for momentum transfer (values differ for heat and mass transfer), (Friedlander, 1977).

Combining equations (2.45) through (2.49) (all evaluated at stagnation conditions) gives:

$$\psi_o = 0.1309 \sqrt{\frac{\pi}{\gamma} \frac{\rho_p d_p c_o^2}{d_n P_o}} \qquad (2.50)$$

if $P_o/P_1 > 1$, $Re > 1$ and L/d_n $(=x) > 1$, the Stokes number in the impaction region, ψ, can then be estimated from ψ_o using the following approximate relation (de la Mora, 1990b):

$$\psi = \frac{G(x)\psi_o L}{d_n} \qquad (2.51)$$

G(x) relates the stokes number based on stagnation condition to the stokes number near the impaction plate and it is a property of the support gas and the gas Mach number. For most of the common gases used in this study, γ is approximately 1.4 and the asymptote value of G, $G(\infty)$, is about 32.02 corresponding to the hypersonic regime where the gas reached the terminal speed, U_∞.

2.1.2.4. Computational Results

In order to have a better understanding of the operating parameters of the low pressure impactors, several computer simulations of the model that is represented by the set of equations presented earlier in this chapter have been done for round jet (Jurcik *et al.* 1989) and slit jet (Chang *et al.* 1993). In all these simulations, the gas flow field of an impinging sonic jet is calculated first. With the assumption that the particles are passive contaminants, particle trajectories are calculated using the gas flow field. Some of the simulation results of Jurcik *et al.* (1989) will be presented in this section for the purpose of showing the variation of particle collection efficiencies with the ratio of nozzle-to-plate distance, L, and the presuure ratio.

The simulation result in Figure 2.7 shows the cut-off diameter, particle diameter corresponding to 50% collection efficiency, for a constant pressure ratio (P_1/P_o), χ, of 0.2 plotted as a function of the downstream pressure, P_1, at various values of S/D. S is the distance between the nozzle and the plate, which was previously defined as L and D is the nozzle diameter, d_n. As P_1 decreases, smaller particles are collected on the surface. The physical reason for this phenomenon is that as S/D increases the central compression shock moves further downstream, the pressure at the stagnation point decreases. Thus, the particle is accelerated to a higher

velocity before the central compression shock and the drag force is decreased in the wall region as S/D increases, allowing smaller particles to impact.

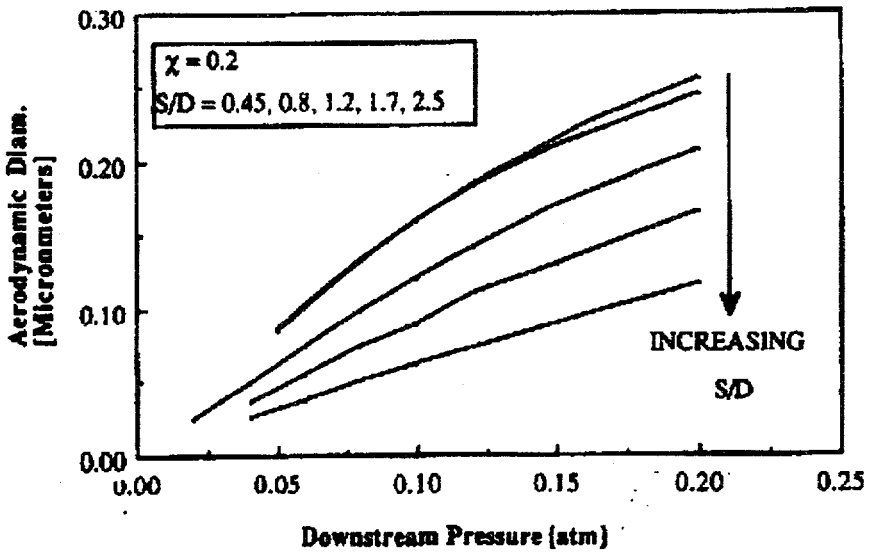

Figure 2.7: Calculated aerodynamic diameter for an inertial impactor stage with D=0.1 cm for several values of S/D for a constant pressure ratio χ = 0.2 (Jurcik *et al.* 1989 - Used with permission)

The results for constant S/D=0.8 and various pressure ratios are shown in Figure 2.8 and 2.9. Figure 2.8 shows the cut-off diameter as a function of downstream pressure for various pressure ratios. This figure shows that the cut-off diameter decreases with increasing upstream or the stagnation pressure , P_o. The same results plotted as a function of upstream pressure in Figure 2.9 show that the three larger values of χ fall on the same curve. This result implies that for an S/D=0.8, the 50% cut-off diameter is relatively insensitive to small changes in the downstream pressure, P_1, for moderately underexpanded jet.

Figures 2.10 and 2.11 shows the gas flow field for S/D=0.8 and 2.5, respectively, (at non-dimensional time=3.5) with typical particle trajectories superimposed on the figures. For the S/D value of 0.8 (Figure 2.10) the gas accelerates in the axial direction to Z/D=0.5 where it rapidly decelerates and strong radial flow begins. For the S/D value of 2.5 (Figure 2.11), the location of the plate is well behind where the shock will form in a free jet, the recirculation bubble is clearly seen and recurs with time. The effect of the recirculation bubble on the particle trajectories is to

cause most of the particles to be collected off the axis which can cause anomalous behaviour, non-monotonic response, of the impactor.

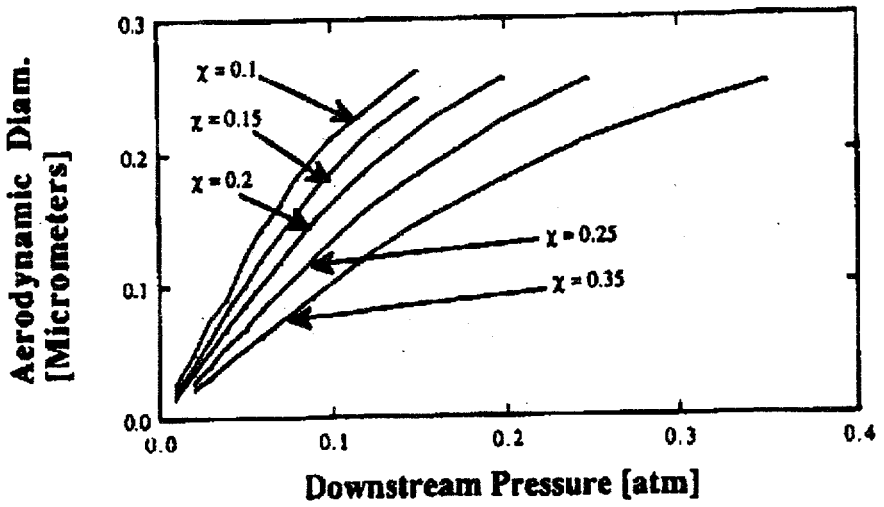

Figure 2.8: Calculated aerodynamic diameter as a function of downstream P_1, for several values of χ and S/D=0.8 (Jurcik *et al.* 1989 - Used with permission)

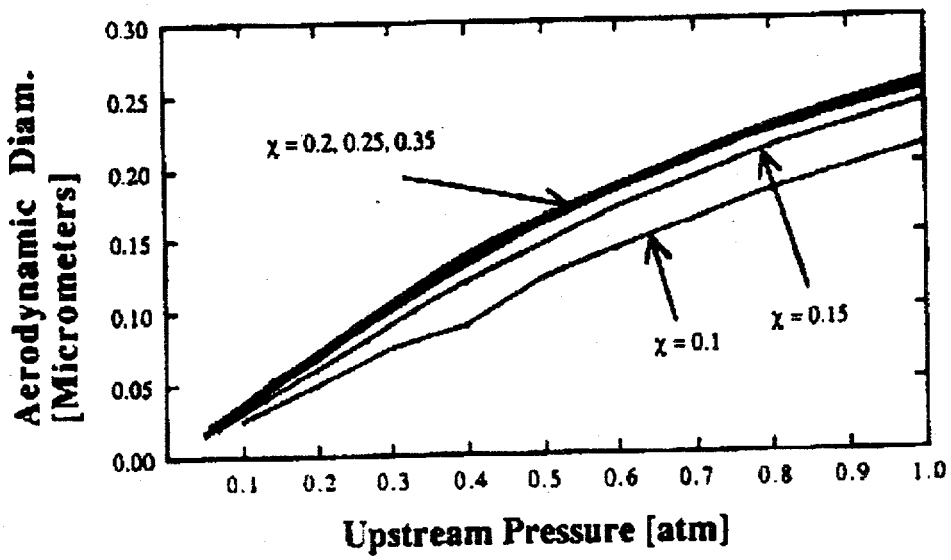

Figure 2.9: Calculated aerodynamic diameter as a function of upstream P_o, for several values of χ and S/D=0.8 (Jurcik *et al.* 1989. Used with permission)

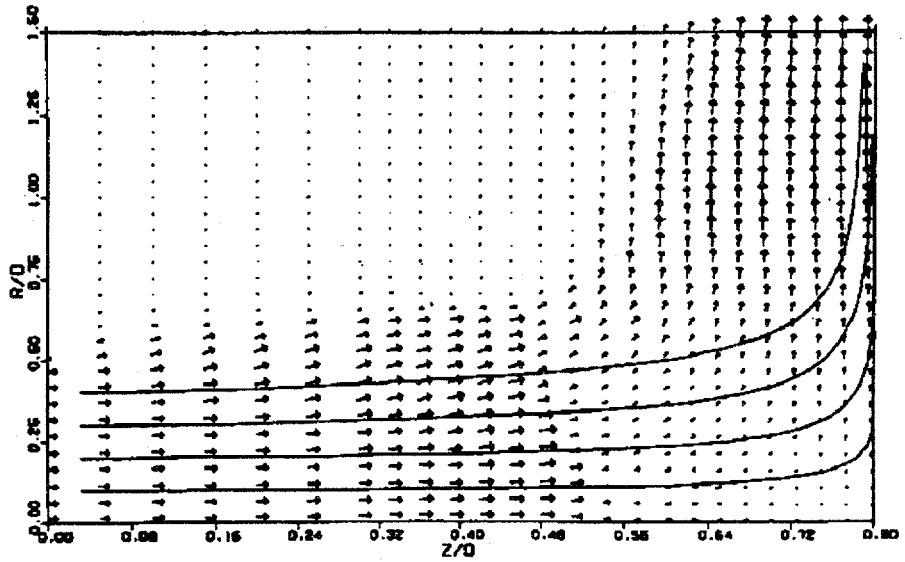

Figure 2.10: Calculated gas flow field for an inertial impactor stage with S/D=0.8 and χ=0.2. The solid lines denote typical particle trajectories for a particle size that is approx. 50% collected. (Jurcik *et al.* 1989 - Used with permission)

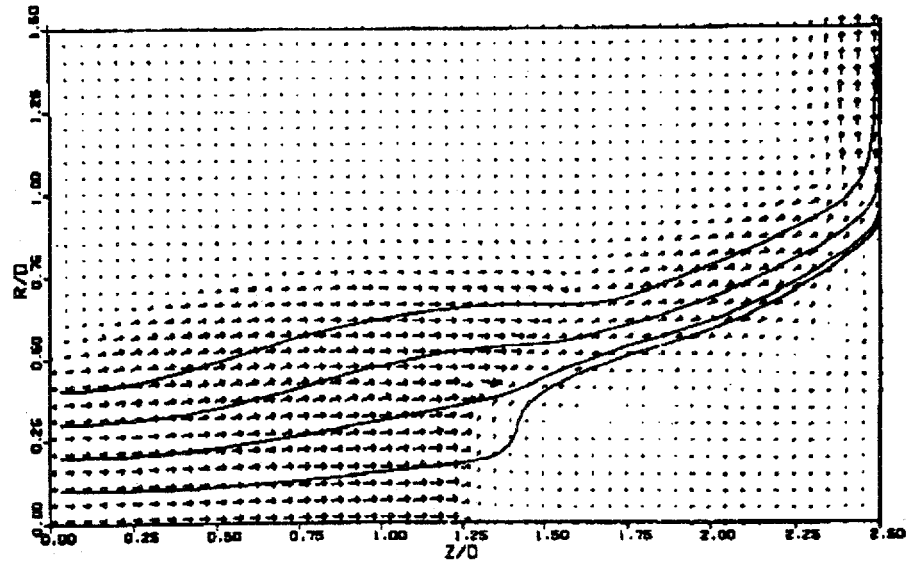

Figure 2.11: Calculated gas flow field for an inertial impactor stage with S/D=2.5 and χ=0.2 (Jurcik *et al.* 1989 - Used with permission)

2.2. Summary remarks

In this chapter, the mathematical model for predicting ultrafine particle collection efficiency in low pressure impactors was presented and discussed. The model was derived based on the following simplifying assumptions: 1. Ideal gas, 2. constant specific heats, 3. perpendicular velocities to the shock, 4. adiabatic process and 5. isentropicity at the nozzle. The system of equations which constitute the model are non-linear and therefore they are unamenable to any known analytical solution. The simulation result obtained by solving the equations numerically were also presented. The result clearly showed that in low pressure impactors the size of collected particle is determined by the nozzle-to-plate distance, L and the downstream pressure, P_1. Thus, L and P_1 are the important parameters in the design of the hypersonic impactor (chapter 3). Above all, this chapter was able to provide the framework of ideas that led to the design of the HI system.

Chapter
THREE

HYPERSONIC IMPACTOR DESIGN AND TESTING

The objective of this research project was to develop an operable system that could measure the aerodynamic size of ultrafine radioactive particles, and subsequently use the system to investigate the changes in their physical and chemical forms as a result of their interaction with the trace gases present in ambient air.

The ability of ionizing radiation, such as x-rays, alpha and beta particles, to produce ultrafine aerosols in filtered air containing trace quantities of gases such as SO_2, O_3 and organic vapors is well documented (e.g. Chamberlain *et al.*, 1957; Perrin *et al.*,1978; Leong *et al.*, 1986)

In support of this hypothesis is the work on radon progeny reported by (Chu *et al.*, 1987; Ramamurthi *et al.* 1993; He and Hopke, 1995) that provided indications of radiolytic formation mechanism of sulfuric acid nuclei and ultrafine aerosols from the oxidation of SO_2 added to radon-carrier gas mixtures.

In humid air, Hawrynski (1984) postulated the existence of clusters of water molecules around ionized radon decay products and that air humidity strongly influences the size of the cluster. Under normal conditions, he estimated cluster sizes to be 1.3 nm for 1% RH (40 molecules forming the clusters) and 2.3 nm for 100% RH (220 molecules in the cluster). However, Castleman (1991) postulated that only 5 to 8 water molecules can cluster around an ion, depending on the prevailing humidity and temperature. Nevertheless, both authors agreed that water molecules will cluster around radon progeny.

The hypersonic impactor system developed in this study was patterned after the one described by de la Mora *et al.*(1990a). The basic difference in the two designs is the property of the particle being monitored. The latter utilizes the particle's electrical charge, while the former was designed to utilize the particle's radioactivity because the use of de la Mora system is limited because of the difficulty in charging sub-nanometer particles as previously mentioned.

A detailed description of the HI system is presented in this chapter. The cross-sectional design of the HI system is shown in Figure 3.1 and the photograph of the same system is shown in Figure 3.2. The major system components are: the stainless steel cross, the collection and the nozzle assemblies. The photograph (Figure 3.2) shows the stainless steel cross standing with support on a table. Also shown on the photograph are the flexible coupling, the pressure gauge head (red) and its control/readout unit, the connection pipe with the cylindrical chamber, micrometer screw gauge, the regulating valve and the rotary pump. The micrometer screw gauge, white in color, sits on the brown support. The flexible coupling connects the system to the pump through the regulating valve. The gauge head measures the pressure in the chamber and is mounted in the figure with its face down and its body tube vertical, and a connecting cable to the body tube. The design features of most of these instruments will be presented and discussed in turn in the following sections. This chapter also presents the experimental system used for testing of the HI together with a detailed procedure for estimating the particle size from experimental data.

3.1. Stainless Steel Cross

The cross dimensions are as shown in Figure 3.3. It has flanges on its four arms. One of the side arms of the cross is connected to a reducer(MDC), which has two other flanges. As shown in Figure 3.2, one of the reducer flanges is connected to a Pirani vacuum gauge head (Edwards Model PRH10K) and the other to a pre-amplifier that is connected to an amplifier and a multichannel analyzer (see Figure 3.10). The left arm of the cross is connected to a rotary mechanical pump (Fisher Maxima, Model 16A) through a regulating valve that controls the pressure ratio and a flexible coupling. The Fisher pump was later replaced with another rotary pump Trivac (Model D30A) with a capacity of 1030 liters/min. The Trivac pump permits a pressure of about 0.44 torr in the vacuum chamber at an aerosol flowrate of about 0.7 liters/min. Electrically, the cross is maintained at ground potential. The grounding is necessary to prevent interference from external signals, thereby reducing the electronic noise level to the minimum.

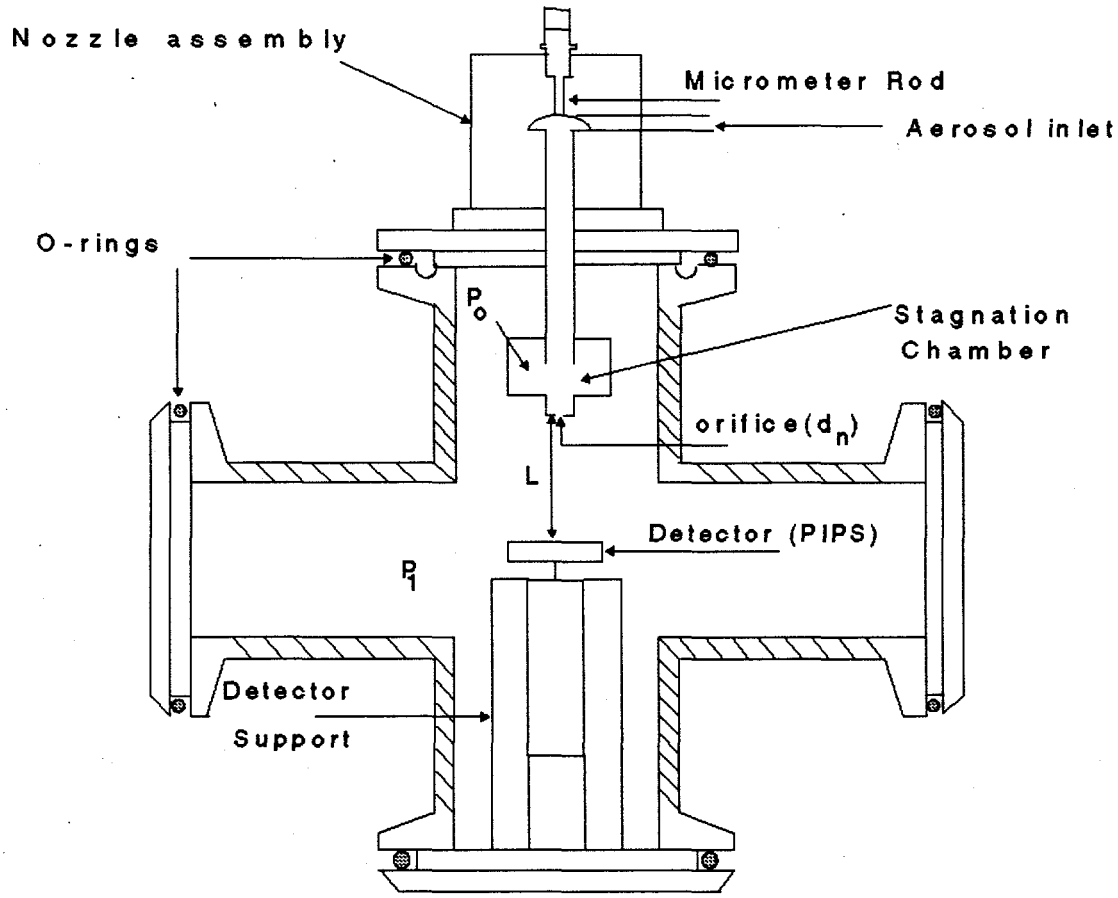

Figure 3.1: Cross-sectional view of the Hypersonic Impactor

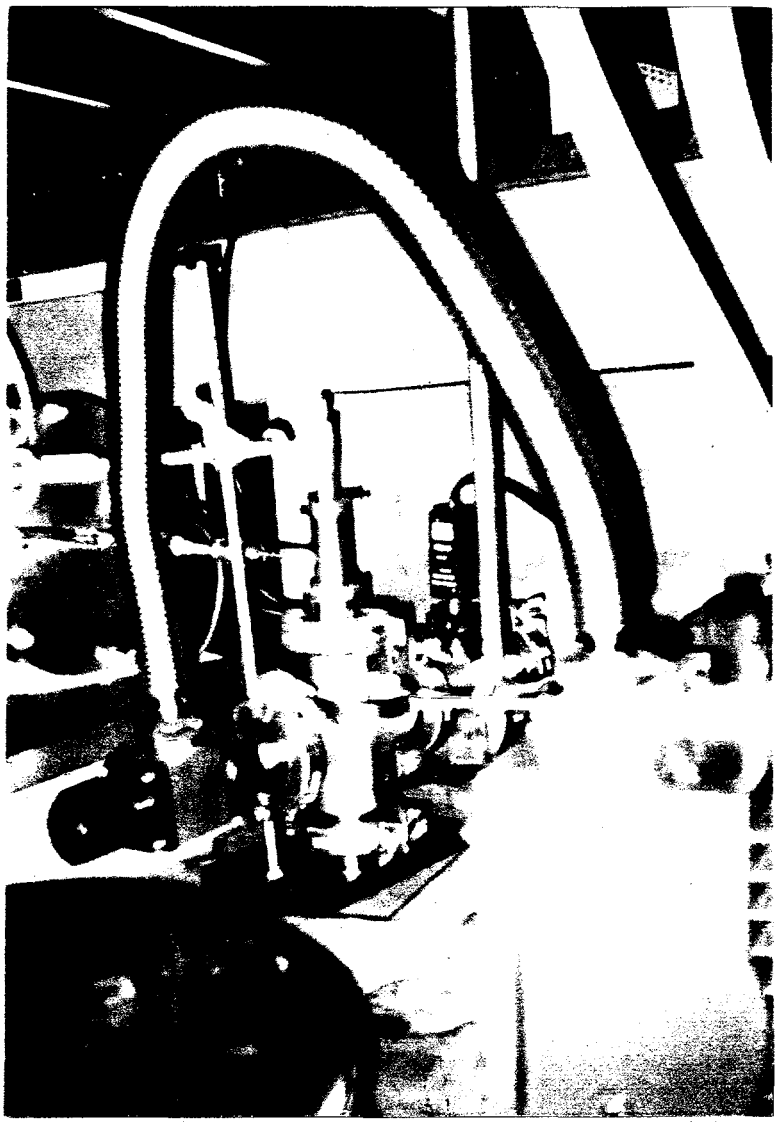

Figure 3.2: Photograph of the HI system with the stainless steel cross connected to the vacuum gauge and pump, and the aerosol inlet pipe connected to the radon chamber.

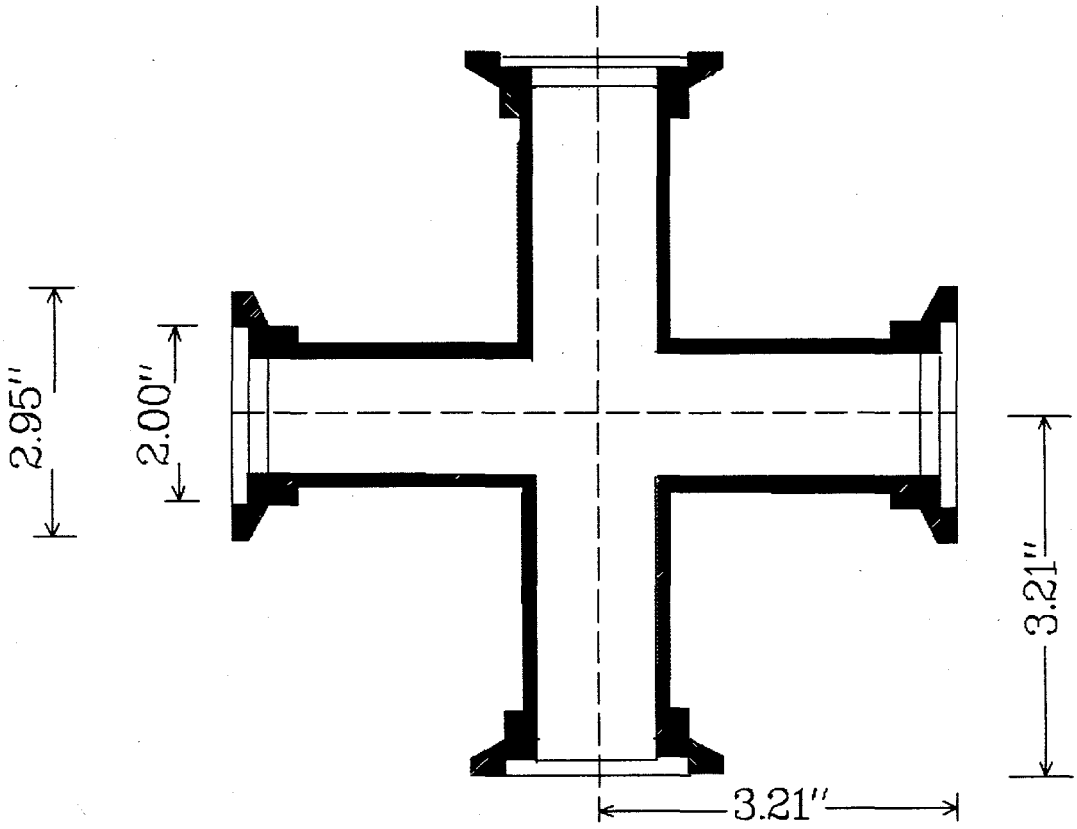

Figure 3.3: Cross-sectional view of the Stainless Steel Cross

3.1.1. Pirani vacuum gauge

The gauge consists of a gauge head (Edwards, PRM10K) shown in Figure 3.4 and a control unit. The gauge head is connected to the stainless steel cross and the control unit. With the face of the KF10 flange horizontal and the body tube of the gauge head vertical, the head was mounted as close as possible to the point at which pressure was measured, to reduce reading error. Long, narrow and angled connections have been found to cause significant reading errors.

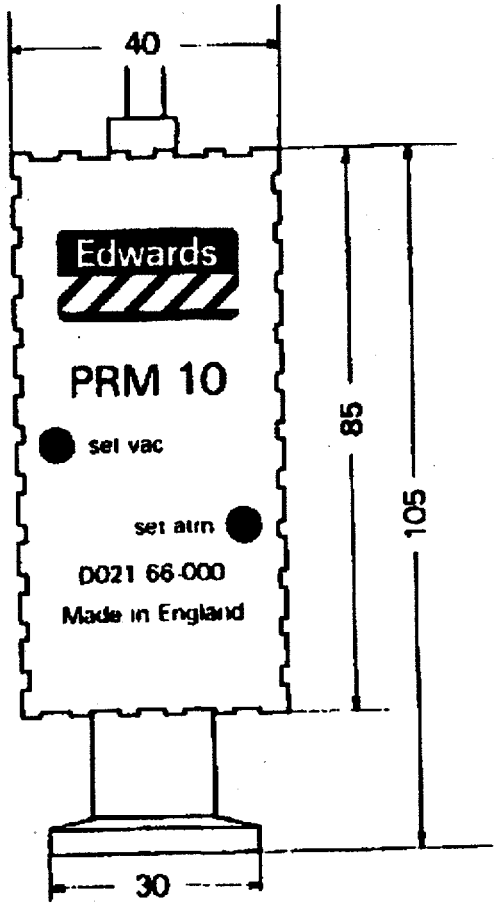

Figure 3.4: Gauge head

The gauge head (40 x 26 x 85) mm can measure pressure ranging from 200 to 10^{-3} mbar. It operates on the Pirani principle that, at a low pressure, the thermal conductivity of any gas varies with pressure. The interior of the gauge head is open to the vacuum system and contains a filament that is heated by current from the control circuits. The amount of heat lost to the surrounding gas diminishes as the gas pressure falls, so that filament temperature rises. Thus,

the electrical resistance of the filament increased. The filament forms one arm of a Wheatstone bridge which is balanced at atmospheric pressure and becomes unbalanced as the pressure decreases. The imbalance signal is used in a feedback circuit to adjust the bridge voltage and bring the filament resistance back to its original value. The head therefore operate in a constant temperature mode and the bridge voltage is a function of pressure, and it's output is gas dependent as the thermal conductivity of different gases vary.

The "set atm" and "set vac" pre-sets on the gauge head were used to calibrate the gauge. For a detailed calibration procedure, see the equipment manual. For the 0.2 mm orifice, the pressure reading was 0.9 torr and 0.4 torr for Fisher and Trivac pumps, respectively.

3.2. Nozzle assembly

Sitting on the top arm of the cross is the nozzle assembly shown in Figure 3.5. Its uppermost part is a vertical micrometer whose frame is attached to the upper surface of the flange. The bottom surface of the moving micrometer pushes against a steel pipe (1/4" outer diameter and 5" long) that penetrates through the flange deep into the stainless steel cross. The atmospheric side of this pipe is fed perpendicularly by a soldered 3.5-inch long tube segment of identical cross-section, through which the aerosol enters.

The bottom end of the pipe is screwed onto a 1.18-inch long, 1-inch OD cylindrical metal piece (stagnation chamber). In order to reduce the amount of particle wall loss, a relatively large stagnation chamber was used in this system. The stagnation chamber has a diamond knurled metal cap with a small projection having a center hole (0.28" diameter) closed by a soft soldered orifice plate (MICRO-ENGINEERING, Coventry, RI) , 0.4-inch diameter and 0.004-inch thick, with a **round orifice** of 200 μm - See Table 3.1. The orifice is a **beam aperture for an electron microscope** and it is not easily damaged by mechanical handling or chemical corrosion (made of platinum). However, small imperfections in the orifice have been found to cause anomalous behavior in a sonic velocity impactor (Kalghatgi and Hunt, 1976).

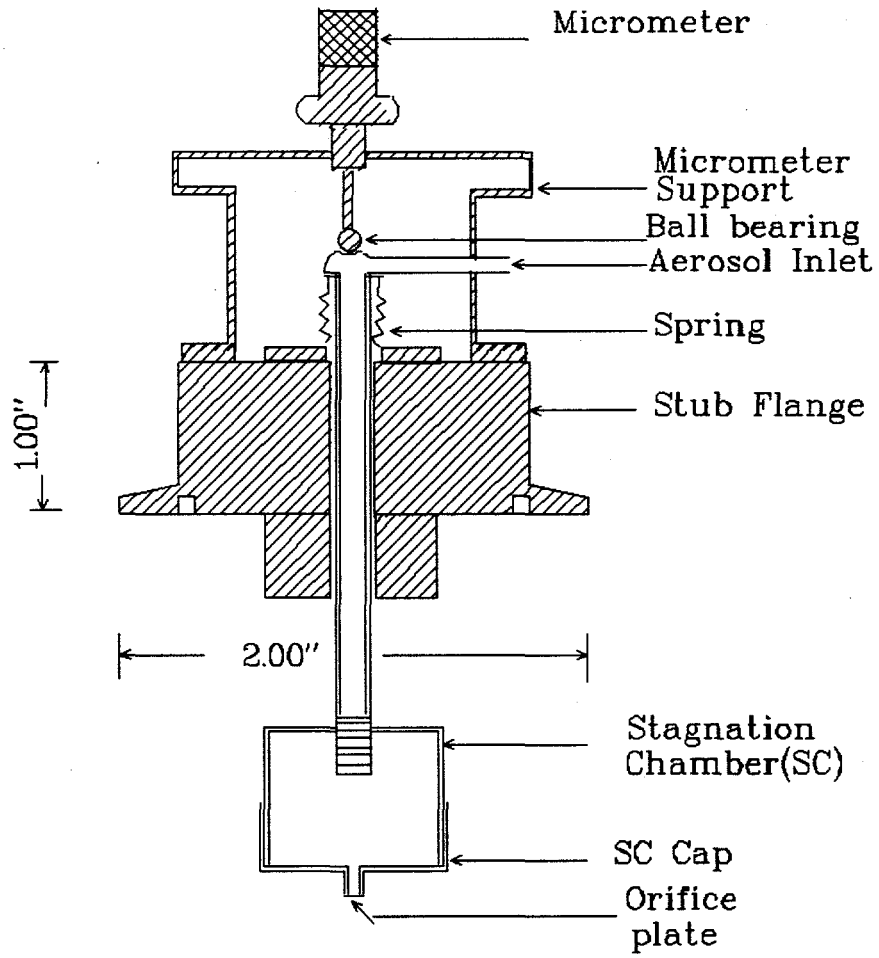

Figure 3.5: Cross-sectional view of the nozzle assembly

Table 3.1 Orifice plate specification

Diameter	0.4"
Thickness	0.004"
Orifice	200 μm

The position of the orifice relative to the collection plate is adjusted by means of the micrometer which moves the entire orifice tube assembly. The opposing force is provided by a spring and the vacuum seal is provided by the "O" rings.

3.3. Collection assembly and the counting system

The collection assembly (Figure 3.6) consists of the particle implanted planar silicon (PIPS) barrier detector (CANBERRA, Meriden, CT) and the support.

PIPS Detector

Table 3.2 gives the detector specifications and performance data. The detector can be cleaned with methanol and cotton swab should its surface become contaminated. The detector is positioned on a support, concentric with the orifice on the stagnation chamber of the nozzle assembly. It collects and detects the alpha particles emitted by the radioactive particles.

Table 3.2: Detector specifications and performance data

SPECIFICATIONS	
Active area	300 mm^2
Warranted alpha resolution	19 keV
PERFORMANCES	
Recommended bias voltage	40 volts
Leakage current (at 20°C)	12 nA
Minimum depletion depth	>140 microns
Electronic noise	9.4 keV
Operating bias voltage (min/max)	+20/+80 volts
Typical background	0.05 cts/cm^2/hour
Silicon chip thickness (min/max)	275/315 microns

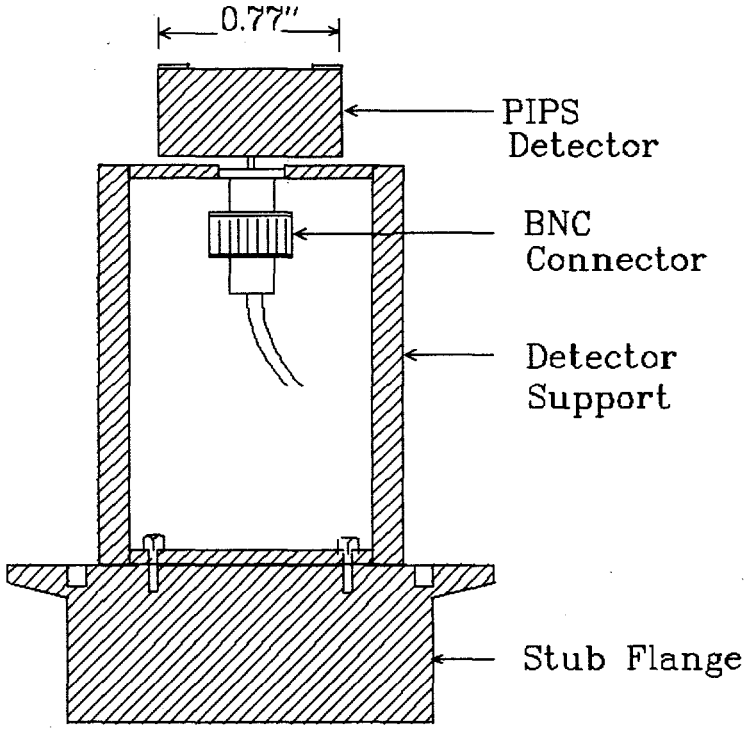

Figure 3.6: Cross-sectional view of the collection assembly

The signal from the PIPS is sent via a cable to the pre-amplifier and amplifier into a PC based Multichannel Analyzer (MCA) with an in built multiplexer as shown in Figure 3.10 (Section 3.5). The MCA measures the energy spectrum of a radioactive source by recording the pulse-height distribution produced by the particles emitted from the source.

Multichannel analyzers are used in either of two different modes: the pulse-height analysis (PHA) mode or the multichannel scaling (MCS) mode. The former is used to sort incoming pulses according to their voltage and store the number of pulses of a particular height in a corresponding address of the MCA memory called the channel number. The latter is used to count events as a function of time. The individual channels of the memory count all incoming pulses for a preset time width Δt. After time Δt, the counting operation is switched automatically to the next channel in the memory, thus providing in the end a time sequence of the radiation being detected.

In the PHA mode, the incoming pulse enters into a unit called the analog-to-digital converter (ADC). The ADC digitizes the pulse amplitude and produces a number proportional to the height of the pulse, a number which determines the channel where the pulse will be stored.

The size of the ADC, given in terms of the number of channels, defines the absolute resolution of the system. Actually, the ADC determines the number of discrete parts into which the pulse height can be subdivided. Commercial ADCs can have a size up to 8192 channels, with the full scale adjustable in steps of 256, 512, 1024, etc channels. The number of discrete parts (channels) into which the input pulse range (0 to +10V) is divided is called the conversion gain.

The MCA is connected to the MCA controller card in one of the expansion slots in the PC's motherboard. All the electronic modules (1 amplifier, 1 power supply, 1 pulse generator, MCA) are housed in a standard NIM bin and power supply unit.

Detector Support

The detector support is a cylindrical solid piece with a central groove that holds the BNC connector. It has a lateral opening through which the co-axial cable from the connector to the pre-amplifier passes. The finite length of the cable connecting the detector to the pre-amplifier introduces some capacitance into the counting system, thereby resulting in a somewhat broader peak.

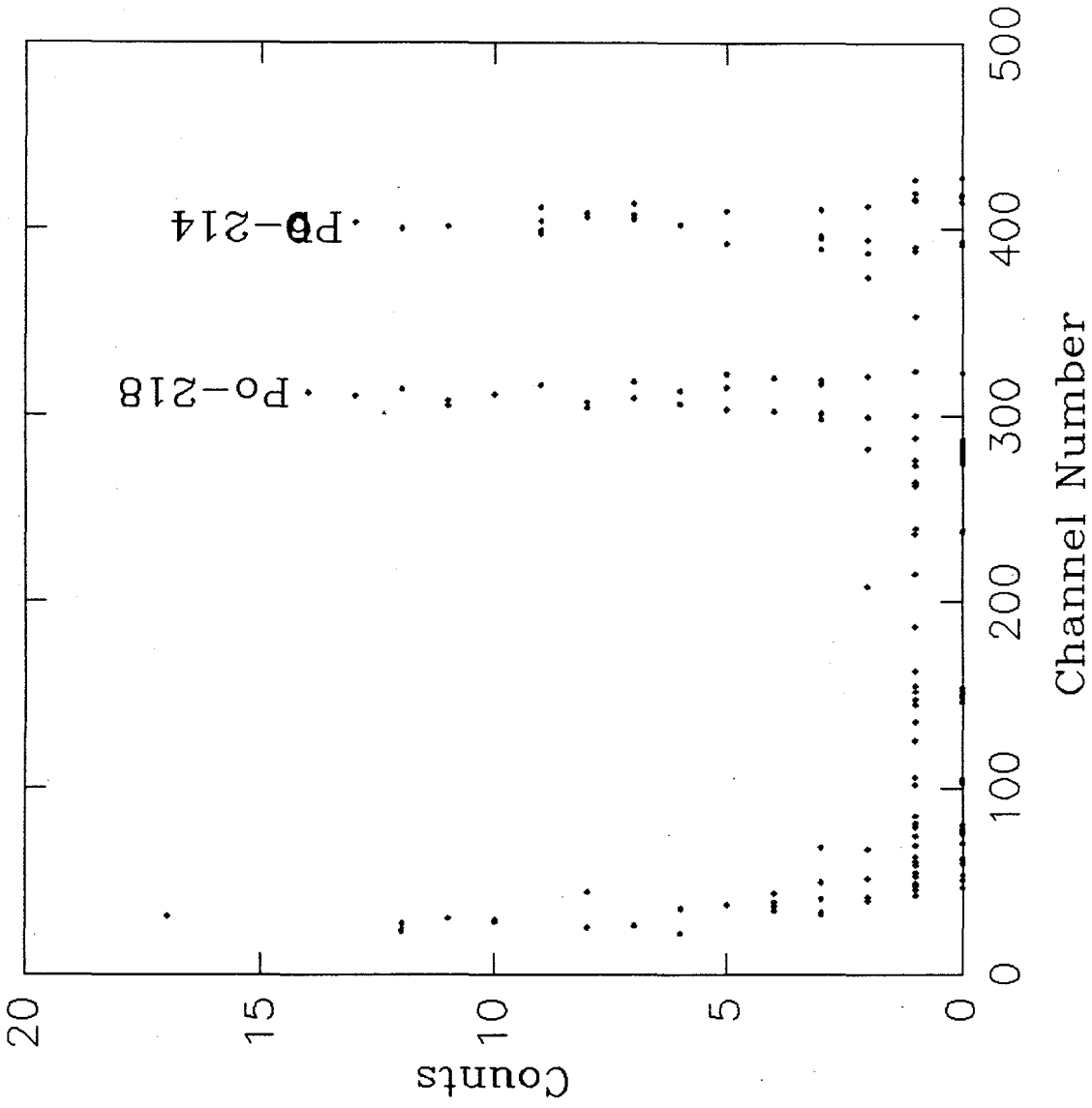

Figure 3.7: The typical α-spectrum of Po-218 and Po-214 of the HI system.

However, the broader peak does not in any way affect the performance of our system because of the high resolution of the detector used. The bottom part of the support is screwed to an MDC stub flange as shown in Figure 3.6.

3.4. HI System Operating Procedure

Since the impactor operates at reduced pressure, care must be taken to insure that there are no leaks in the system. Leaks not only cause contamination of the sample, but will also affect the pressure drop in the instrument, which deteriorates the impactor performance. At the start of operation, the impactor inlet is sealed and evacuated with the sampling pump. The valve to the pump is then closed and the vacuum gauge is watched for a rise in pressure.

After ensuring no leakage, both the valves to the pump and the impactor inlet are opened. The aerosol enters through the tube segment into the stagnation chamber and expands through the orifice into the evacuated chamber at supersonic velocity. A shock is formed just before the PIPS collection plate resulting in a subsonic flow near the plate - See chapter 2. Particles with sufficient inertia deviate from the gas streamlines and are collected on the surface. The number of particles collected is determined by alpha spectroscopy. The signals of the detector, collection plate, are amplified by a preamplifier-amplifier combination and the spectra are collected with a multichannel analyzer, controlled by a PC, which starts and stops the α-spectroscopy and stores the spectra.

Figure 3.7 shows a typical alpha spectrum obtained during the system testing showing peaks corresponding to ^{218}Po and ^{214}Po, respectively. By integrating ^{218}Po peak, one alpha count per deposited ^{218}Po nucleus is obtained, since the counting efficiency for each nuclide is essentially 50%. The number of other radon progeny in the gas stream is assumed to be negligible due to the high ventilation rate. In order to scan the whole aerosol, the procedure is repeated for several values of orifice-to-plate (L) distance. A plot of the particle counts against L is then made. The middle of the "S" shaped curve is estimated and the value is used to estimate the particle diameter (section 3.7). Generally the number of steps present in an impactor curve is an indication of the aerosol's dispersity. One step indicates a monodisperse aerosol (Figure 3.8) and two or more steps as shown in Figure 3.9 suggests polydispersed aerosols.

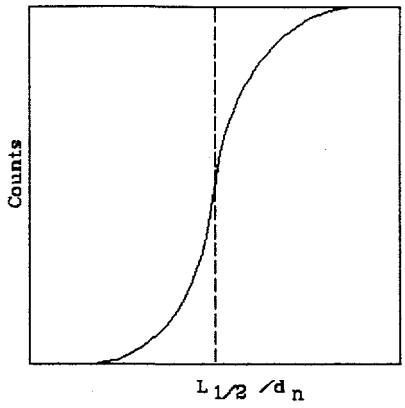

Figure 3.8: Impactor curve with single step

The main advantage of the on-line measurement is that the sampling time is not restricted by the half-life of decay of the radioactive particles/clusters investigated. It is even advantageous to have a short $t_{1/2}$ so that most of the particles will decay during the sampling interval plus 10 minutes.

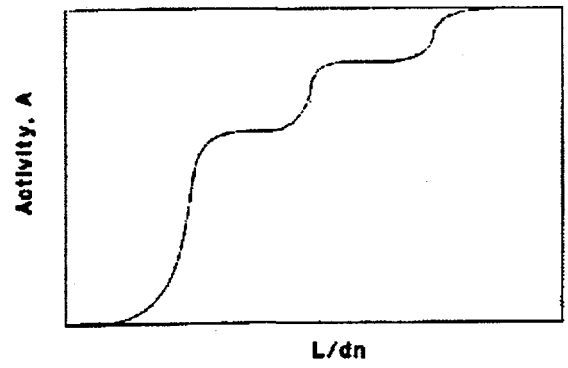

Figure 3.9: Impactor curve with several steps

3.5. Experimental System used for HI System Testing.

The experimental system used for the system testing is shown schematically in Figure 3.10. It includes the aerosol generation part, and the HI with the counting systems which incorporates the personal computer for data acquisition and analysis.

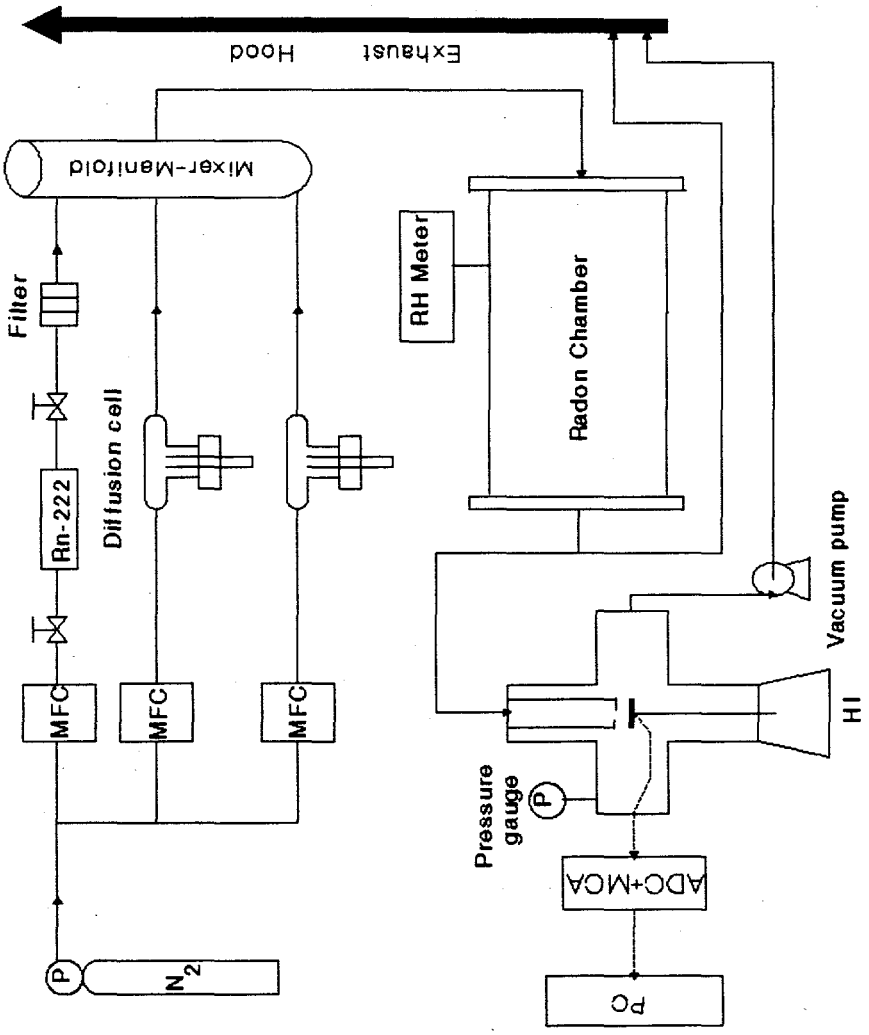

Figure 3.10: Experimental System

Since both the HI and the counting system have been previously described in detail, the detailed description of the aerosol generation system will be presented in this section.

3.5.1 Radon chamber and its flow system.

Nanometer sized particles are generated in the radon chamber by mixing radon laden gas stream with other trace gases, depending on the particle size to be generated. The gas flow rate is controlled by mass flow controllers (Tylan Corporation) that are connected to a readout/control unit. The full scales of the mass flow used are 100 CCM and 1 SLPM (standard liters per minute) with a relative uncertainity of about 1.0%.

The radon gas is from two flow-through Pylon Rn-1025 source with continuous outputs of about 1.39×10^5 and 1.61×10^5 mBq min^{-1}. The source contains a dry radium (^{226}Ra) that provides calibrated quantities of radon gas with an accuracy of ±4%.

Trace concentrations of the organics in the support gas are obtained by passing it through the diffusion cell (Miguel and Natusch, 1975) containing the desired organics. Similarly, water vapor is added to the support gas stream with the aid of a water bubbler (modified water-purification cartridge holders) immersed in a constant temperature water bath. The humidity of the gas stream is monitored using a chilled-mirror dew point hgyrometer (General Eastern Co., Model M1). However, if few ppm of water is desired, the water bubbler is replaced with a diffusion cell.

The water and/or organic laden N_2 gas were mixed with radon gas in the mixer-manifold. The mixer-manifold is a stainless-steel cylinder (2.5-inch o.d, 1/4-inch wall and 10 inches long) with 6 inlet ports and a single outlet port to the radon chamber. The photograph of the chamber is shown in Figure 3.11. The chamber is a stainless steel cylinder with an internal volume of 32 liter. It was designed with 6 sampling ports and 8 BNC bulkhead fittings for electrical and electronic connections. The relatively long residence time (32 min) provided by the chamber permits formation of sufficient number of radon progeny/clusters and its relatively wide internal diameter reduces the rate of particle wall loss.

The relative humidity inside the chamber was monitored continuously with a dew point hygrometer (General Eastern) while the detectable particle concentration was monitored intermittently by a TSI Ultrafine Condensation Particle Counter (UCPC). Because the detection limit of the UCPC is about 3 nm, it could not detect radon progeny clusters. Thus, the primary use of UCPC was to ensure that particle with sizes greater than 3 nm were not being generated.

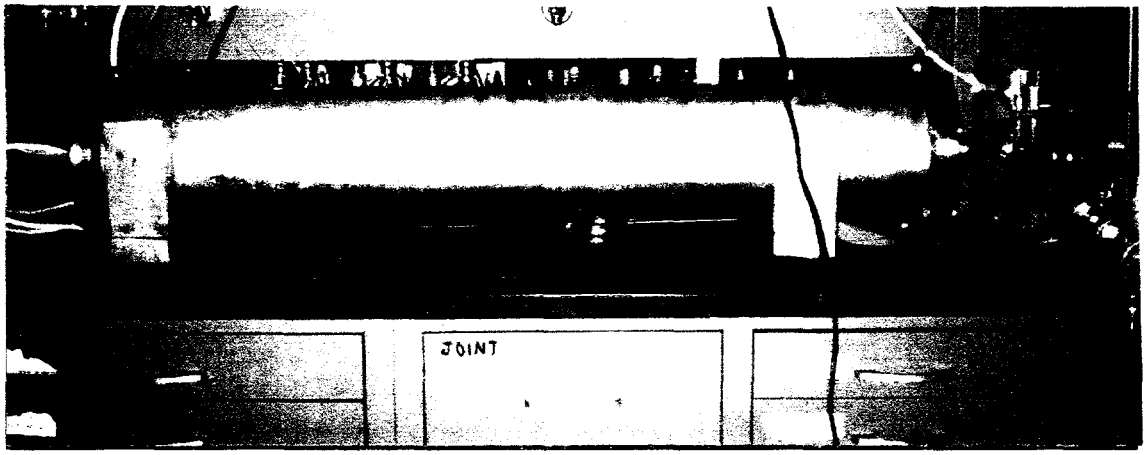

Figure 3.11: Photograph of the radon/aerosol chamber

Ultrafine Condensation Particle Counter (UCPC)

The Ultrafine Condensation Particle Counter (Figure 3.12) is a continuous flow

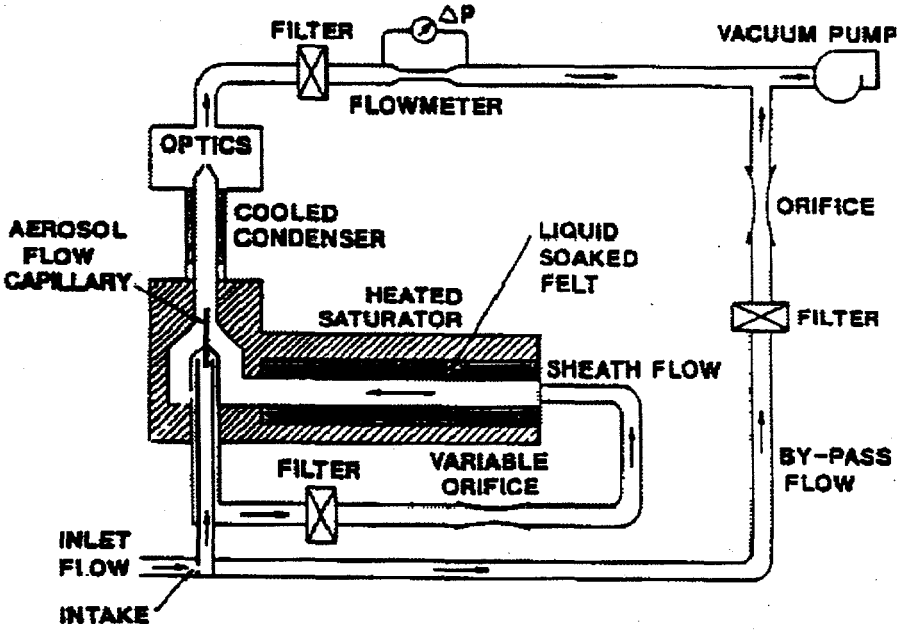

Figure 3.12: Schematic diagram of the condensation nucleus counter

condensation particle counter that uses a vapor sheath technique to improve the instrument's

lower particle size detection sensitivity upto 3 nm. The particles are detected and counted by a simple optical detector after a supersaturated vapor condenses onto the particles causing them to grow into larger droplets. The range of particle detection extends from less than 0.01 particle/cm^3 to $9.99x10^4$ particles cm^{-3}.

The counter uses a laser-diode light source, butanol as the condensing fluid, an internal microprocessor control, a pump, volumetric flow control, and a front panel display of both particle concentration and instrument status.

Diffusion cell

The diffusion cell (Figure 3.13) permits analytical investigations of air pollutants. This analytical investigation requires the continuous generation of known constant concentrations of gases and vapors in order to minimize errors due to absorption on tubing. The diffusion cell main advantage over comparable devices are improved flow geometry which allows very precise calculations of experimental diffusion rates from theoretical diffusion coefficients, ease of operation over a wide range of concentrations, and the ability to maintain constant vapor concentrations over prolonged operating periods.

The diffusion cell was constructed from Pyrex tubing, 8.0 cm long and 3 cm o.d. The diffusion tube, D, which contains the liquid sample, was made from Kimax tubing, 8.0 cm long and 1.1 cm i.d. The diffusion tube holder, E, is an internally threaded glass connector (Ace Glass Catalog No. 7644-15) with a Teflon bushing and "O" ring (Ace Glass Catalog No. 7506-27). The diluent gas enters the cell via tube A. Its flow through the diffusion cell was controlled by a 4-mm Teflon valve, B, and was delivered to the cell chamber, C, through a capillary, F, which is 2 cm long and 1.0-mm i.d. The diluent gas flow rate was monitored by a mass flow controller. The standard vapor mixture leaves the cell through tube H, and can be sampled for analysis through a septum sealing tube, G. When very low vapor concentrations are required, secondary dilution can be employed by introducing the gas mixture from tube H, into a second diluent gas stream.

During operation, about 5 ml of liquid were transferred to the diffusion tube, D which is immediately inserted into the cell and positioned 1 cm below the diluent delivery capillary, F.

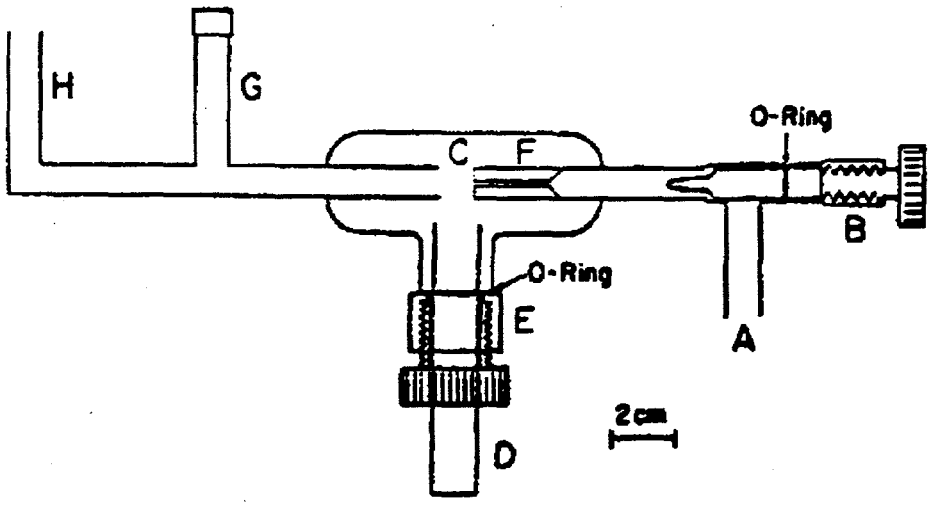

Figure 3.13: The diffusion cell

3.6. Aerosol Generation and Sampling Procedure

Cluster aerosol is generated in the 32 liter cylindrical chamber using radon in purified, compressed gas with/without the addition of water vapor and trace gases. Carrier gases such as N_2, O_2, Air, NO in N_2 and He were used in this study while the vapor of short-chain alcohols, such as methanol, ethanol, propanol, n-butanol and 2-butanol, could be added as trace gases. The composition of some of these carrier gases are tabulated in Table 3.3. From Table 3.3, it can be seen that the commercially available compressed gases used are of research grade (99.998% purity). The high purity permit investigation of the initial properties of radon decay cluster/particle.

When the support gas is compressed air, it is passed sequentially through a first stage air dryer (Dayton Electric MFQ Co.), a high efficiency air dryer (Balston Filter Products), a silica gel, activated charcoal and 13X molecular sieve columns to reduce the moisture content and to remove unwanted organic vapors. It is then passed through an absolute filter for the removal of particulate contamination.

In order to study the effect of each alcohol on the initial properties of freshly-formed radon progeny, the vapor of the chosen alcohol is introduced into the radon-laden airstream with the aid of the diffusion cells. The concentration of the alcohol in the gas stream is subsequently determined by weighing the diffusion tube both before and after a given period of time. The difference between the two values gives the mass of alcohol that evaporated into the gas-stream.

In cases where the combined effect of trace alcohol and water are investigated, two diffusion cells are used in parallel. One containing water and the other containing alcohol as shown in Figure 3.10.

Table 3.3: Specifications for the gases used in this study

Gases	Minimum Purity	Contaminant Species (ppm)
O_2	99.99	THC* < 20; AR < 20 N_2 < 55; H_2O < 3 CO < 3; Kr < 15
N_2	99.999%	H_2O < 3 O_2 < 5
He	99.995	H_2O < 3 N_2 < 5

*THC - Total hydrocarbon

Since the usefulness of any particle-sizing device is determined by how accurately it can measure what is considered to be known somewhat accurately, the system was tested with generated particles that have been previously measured by the earlier investigators (Ramamurthi, 1988) for comparison purpose. The particles are generated by using compressed N_2 gas to supply nitrogen at a mass flow controlled rate through the two flow-through radon gas sources (Pylon-1025). The radon-laden nitrogen, 0.2 liters per min^{-1} (STP) was then passed through a 0.8 μm Millipore filter to remove any decay products and particulate contaminants before being mixed with the dilution gas, 0.7 liters min^{-1}, in the mixer manifold. Then the mixed gas flows into the chamber where the number of particles formed is a function of the residence time. The system is allowed to come to a steady state which can be attained in about 3 hours. The particle concentration is assumed steady if for a given orifice-to-plate distance, the number of particles collected in three consecutive 35-min sampling period agree within 10%.

After attaining steady state, samples are then taken with the hypersonic impactor. The vacuum pump is turned on, and three 35-min are taken for each orifice-to-plate distance, L. As the samples are being taken, there is simultaneous counting of the radioactive ^{218}Po and ^{214}Po nuclide deposited on the impaction plate and, to ensure complete decay of all the deposited ^{218}Po nuclide, the counting is continued for another 10 min, about three ^{218}Po half lives, after

the end of the sampling period. A record of the number of collected particles is made for each value of L.

However, the total number of particles entering the impactor could not be determined because the commonly used instruments, CNC and OPC (optical particle counter), can not detect particles generated in the radon chamber of this study. Thus, for each sample, the collection efficiency can not be determined and the number of collected particle is used instead, assuming a steady inflow of particles.

3.7. Data Inversion - Procedure for estimating aerodynamic diameter

The principal design parameter for an impactor with sharp separation efficiency curve is the position of the step which is generally the value $\psi_{1/2}$ of the Stokes number at which 50% of the particles are captured (de la Mora, 1990). Given the nozzle geometry (round or rectangle), the carrier gas, its temperature, and the pressures P_o and P_1, the collection efficiency, E, depends only on L and the particle aerodynamic diameter, d_{ae} , in the limit of high Reynolds number. Thus, given a particle of unknown aerosol size the particle's aerodynamic size can be estimated as follows:

●From the experimental plot of counts(L) against L, $L_{1/2}/d_n$ will be determined from the curve. This spectral variable $L_{1/2}$, measured in the middle of each step in the counts(L) curve, is a unique function of the aerodynamic diameter of an unknown aerosol. A discrete aerosol spectrum, therefore would be represented by a counts(L) curve with finite number of steps. Each step would have its associated value of the spectral variable $L_{1/2}$ and a corresponding aerodynamic diameter.

●Calculate ψ_0

$$\psi_o = \frac{\psi_{1/2}/(L_{1/2}/d_n)}{G(x)} \qquad (3.1)$$

where G(x)=32.02 and for particle impaction, de la Mora *et al.* (1990a) has shown that $\psi_{1/2}\sim 1$ for

$$0.8 < \frac{L}{d_a} < 0.13\sqrt{\frac{p_o}{p_1}}$$

Then, combining equation (3.1) and (2.50) and re-arranging gives:

$$d_{ae} = \rho_p d_p = \left(\frac{1}{32 L_{1/2}/d_n}\right)\left(\frac{d_n p_o}{0.1309\sqrt{\frac{\pi}{\gamma}c_o^2}}\right) \tag{3.2}$$

Figure 3.14 shows a plot of d_{ae} against $L_{1/2}/d_n$ for d_n=0.2 mm, γ=1.4, c_o=34 x 10^3 cm/s and P_o=1.01 x 10^6 dyn cm^{-2} and a sample of the calculation of d_{ae} values in Figure 3.14 is presented in the next section.

The data inversion can be briefly summarized as follows: First, using the experimental data, a plot of the particle counts against L/d_n is made. For a fairly monodispersed aerosol, the efficiency curve should have a single characteristic "S" shape curve like the traditional impactor. If the aerosol is polydispersed, then there will be several steps. Next, the value(s) of $L/d_n(=L_{1/2}/d_n)$ that corresponds to 50% collection efficiency or the middle of the curve(s) is/are estimated. The corresponding d_{ae} can then be estimated either from equation (3.2) or from Figure 3.14.

A more accurate d_{ae} of the unknown aerosol could be obtained if the hypersonic impactor were calibrated with standard aerosol particles. However, this is currently not possible due to the difficulty associated with the generation of a standard calibration aerosol in the 1 nm range.

3.8 Sample Calculations

According to the definition of the aerodynamic diameter (d_{ae}), diameter of a unit density (1 g cm^{-3}) sphere having the same settling velocity as the given particle

$$d_{ae} = \rho_p d_p \tag{3.3}$$

The derivation of equation 3.3 is given in Appendix A.

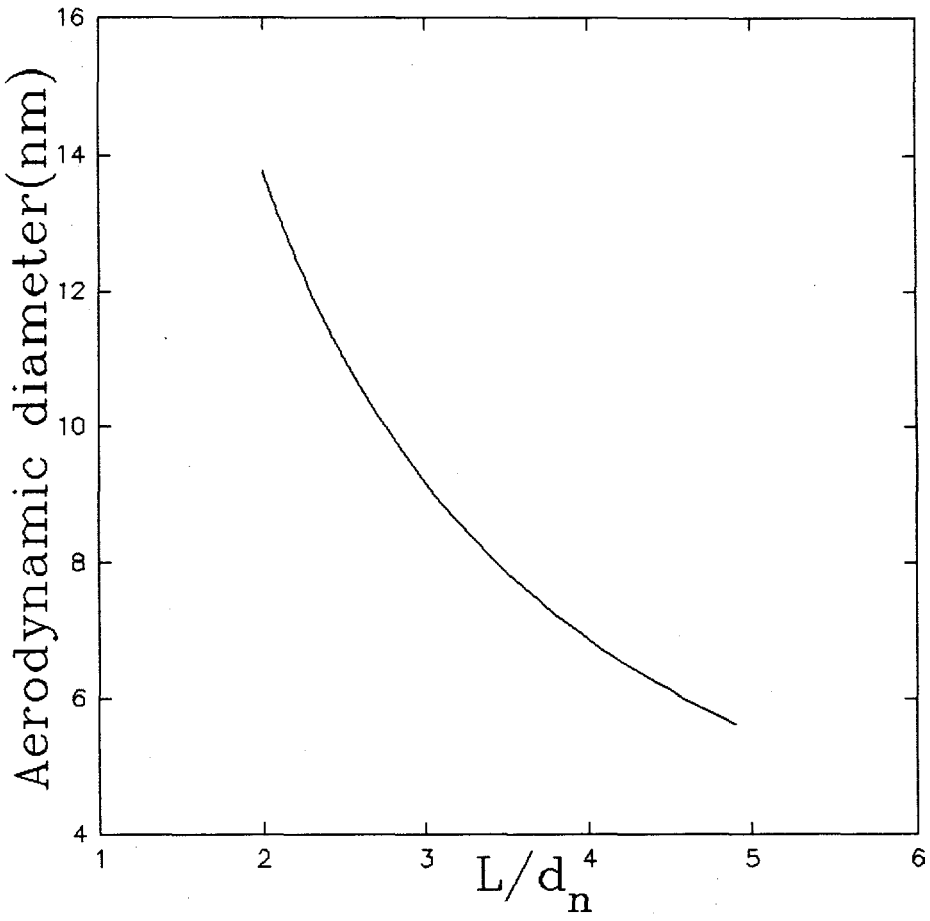

Figure 3.14: Plot of aerodynamic diameter, d_{ae} against $L_{1/2}/d_n$ for d_n=0.02 mm, γ=1.4, P_o=1 atm, c_o=340 m/s.

substituting the values of c_o, P_o, d_n, and γ in equation (3.2) gives:

$$d_{ae} = \frac{8.91 \times 10^{-5}}{32(L_{1/2}/d_n)} \text{cm}$$

For a $L_{1/2}/d_n = 4$

$$d_{ae}=6.96 \times 10^{-7} \text{ cm} \approx 7 \text{ nm}$$

3.9 Summary Remarks.

The important design features of the system have been presented in this chapter. The system is very versatile. A particle size distribution can be scanned by simply changing the orifice-to-plate distance, L. The precautions necessary for the successful operation of the system were also highlighted. The experimental systems used for the system testing was also presented. The major feature of the experimental system, apart from the HI, is the cylindrical chamber where the clusters are generated under well controlled laboratory conditions. The results of the system test are presented and discussed in chapter 4.

It is worth noting that the data inversion procedure presented in this chapter was employed because of two fundamental problems with the experimental system. The problems are: (1) the HI was not calibrated with test aerosol due to the non-availability of standard test aerosols in the less than 1 nm range; (2) inability to measure the particle concentration of the aerosol flowing into the HI system during a given sampling period. The HI system performance can be considerably improved by addressing those two problems.

Chapter
FOUR

RESULTS AND DISCUSSION

In all the impactor response curves presented in this section, the circles (symbol) are the experimental data points and the error bars show the standard error of the mean with 90% confidence level. As a rule of thumb, curves such the one shown in Figure 4.1 with one step size change indicates that aerosol is fairly monodisperse while curves like Figure 4.10 with more than one peak suggest a polydisperse aerosol. Since a response curve to a polydispersed aerosol should have a stair-step type of pattern, the assumption of a polydispersed aerosol for non-monotonic response curves with more than one peak seems counter-intuitive. The justification for this assumption will be presented in great details later in this chapter.

The $L_{1/2}$ for each steep portions on the curves were estimated by finding the average of the L_{min} and L_{max}, where L_{min} and L_{max} are the values of L corresponding to the lowest and highest positions, respectively, on each steep portion. The estimated value was then used to compute the particle size using the procedure presented in chapter 3.

Though most of the results presented in this chapter agrees with previously measured values, the results should be used with care. This is due to some of the simplifying assumption made in estimating the values. A more accurate and precise value is possible if the system is calibrated with standard aerosol in the less than 2 nm, which is currently not possible.

4.1. System Test Results

The first experiment was for radon progeny particles generated in an environment of high purity research grade nitrogen that is better than 99.99% pure. In pure nitrogen, $^{218}Po^{+}$ is presumed to be neither chemically bounded nor form molecular clusters with the nitrogen molecules because nitrogen is an inert gas. These ^{218}Po aerosol particles/clusters have diffusion coefficient, D, ranging from 0.044 - 0.079 cm^2/sec in N_2 environment, depending on the degree of neutralization of the $^{218}Po^{+}$ ion (Goldstein and Hopke, 1985). The collection efficiency curve obtained for the radiolytic particles formed in the case of Rn in dry N_2 is shown in Figure 4.1.

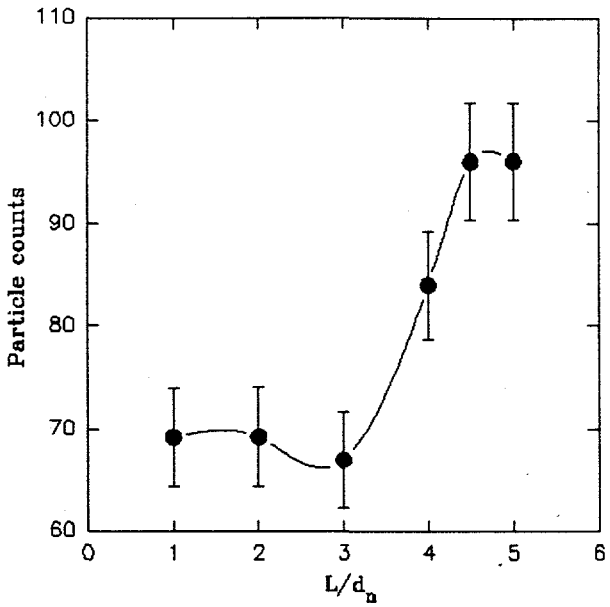

Figure 4.1: Collection efficiency for ^{218}Po particle/cluster in a 99.999% pure N_2 , d_n=0.35 mm and $P_o/P_1 \sim 800$.

For this experiment a 0.35 mm orifice was used with a ratio of stagnation pressure, P_o, to vacuum pressure, P_1, of about 800. The fact that there is a single step signifies that the aerosol generated is relatively monodispersed. Using the value of L/d_n that correspond to the middle of the curve, the d_{ae} of ^{218}Po atom was estimated to be about 13 nm. Compared to previously measured diffusion diameter (Ramamurthi *et al.*, 1993), the d_{ae} of 13 nm was found to be unacceptable. Thus, the nozzle was replaced by a smaller nozzle of 0.2 mm and the experiment was repeated as discussed in the latter part of this section. Using the 0.2 mm orifice, the response curve is similar to the Figure 4.1 and the calculated cluster d_{ae} was 7 nm, which agreed with diffusion diameter measured with graded screens.

It is worth noting the impactor's ability to size-discriminate particles around 1 nm (diffusion-diameter). However, as expected, the collection efficiency does not go to zero below the critical point because particles apparently deposit by diffusion at non-negligible rates.

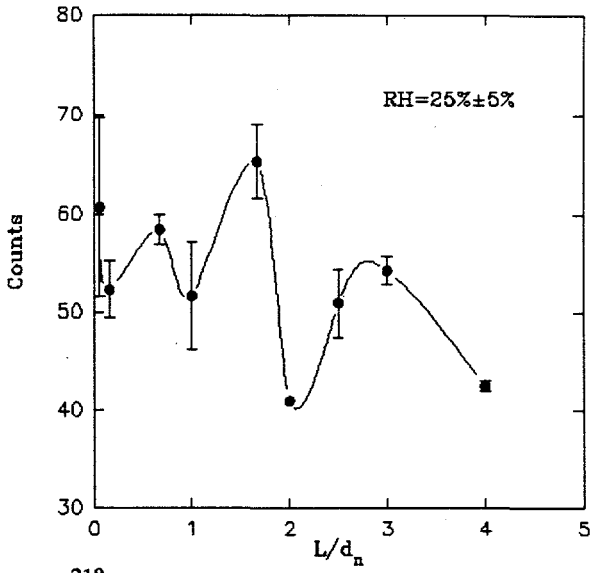

Figure 4.2: Response curve for ^{218}Po particle/cluster in a 99.998%N_2 , d_n=0.35 mm, P_o/P_1~800 and RH=25%.

Because of conflicting reports on the nature of cluster particles formed during radiolysis and its dependence on water vapor concentration (Su *et al.*, 1988 ; Frey *et al.*, 1981), a set of experiments were performed to investigate the Po/H_2O molecular cluster size dependence on increasing RH in a nitrogen environment.

Figure 4.2 shows the initial experimental results for the case when the relative humidity of the gas stream was increased to 25% and for d_n of 0.35 mm, the same orifice used for Figure 4.1. There are three distinct steps ($L_{1/2}/d_n$=0.5, 1.5, 2.5) that corresponds to estimated d_{ae} of 96 nm, 32 nm, and 19 nm, respectively. Note that the inference d_{ae}= 96 nm is very unreliable because of the hypersonic impactor's low resolution below L/d_n of 1. The non-monotonic response is possibly caused by the insufficient pressure drop across the orifice. Furthermore, a closer look at the estimated d_{ae} values suggests that condensation of water molecules in the vacuum chamber has occurred, thereby resulting in the formation of relatively large particles.

The impactor performance can be improved by increasing the pressure drop across the nozzle, which is achieved by either decreasing the nozzle diameter or by employing a higher pumping capacity. We opted for the former. Thus, the 0.35 mm critical orifice was replaced by a thin-plate 0.2 mm platinum orifice, and the experiments were repeated for the cases of RH of

<1%, 10%, 15% and 26%. The results are presented as shown in Figure 4.3.

Figure 4.3 was obtained as follows: (1) normalizing the particle "counts" to take the values of zero and one at the beginning and end, respectively, by using the mathematical relation: $(C - C_{min})/(C_{max} - C_{min})$, where C_{min} and C_{max} represents minimum and maximum counts, respectively, and (2) neglecting the steps in the $L/d_n \leq 2$ range. Though the number of steps present in a curve is an indication of the degree of polydispersity of the aerosol, steps in the $L/d_n \leq 2$ range was found to be mainly due to diffusional deposition or condensation of water molecules because of the jet expansion as previously mentioned. Therefore, these steps are not reproducible because of the stochastic nature of diffusion/condensation processes.

On comparing the curve for RH=26% in Figure 4.2 with solid line curve in Figure 4.3, it can be seen that there was a marked improvement in impactor performance upon increasing the pressure drop, P_o/P_1, across the orifice. Also, the other curves in Figure 4.3 clearly show that the aerosols generated in each case is fairly monodispersed.

Most importantly, an obvious trend can be seen in Figure 4.3 where the value of $L_{1/2}/d_n$ decreases with increasing RH until it reaches a plateau at a RH of about 15%. The estimated d_{ae} are 7 nm, 8 nm, 10 nm and 10 nm for curves labelled as <0.002%, 10%, 15% and 26%, respectively. This demonstrates the sensitivity of the impactor to a relatively small change ($\leq$ 25%) in the particle size. On the other hand, with a RH greater than 15%, the particle size of ^{218}Po remain essentially constant at about a diffusion diameter of about 1 nm (assuming $\rho_p \sim 10$ g/cm^3). Also, the modest increase in particle size observed with increasing RH agrees with: (1) the classical cluster behavior theory prediction that the diffusion coefficient ^{218}Po ions in the presence of pure H_2O should decrease with increasing RH (Raes, 1985; Hawrynski, 1984), and (2) the thermochemistry of ion hydration presented by Castleman (1991). He suggests that increasing the partial pressure of water vapor will only add a few additional water molecules and thus, will not substantially affect the diffusivity of the cluster.

Water molecules can interact with radon in two ways: First. clustering of water molecules around $^{218}Po^+$ (Castleman, 1991); and secondly, neutralization of $^{218}Po^+$ ions by water vapor has been reported as follows (Chu and Hopke, 1988)

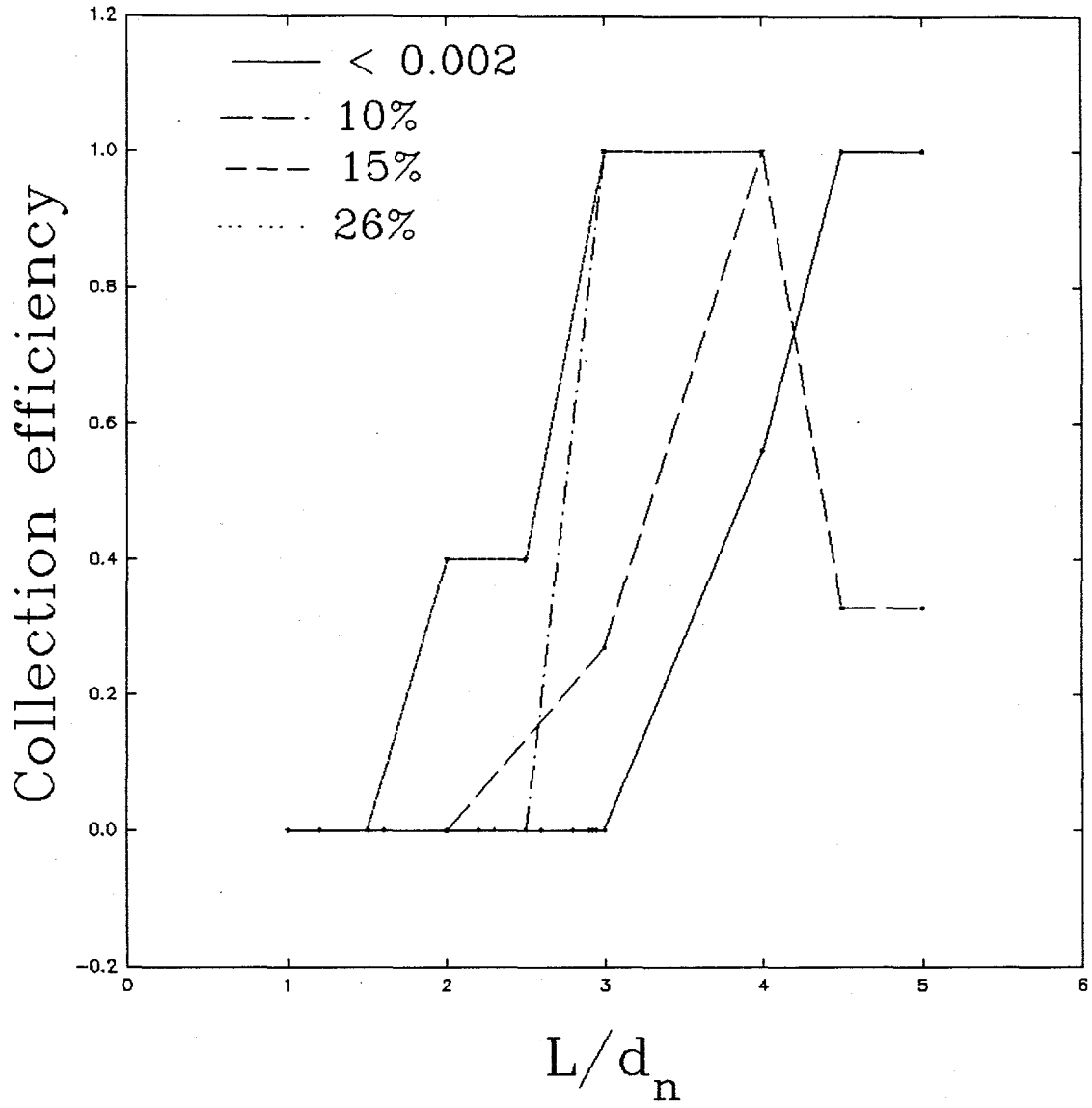

Figure 4.3: Normalized impactor response curve for ^{218}Po particle/cluster in a N_2 environment at various RH, d_n=0.2 mm and $P_o/P_1 \sim 1000$.

$$H_2O \rightarrow \cdot H + \cdot OH \quad (4.1)$$

$$\cdot OH + e^- \rightarrow \cdot OH^- \quad (4.2)$$

$$\cdot OH^- + Po^+ \rightarrow Po + \cdot OH \quad (4.3)$$

The neutralization effect would lead to an effective increase in the D value, thereby causing more particles to deposit on the collection plate for all Stokes number below the critical point where the inertial collection efficiency is supposedly nil. As mentioned earlier, the fact that measured particle sizes increases with increasing relative humidity support the first possibility, clustering of water molecules around the ion.

Finally, the uncertainty in the estimated d_{ae} could be the result of: (1) Assumption that the particles are spherical in shape, no shape factor was used in the estimation (2) Experimental measurement errors, and (3) Simplifying assumptions made in the derivation of equation (3.2).

In conclusion, the comparison of the system test result to previous results showed that the hypersonic impactor has been successfully adapted to measure the d_{ae} of radioactive particles. In addition, the initial tests of the system with radon progeny molecular clusters in the less than 1 nm range showed that the system performance is relatively good for monodisperse aerosol. However, the system collection efficiency curve does not go to zero below the critical point because of high diffusional deposit of the particles, thereby decreasing the system sensitivity.

4.2 Nature of Cluster Aerosol in various Support Gases.

After demonstrating good performance by the system, it was subsequently used to investigate the nature of the same $^{218}Po^+$ in several other carrier/support gases. These support gases were chosen based on various reasons. Qualitative comparison of the results for different carrier gases were then made to provide a better understanding of the nature of $^{218}Po^+$ in those gases.

4.2.1. Cluster Aerosol in Pure O_2

Initial properties of radon progeny in oxygen was investigated because of the following: First, the current controversy regarding the nature of the association of oxygen with ^{218}Po. It is unclear whether the association, if there is any, is strong or weak. Castleman (1991) has postulated that O_2 forms a very weak association with $^{214}Pb^+$, $(Pb^+).(O_2)$ that is expected to be easily broken in a low pressure region. $^{214}Pb^+$ might be expected to have a somewhat similar behavior to $^{218}Po^+$. On the other hand, thermodynamic data predicted that the polonium metal should also react with oxygen to form Polonium oxide ion and release about 3.7 eV of chemical energy (Busigin *et al.*, 1980). Secondly, O_2 is about 20% of the indoor air and therefore should contribute to the changes in the initial properties of radon progeny. However, this contribution is yet to be investigated.

Here, the same experimental system as the one presented in chapter 3 was used except that N_2 was replaced by O_2. Thus, O_2 was used as both the carrier gas and the dilution gas. The impactor response curve obtained for this case is shown in Figure 4.4. Unlike Figure 4.1, it has an unusually high background at the tail end, which makes further experimental investigation of

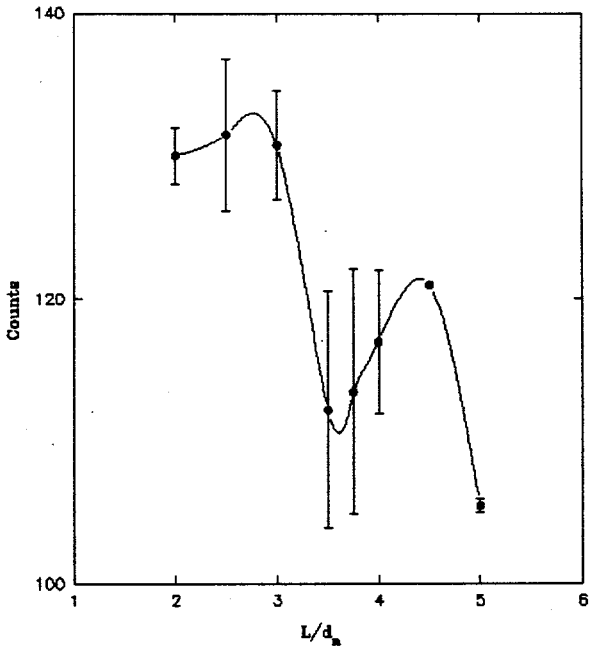

Figure 4.4: Response curve for cluster aerosol in O_2, d_n=0.2 mm and p_o/p_1~1600

the effects of trace gases practically impossible. Therefore, the nature of the association of

oxygen with polonium could not be ascertained.

The high tail end could be as a result of two mechanisms (1) formation of particles > 3 nm and (2) increased neutralization of the charged clusters which subsequently lead to more effectively diffusive clusters. Since the CNC count was zero during the experiment, the first mechanism was eliminated. To check the second possibility, the same experiment was repeated with N_2 containing 0.1% NO. NO has been shown both experimentally and theoretically to be very effective in neutralizing charged Po ions (Frey *et al.* 1981; Goldstein and Hopke, 1988). The response curve obtained for the same aerosol in NO in N_2 as shown in Figure 4.5 is similar to that of oxygen, thereby confirming the second possibility. The high tail end suggest increased neutralization of the $^{218}Po^+$ in O_2 which results in an increase in the particle's diffusion coefficient (Chu and Hopke 1988). However, similar measurements made for radon laden support gas of N_2 with less than 20% O_2 content produced the response curve similar to Figure 4.1. Ditto for Air, which has an oxygen content of about 21% (Scetion 4.2.2). The reason for this inconsistency in the O_2 results could not be explained.

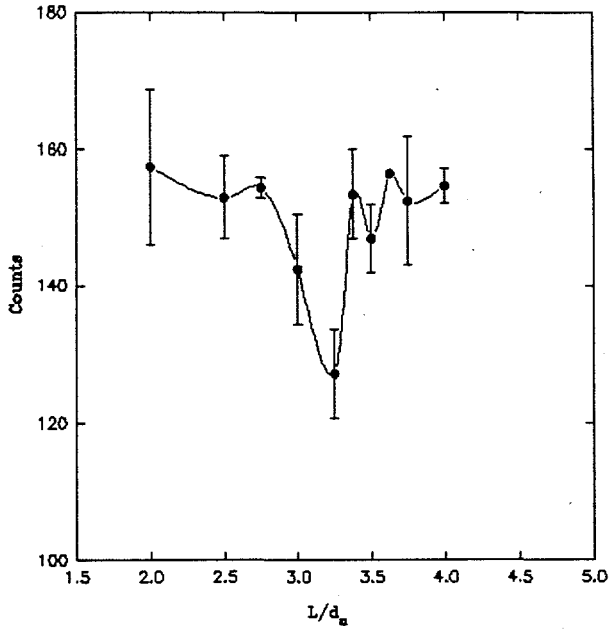

Figure 4.5: Response curve for cluster aerosol in N_2 with trace NO, d_n=0.2 mm and P_0/P_1~1600.

Three mechanisms of neutralization of ^{218}Po-electron transfer, electron scavenging and small-ion recombination have been suggested by Frey *et al.* (1981), and Chu and Hopke (1988).

Since decay of radon usually result in the production of ions and electrons in the carrier gas, oxygen could pick up electron to form an ion and then neutralize the charged $^{218}Po^{+}$ as follows:

$$o_2 + 2e^- \rightarrow o_2^- \qquad (4.4)$$

$$o_2^- + Po^+ \rightarrow Po + o_2 \text{ or } (Po^+)(o_2^-) \qquad (4.5)$$

The neutral ^{218}Po is more diffusive than the charged species due to the interaction of the latter with the gas molecules (Ramamurthi and Hopke, 1990). Apparently, there will be little or no interaction of radon progeny with trace gases in pure O_2 since only charged progeny can form clusters with trace gases (Castleman and Tang, 1972). However, if the trace species have a large dipole moment, they could induce monopole-dipole interaction with Po but the interaction would be relatively weak. Consequently, the investigation of interaction of radon progeny with trace gases in O_2 was discontinued.

4.2.2. Cluster Aerosol in Purified Air

Purified air (RH=4% at 20°C) is also used to have a better understanding of the actual behavior of the radioactive clusters in real indoor air. The results can then be compared to those of the separate measurements made in O_2 and N_2.

Here, the aerosol generation and sampling procedure is nearly the same as the one presented in chapter 3 only that N_2 was replaced by purified air as the dilution gas. N_2 was still used to carry radon through the source. Unlike in the other cases, air was not used as carrier gas through the radon sources because of its high moisture content which is detrimental to the sources.

Figure 4.6 shows the the impactor response curve obtained. Unlike the case of pure O_2, the high tail end is absent in response curve for purified air. Thus, oxygen concentration seems not to be sufficiently high enough to have appreciable effect on the properties of $^{218}Po^{+}$ present in air. As previously mentioned, the reason why the relatively high concentration of oxygen in air does not undergo any noticeable interaction with polonium ions in the same manner as in pure oxygen is not understood.

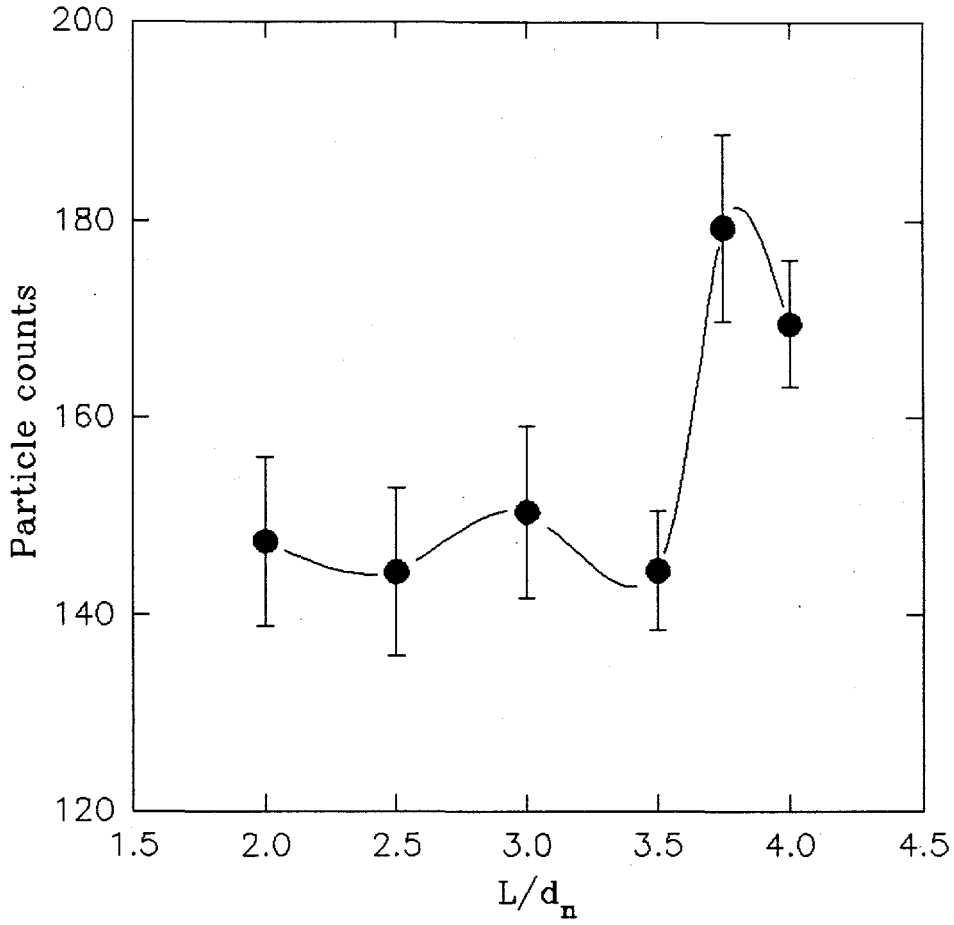

Figure 4.6: Impactor response curve for cluster aerosol in purified air, d_n=0.2 mm and p_o/p_1~1600.

4.2.3. Cluster Aerosol in Pure He

In the course of the review of the initial report of results (Olawoyin *et al.*, 1995), one of the reviewers suggested that the use of He or H_2 rather than N_2 will greatly improve the resolution and reduce the relative importance of diffusion effects. The reviewer argued that impactor resolution tend to increase with the ratio of the masses of the carrier gas molecules and the seeded clusters. Therefore, the response of the hypersonic impactor to the same particles in helium, particle-carrier gas ratio ~ 55, was determined and compared to that obtained for the case when N_2 was used as a carrier gas, particle-carrier gas mass ratio ~ 7. Figure 4.7 shows the

response curve obtained for the case of helium. It can be seen that the curve is not qualitatively different from that of nitrogen (Figure 4.1). However, the particle counts in Figure 4.6 are much lower than those in Figure 4.1 due to the increased volumetric flow into the chamber during the measurements. The increased volumetric flowrate consequently resulted in decreased pressure ratio across the orifice.

The reason for not observing improved resolution, as one would expect, might be due to the fact that high gas-particle mass ratio is offset by the increased particle diffusion coefficient in helium. A particle's diffusion coefficient increases with decreasing support gas viscosity.

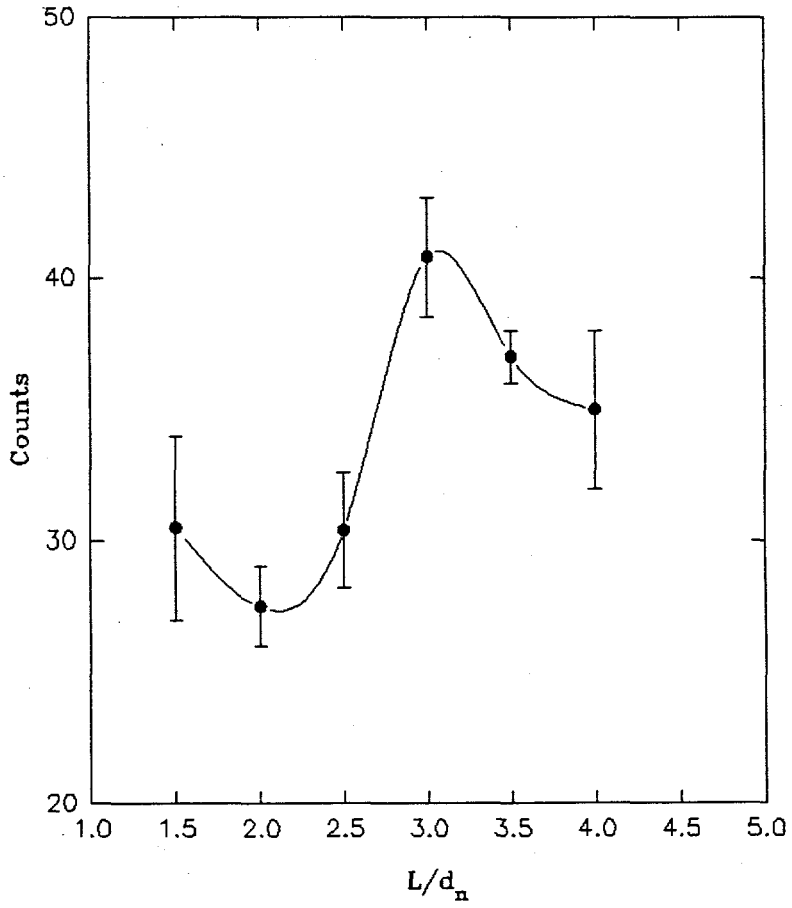

Figure 4.7: Response curve for cluster aerosol in prepurified helium, d_n=0.2 mm and P_o/P_1~760.

4.3. Volatile Organic Compounds

Keese and Castleman (1989) have discussed the potential for forming molecular clusters from organic compounds in the ambient atmosphere. However, they did not evaluate the formation of clusters of indoor air organic compounds around the ions produced by the decay of radon, which was done recently by Daisy and Hopke(1992). Although the neutralization of the polonium ion may occur before it can serve as a nucleation site, there are 167,000 ion pairs produced by the passage of the 5.5 MeV α and the recoiling Po nucleus through the air (Lind, 1961). Thus, there are a large number of ions available to serve as nucleating centers for the organic vapor in the indoor atmosphere. The neutral polonium molecule could also potentially cluster around one of these residual small air ions.

Indoor atmospheres contain many vapor-phase organic compounds that may interact with radon progeny to form ion clusters. Over 300 volatile organic compounds (VOC) have been detected in indoor air (Berglund *et al.* 1986). The VOC are generally defined as compounds with vapor pressure $>\sim 10^{-3}$ torr, this include compounds such as the C_4 to C_{16} alkanes, aromatic hydrocarbons, chlorinated hydrocarbons, alcohols, aldehydes, ketones, esters, terpenes, ethers, and heterocyclics. These VOCs are present in indoor air as a result of many processes that includes infiltration of outdoor air containing VOC, cooking, emissions from building materials, consumer spray products, etc. Mean concentrations of individual compounds in established buildings were found to be generally below 50 $\mu g/m^3$, with most below 5 $\mu g/m^3$. Concentrations in new buildings were much greater, often by an order of magnitude or more, and appeared to arise from construction materials and building contents. For detailed review of investigations of VOCs concentrations in indoor air of buildings of different classifications (dwellings, offices, schools, hospitals) and categories (established and new buildings), see Brown *et al.* (1994). The VOC investigated in this work are the short-chain alcohols.

4.3.1 Short-chain Alcohols

Alcohol occur throughout nature and have wide spread industrial applications. For example, ethyl alcohol is second only to water as a solvent in the manufacture of drugs, plastics, lacquers, plasticizers, perfumes, cosmetics, detergents, rubber accelerators, window cleaner spray, hair spray, deodorant stick or an antiperspirant and many others. Use of ethanol as a motor fuel is growing in the United States. The use of these household products could lead to significant increase in VOCs concentration in indoor environments.

The radon progeny interaction with alcohols listed in Table 4.1 was investigated. The alcohols physical properties are also given in the table. Values of saturation vapor pressures (at 25°C), surface tension (at 25°C), dielectric constant, density (at 25°C) and molecular weight for these alcohols and water were compiled from the CRC Handbook of Chemistry and Physics, 70th Edition (1989). The surface tension in Table 4.1 refers to the liquid-vapor interface where both phases are in equilibrium, measured and expressed with air as the vapor state. Similarly, the dielectric constant were measured in air at a temperature of 25°C and an electrical frequency of about 200 kHz. Dielectric constant relates to the force of attraction between two electrically charged plates with opposites charges. A substance with a high value for dielectric constant is one which provides a strong interaction with the applied force.

Table 4.1: Properties of the VOCs used in this study

Component	Molecular Weight (g)	Saturation Vapor pressure (mmHg)	Surface Tension (dyn/cm)	Dielectric Constant	Density (g/cm^3)
Methanol	32.04	139.70	22.61	32.63	0.7914
Ethanol	46.07	62.60	22.75	24.30	0.7893
Propanol	60.10	24.24	23.78	20.10	0.8035
Butanol	74.12	8.51	24.60	17.80	0.8098
2-Butanol	74.12	12.51	23.50	15.80	0.8078
Water	18.00	23.76	71.98	78.40	0.9969

It is worth-mentioning that there is a potential problem with sampling of cluster aerosol containing trace amount of VOCs with a low pressure impactor. Organics can vaporize or condense in the low pressure chamber, depending on the vapor pressure of the organic. Condensation can be categorized as either homogenous, where the phase transitions occurs in the absence of the ions and the foreign surfaces, or heterogenous, where the formation of the new phase is enhanced by the pre-existing ions or particles.

To prevent condensation of the low pressure organics in the chamber, sufficiently low concentration is maintained in the carrier gas. Condensation of the organic or water vapor can

be easily detected by the size of particle, > 2 nm, formed in the chamber. However, the possible evaporation of clustered alcohol molecules in the low pressure of the impactor region could not be controlled. Before presenting the results, it would be worthwhile to review the theory of cluster formation.

4.3.2 Classical Theory of Cluster Formation - Thomson Theory

The formation of clusters of vapors and gases about ions is essentially an atomic/molecular level process. However, the classical theory of charged liquid droplet formation (Thomson, 1988; Castleman *et al.*, 1978; Chan and Mohnen, 1980), that is based on the macroscopic properties of the clustering species, has often been used to describe this process (Castleman, 1982; Raes, 1985). In this theory, the Gibbs free energy of cluster formation around an ion is described by the Thomson equation:

$$\Delta G = -nkT\ln S_{sr} + 4\pi r^2\sigma + \frac{q^2}{2}\left(1-\frac{1}{\epsilon}\right)\left(\frac{1}{r}-\frac{1}{r_o}\right) \qquad \textbf{(4.6)}$$

where ΔG is the free energy required to form a cluster of radius r, with an ion core of radius r_o, S_{sr} is the saturation ratio=P/P_{sat}, P is ambient vapor pressure of a compound, P_{sat} is the saturation vapor pressure of the compound at temperature T, n is the number of vapor molecules in the cluster, k is the Boltzman constant, T is the temperature in degrees K, σ is the surface tension of the compound, q is the charge of the ion, and ϵ is the dielectric constant of the organic compound. The variables n and r are related by:

$$\frac{4}{3}\pi\rho r^3 = \frac{nM_{wt}}{N} \qquad \textbf{(4.7)}$$

where ρ is the bulk density of the clustering compound, M_{wt} is its molecular weight, and N is the Avogadro's number; Thus, the ratio of M and N is the mass of a molecule of the compound, say m.

Assuming volume additivity, the mass of clustering compound, M_c, in a cluster of radius r around an ion radius r_o is:

$$M_c = \left(\frac{4\pi}{3}\right)(r^3 - r_o^3)\rho \qquad \textbf{(4.8)}$$

M_c can furthermore be given by the product of the number of clustering molecules in the cluster and the compound molecule mass:

$$M_c = nm \tag{4.9}$$

so that the number of clustering molecules, n, in the cluster can be calculated from the cluster radius by combining equations (4.8) and (4.9).

Substituting equations (4.7) in (4.6) gives:

$$\Delta G = -\left(\frac{4\pi r^3}{3m}\right)\rho kT \ln\frac{p}{p_{sat}} + 4\pi r^2\sigma + \frac{q^2}{2}\left(1-\frac{1}{\epsilon}\right)\left(\frac{1}{r}-\frac{1}{r_o}\right) \tag{4.10}$$

The first term on the right of equation (4.10), G_1 , accounts for the release of latent heat of vaporization and is positive unless the condensing vapor is present in the atmosphere at supersaturation levels. The second term, G_2, represents the free energy barrier due to the surface tension of the liquid droplet and is also positive. The last term of the equation, G_3, contributes to the lowering of the cluster free energy due to the presence of the ion and is negative. Stable cluster will form only if there is a negative minimum in ΔG.

Because the classical theory is based on the bulk properties of liquids at a macroscopic level and does not take microscopic effects into account, several investigators have developed theories to correct for the molecular level effects such as polarizability of vapor molecules, the orientation and the overall configuration of the vapor molecules. For example, Chan and Mohnen (1980) developed an empirical-analytical semimolecular theory to correct for molecular effect. The same model also corrects for the change in surface dipole-diploe interactions. The overall effect of these corrections for water molecules clustered about a Cs^+ ion is to approximately double the negative value of ΔG that is calculated using the classical theory which agrees with the observation of Castleman and co-workers(1978).

Castleman and co-workers (1978) compared the predictions of the classical droplet theory to some experimental measurements of clusters of water and ammonia about some cations and subsequently found that Thomson equation predicted less negative values for the enthalpy of cluster formation with NH_3 than were observed experimentally for values of n from 1 to ~6. No experimental data were available for the Bi^+ ion with water. The experimental data for clusters

of NH_3 with the Bi^+ ion suggested also that the entropy of formation of these microclusters was more negative than predicted by theory; that is, the clusters have a more ordered structure than accounted for in the classical liquid droplet theory. However, the prediction of the Thomson equation was shown to agree with experimental values at moderate and larger cluster size, $n > 7$. Overall, there findings suggested that the Thomson equation is not generally adequate for treating heteromolecular phenomenon.

Nevertheless, Daisey and Hopke (1993) have used the classical theory successfully to investigate the potential for cluster formation induced by the decay of radon in indoor air containing vapor-phase organic compounds and determine the ones that were most likely to form clusters around the PoO_x^+ ion (and multiple small ions) formed by radon decay. The Thomson equation was used to estimate the Gibbs free energy from the maximum reported indoor concentration as an indication of the potential for ion-induced nucleation for 44 indoor organic compounds. Oxidized hydrocarbons and the semi volatile organic compounds (SVOC) were found to have the greatest potential for cluster formation and estimated cluster diameter of 0.6-1.0 nm.

For the case of water at 4% relative humidity (22^0C and 1 atm) in air, Figure 4.8 presents an example of the variations in the three terms (G_1, G_2, G_3) that contribute to ΔG as a function of cluster radius. The ion is ^{218}Po and its radius was taken to be 0.23 nm. In the same figure, it can be seen that ΔG exhibits a distinct minimum. This pattern is typical for all the compounds investigated in this work.

The measured sizes, in this study, were compared to those estimated from the Thomson equation using the experimentally measured concentration values for the organics and water. The comparison is presented and discussed later in this section.

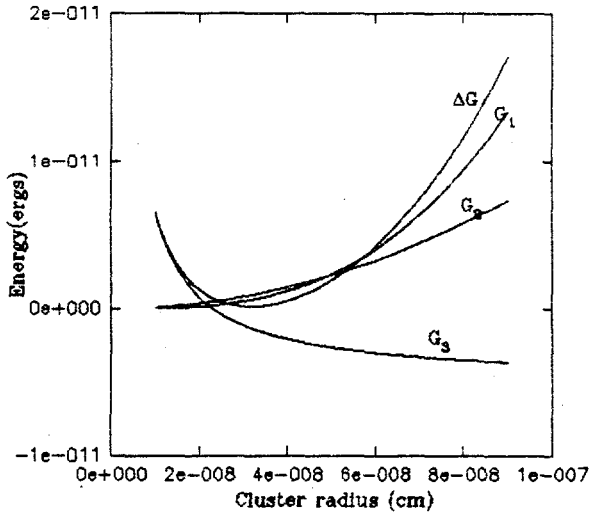

Figure 4.8: Variation in ΔG as a function of cluster radius r for water, $\Delta G=G_1+G_2+G_3$

In the presence of VOC, the impactor response curve is non-monotonic, showing in most cases two dominant humps suggesting the polydisperse nature of the cluster aerosol as opposed to diffusional deposition, a stochastic process.

Theoretically, it is true that a multimodal distribution should not produce multiple humps as apparent in most of the subsequent figures. However, the presence of the humps could not be attributed to diffusional depositional because in the absence of VOCs when the clusters are most diffusive, an essentially S-shape curve were obtained. Diffusional deposition should result in more humps in this case than in the others and the number of counts should decrease continuously with increasing L/d_n, the nozzle-to-plate separation measured in the unit of the nozzle diameter. Moreover, many studies have shown that the diffusion coefficient of polonium ions decreases in the presence of VOCs.

There are several things that can cause non-monotonic impactor response to cluster aerosol, among them are: (a.) operating the impactor beyond the useful hypersonic range, see chapter 2 (b.) polydispersity of the cluster aerosol (c) evaporation of the cluster aerosol in the low pressure near the detector region (d) unsteady particle flow (e) imperfections in the nozzle (f) non-smoothness of the impaction surface. The fact that a nice S-shaped curve was observed for the relatively monodisperse case, polonium in a pure N_2 environment, suggested that d, e and

f are not the cause with (a) through (c) as the remaining possibilities. To check whether (a) was the cause, the pressure ratio across the orifice was increased from 1000 to about 1600, about 60% increase, and the curve remained the same; that is, the multiple humps persisted. According to de la Mora *et al.* (1990a) non-monotonic response of the impactor can be reduced by increasing the pressure ratio as shown in their Figure 7. Thus, it was concluded that the cluster aerosol in gas with trace VOC was polydispersed with the possibility of evaporation of clustered alcohol molecules as the orifice-to-plate distance, L, increases. As L increases, there is more room for gas expansion which results in the decreased pressure in the impaction region. The decreased pressure could cause the clusterd VOC molecules to evaporate thereby reducing the cluster size and the number of that particular cluster size. This reduction in the size and number concentration seems to result in the multiple humps. Thus, the cluster aerosol in the presence of VOC was assumed to be polydispersed, despite the non-monotonic response. See further proof in chapter five.

More importantly, all the experiments were conducted at a downstream pressure, P_1, less than or equal to 0.9 torr and the upstream pressure, P_o, 760 (1 atmosphere). Therefore, based on the discussion of de la Mora *et al.* (1990a) and Hering and Stolzenburg (1994), the impactor should behave in a well characterized way for $0.8<L_{1/2}/d_n\leq 0.14\sqrt{(P_o/P_1)}=4$ which is the so called hypersonic range.

4.3.3 VOCs in N_2

The experimental results for the methanol, ethanol, propanol, 2-butanol and butanol, are presented and discussed.

Methanol, Ethanol, Propanol, 2-Butanol and Butanol

The impactor curves obtained for 0.58 ppm methanol and 0.30 ppm butanol are shown in Figures 4.9 and 4.10, respectively. The two measurements were made at different concentration because it was found that the dominant cluster sizes in a given aerosol is independent of the organic concentration at least in the ppm concentration range. In this range, the concentration affect only the number distribution of the dominant cluster sizes as discussed in the next section.

There are two dominant cluster sizes in both Figures 4.9 and 4.10, suggesting the polydispersed nature of the generated cluster aerosol. In Figure 4.9 for N_2 with 0.58 ppm methanol, the dominant particle sizes are 12 nm and 7 nm while the dominant cluster sizes in

Figure 4.10 for N_2 with 0.30 ppm butanol, are 25 nm and 11 nm. These values and the estimated cluster diameters in other short chain alcohols are listed in Table 4.2. Since the density of clusters present in the aerosols are not expected to be different, we observed that the size

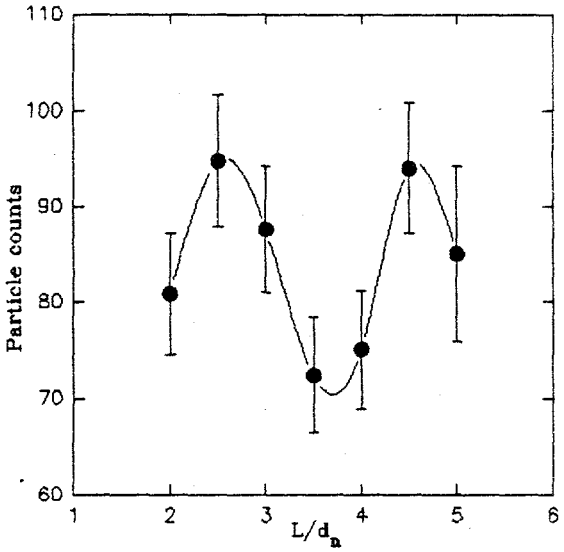

Figure 4.9: Response curve for cluster aerosol in N_2(99.998%) with 0.58 ppm methanol, d_n = 0.2 mm and p_o/p_1~1000.

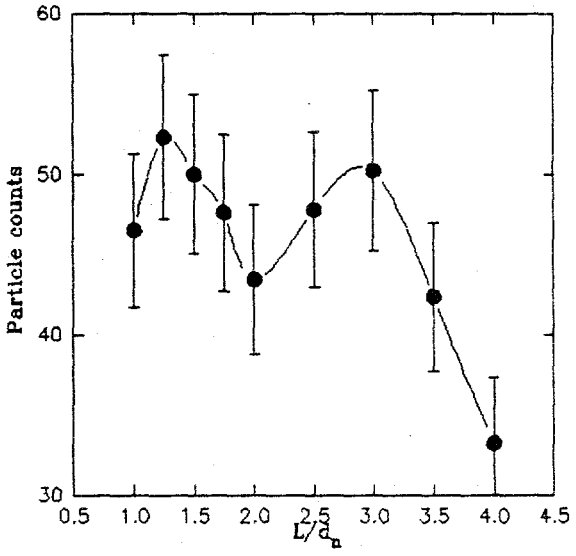

Figure 4.10: Response curve for cluster aerosol in N_2(99.998% pure) with 0.2 ppm butanol, d_n =0.2 mm and P_o/P_1~1000.

of the $^{218}Po^{+}$ cluster in N_2 increases with increasing hydrocarbon chain length. Another interesting observation is that the particle size in 2-butanol is less than the size in n-butanol, two alcohols with the same molecular weight but different structural configuration. This observation agreed with the fact that 2-butanol has a smaller length than *n*-butanol.

However, the result presented here is not complete in itself because typical indoor air will contain certain organics as well as significant amount of water vapor. It will thus be worthwhile to investigate the combined effects of water vapor and each of these short-chain alcohols.

Table 4.2: Dominant ^{218}Po cluster sizes in N_2 with various trace gas phase organic compounds.

Alcohol	Cluster Size (nm)
Methanol	12,7
Ethanol	12,8
Propanol	14
Butanol	25,11
2-Butanol	14,10

Combined Methanol and Water

It has been proposed that addition of methanol to humidified radon gas should result in cluster formation and growth by the substitution of methanol for H_2O in the ion cluster (Yoon *et al.* 1992)

$$Po(H_2O)_x^+ + yCH_3OH \rightleftharpoons Po(H_2O)_{x-y}(CH_3OH)_y^+ + yH_2O \qquad (4.11)$$

$Po(H_2O)_{x-y}(CH_3OH)_y$ will henceforth be referred to as Po-water-methanol cluster. To check the validity of reaction (4.11), experiments were conducted for several methanol-water concentration ratios, 0.7, 1.28 and 6.4 (Figures 4.11 a -c). More water molecule is expected to be substituted with increasing organic concentration, thereby increasing the cluster size. Here, methanol-laden and water-laden streams from the diffusion cells were mixed with the radon-laden N_2 in the mixer manifold. The concentration ratio was varied by adjusting the liquid levels and the

associated flow through each diffusion cell. At all times, the methanol concentration was maintained below 0.7 ppm in order to prevent particle formation by condensation in the expanding jet from the stagnation chamber orifice.

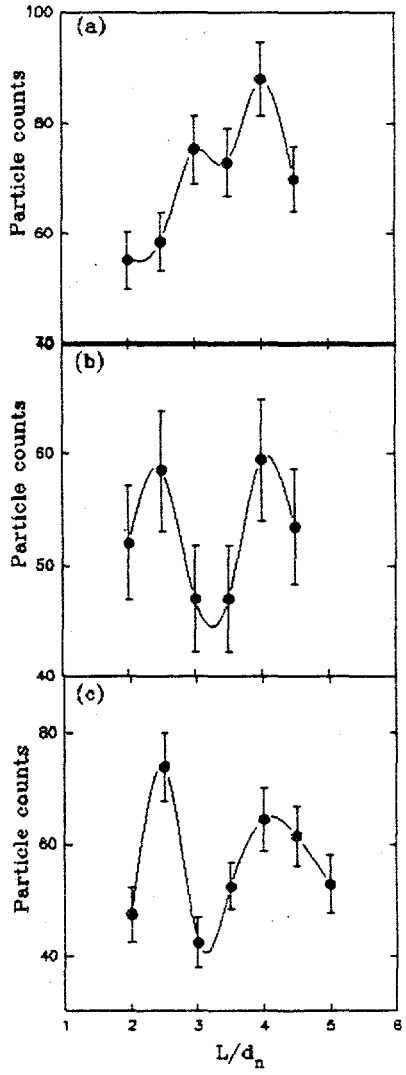

Figure 4.11: Response curves for cluster aerosol in N_2 with various CH_3OH-H_2O concentration ratio (a:0.7; b:1.28; c:6.4)

In Figures 4.11a-c, the presence of two steps, 12 nm and 8 nm, can be clearly observed. Note that the same 12 nm size was observed in the clusters formed in the presence of only methanol. Thus, the 12 nm cluster is referred to as Po-methanol instead of Po-water-methanol cluster as indicated by equation (4.11). Similarly, 8 nm cluster observed here corresponds to Po-water cluster as observed earlier in the experiments with only water.

The experimental results tend to suggest that reaction (4.11) should be used with caution in indoor air modelling because the highest cluster size (12 nm) is the same for the carrier gas with only methanol and the one with both methanol and water. This suggests that x is equal to y in equation (3) and thus, methanol clusters around $^{218}Po^{+}$ ion as follows:

$$Po^{+} + xCH_3OH = Po(CH_3OH)_x^{+} \qquad (4.12)$$

Comparing Figures 4.11 a,b and c shows also that the relative number concentration of the dominant cluster sizes changes with relative methanol-water concentration. The higher the methanol concentration the higher the number concentration of Po-methanol cluster. In other words, more Po ion are converted to Po-methanol clusters with increasing methanol concentration.

Water combined with Ethanol, Propanol, 2-Butanol and Butanol separately

Figures 4.12, 4.13, 4.14 and 4.15 show the impactor results for clusters formed in N_2 with trace amounts of ethanol-water, propanol-water, butanol-water and 2-butanol-water, respectively. The dominant particle sizes for each case are presented in Table 4.3. Table 4.3 also gives the concentration ratio of each organic vapor to the water vapor.

In Table 4.3, unlike in Rn-N_2 gas with either methanol or ethanol, it is observed that the unsubstituted Po^{+} (7 nm) is absent in propanol/water, butanol/water and 2-butanol/water. Thus, almost all the Po-water cluster/particles were able to grow in N_2 with these short chain alcohols suggesting that the clustering of the short-chain alcohols becomes more effective with increasing hydrocarbon chain length. Note that the hydrocarbon chain length is determined by the structural configuration. The observed enhanced particle growth agrees with the earlier observation and the theoretical results of Daisey and Hopke (1993) that showed the potential for cluster formation increasing with hydrocarbon chain length, which is not necessarily linear. The cluster size in 2-butanol (14 nm) was found to be much lower than those in n-butanol. Thus the

size of the resulting cluster formed by a particular alcohol with the ion depend on the structural configuration of the clustering molecule which is consistent with the earlier observation. For example, the maximum cluster size in the presence of 2-butanol is 14 nm, a value much lower than that of n-butanol, 25 nm.

Table 4.3: Dominant ^{218}Po cluster sizes in N_2 with various trace gas phase organic compounds and water vapor.

Alcohol	Ratio	Cluster size (nm)
Ethanol/H_2O	7.00	12,7
Propanol/H_2O	1.75	13
Butanol/H_2O	1.20	25,13
2-Butanol/H_2O	2.00	14

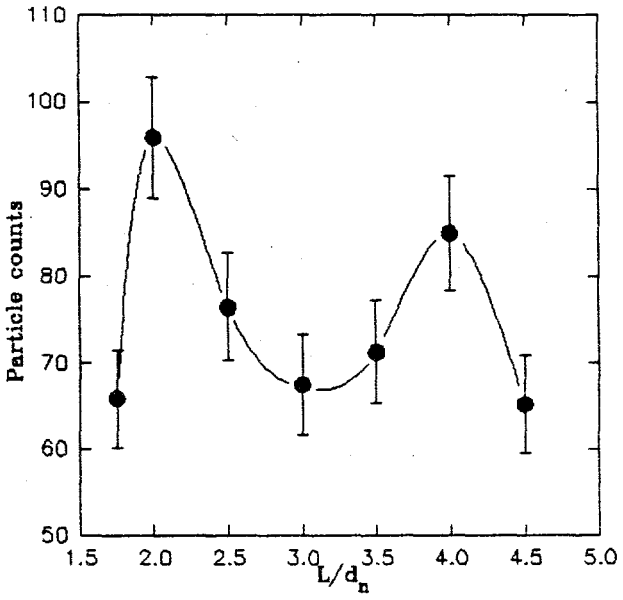

Figure 4.12: Response curve for cluster aerosol in N_2 (99.998% purity) with trace ethanol and water ($[C_2H_5OH]/[H_2O]=7$), d_n = 0.2 mm and $P_o/P_1 \sim 1000$.

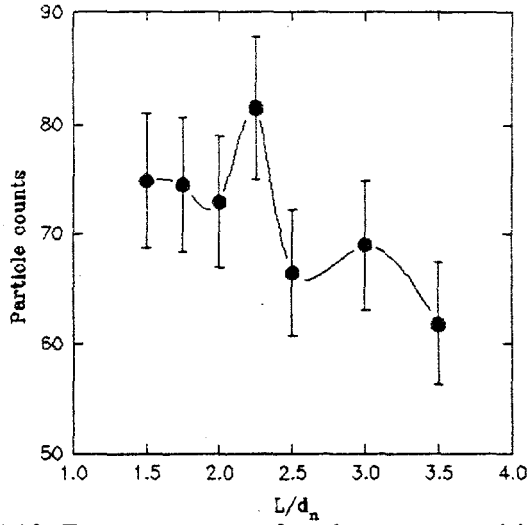

Figure 4.13: Response curve for cluster aerosol in N_2 (99.9985 purity) with trace propanol and water ($[C_3H_7OH]/[H_2O]$)=1.75), d_n=0.2 mm and P_o/P_1~1000.

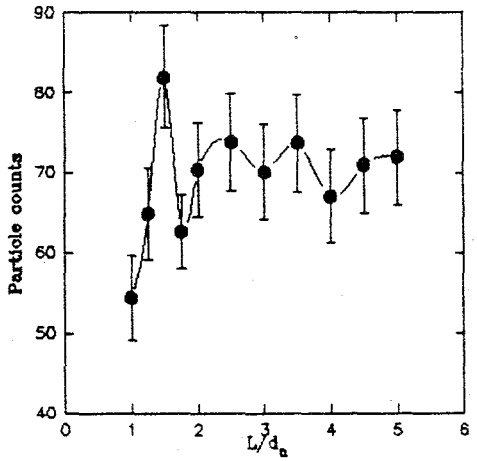

Figure 4.14: Response curve for cluster aerosol in N_2 (99.998% pure) with trace n-butanol and water ($[C_4H_9OH]/[H_2O]$=1.25), d_n=0.2 mm and P_o/P_1~1000.

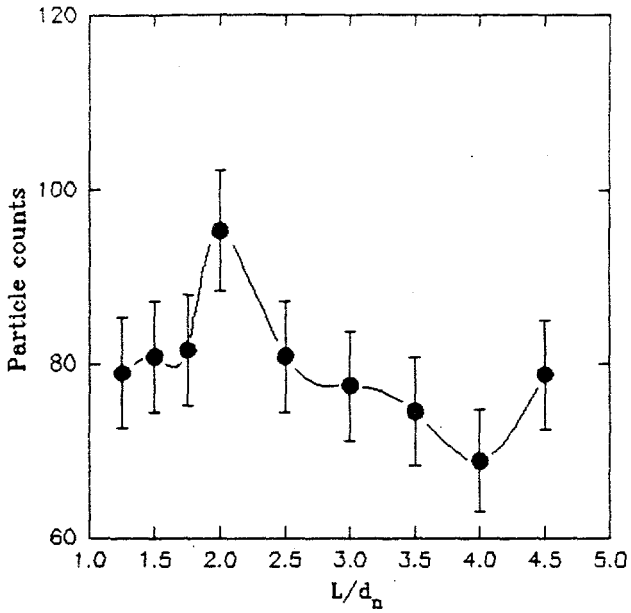

Figure 4.15: Response curve for cluster aerosol in N_2 (99.998% pure) with trace 2-Butanol and water ([2-C_4H_9OH]/[H_2O]=2.0), d_n=0.2 mm and P_o/P_1~1000.

4.3.4 VOCs in Helium

Because of the reason stated earlier, the measurement for helium were made at a pressure ratio, $P_o/P_1 \sim 760$ using the same orifice. The impactor response curves for cluster aerosol formed in helium gas containing trace amount of the short chain alcohols are as shown in Figure 4.16a, b and c. The bimodal nature of the cluster aerosol is demonstrated by the two peaks observed in all the curves. All trends observed earlier for these cluster aerosol in N_2 were also exhibited in helium. For example, the relative size of the bare polonium ion peak, the second peak from left, decreases in intensity with increasing hydrocarbon chain length. Also, the cluster size increases with increasing hydrocarbon chain length.

Comparing the results presented in Figure 4.16 with those of N_2 further confirm the earlier observation that using a relatively low mass carrier gas does not necessarily improve the system resolution.

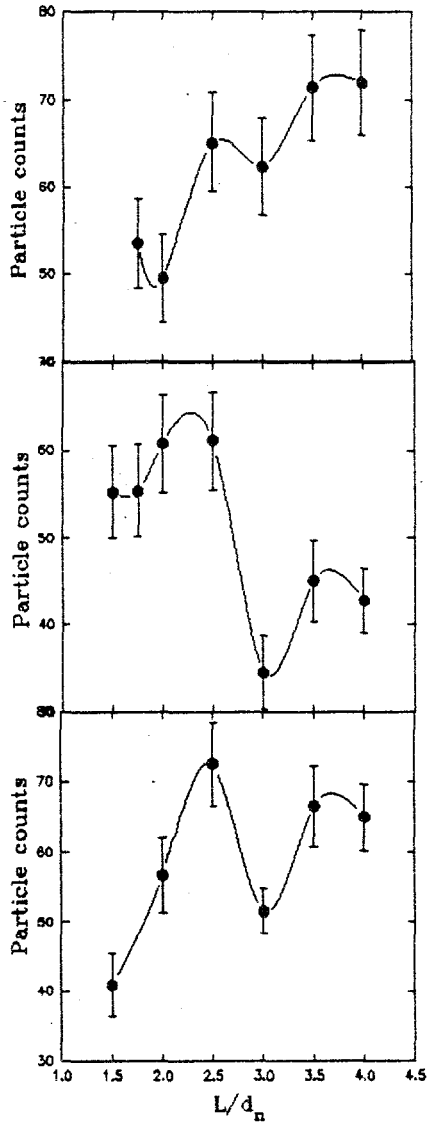

Figure 4.16: Response curves for Helium gas with trace amounts of (a) 0.1 ppm methanol (b) 0.15 ppm ethanol (c) 0.11 ppm propanol.

4.3.5 Purified Air(4% RH at 22°C)

Using the same experimental system described in chapter 3, aerodynamic size distribution of cluster aerosol in purified air with trace water vapor and short-chain alcohols were measured. In addition, the size of cluster aerosol in air with various relative humidity (10%, 15%, 26%) were also measured. The result of the similar measurement made in dry pre-purified N_2 was presented earlier in this chapter.

The result for the purified air can be broadly divided into two: results for cluster aerosol in organic-free support air with increasing RH, and those for support air with one added organic at a time.

Water Vapor

According to the previously discussed clustering theory (Raes, 1985) H_2O molecules will cluster around the ion until a stable radius is reached, implying a balance between the H_2O molecules attaching to and evaporating from the surface of the cluster. For relative humidities from 1 to 100% the time to reach a stable radius is between 5×10^{-5} and 5×10^{-7}s (Strydom *et al.*, 1990) and is characterized by a minimum in the free energy of formation of the cluster. Since a residence time of about 30 min in the carrier gas stream was allowed in this work, the cluster was assumed to have reached equilibrium before size measurement.

The measured aerodynamic sizes at various RH are presented in Table 4.4. From these values, the corresponding physical sizes (d_e) were calculated from $d_{ae}=\rho d_e$ assuming a particle density, $\rho \sim 10$ g cm^{-3}. For comparison purpose, the classical theory of ion-induced nucleation was then applied to calculate the radius and number of H_2O molecules in the clusters for each relative humidity level, assuming a positive charge of one elementary unit. The results of these theoretical calculations together with the number of H_2O molecules estimated from the results of a similar measuements of Strydom *et al.* (1990) are also shown in Table 4.4. Strydom *et al.* (1990) used a mobility spectrometer to measure the mobility size of $^{218}Po^+$ clusters in a similar environment to that of this study, purified air with increasing relative humidity.

Table 4.4 shows discrepancy between the experimentally determined, n_e , and the theoretical prediction, n_{ct}, for the number of clustered water molecules. Similarly, the calculated cluster diameter, d_e, deviates from the corresponding experimentally determined, d_{ct}, value by as much as 43%.

Table 4.4: Comparism of the measured and calculated cluster sizes in purified air at various relative humidity levels.

%RH	d_{ae}(nm)	d_e(nm)	n_e	d_{ct}(nm)	n_{ct}	n_{st}
10%	8	0.8	8	.64	4.3	11
15%	10	1.0	11	.68	4.7	12
26%	10	1.0	11	.70	5.2	13

d_e - physical diameter determined from experimental data; n_e - number of H_2O molecules determined from experimental data; n_{ct} - number of molecules according to classical theory; d_{ct} - physical diameter according to classical theory; n_{st} - number of molecules determined from the experimental data of Strydom *et al.*(1990)

Nevertheless, the trend in the experimental data seems to be the same as the classical predictions, the size of the cluster increases with the relative humidity. In addition, the experimentally determined number of molecules reported by Strydom *et al.* (1990) correspond fairly well with the values found in the present study.

The disagreement between the classical predictions and the two other presented experimental results in Table 4.4 tends to suggest the clustering was dominated by molecular level effects which was not accounted for in the derivation of the classical theory.

VOCs in Air

For short-chain alcohols, the number of molecules and the cluster size together with the estimated values from the classical theory are listed in Table 4.5. The estimated cluster diameter, d_e, differs from the theoretical prediction, d_{ct} , by as much as 62% while the estimated number of molecules, n_e, differ by factors ranging from 7 to 2 from the theoretical predictions. Unlike in the case of nitrogen, the cluster size does not increase with the hydrocarbon chain length; the average size was found to about 1.0 nm. In addition, with the exceptions of methanol and ethanol, there is a much better agreement between the experimental and theoretical values than the one observed in the case of air with increasing relative humidity. In this case, it seems $(Po^+).(O_2^-)$, a dipole, is formed. $(Po^+).(O_2^-)$ could then interact with the dipole of the organic to induce clustering. The polarizability of the organics decreases from methanol to butanol.

Thus, the effect of the dipole interaction on clustering decreases as one goes down the table which consequently lead to better agreement between the experimental and theoretical values for the high molecular weight alcohols. However, it is worth-noting that the values for both n_e and n_{ct} follow nearly the same pattern.

Table 4.5: Comparism of the measured and calculated cluster sizes in air with trace VOC.

VOC	d_{ae}(nm)	d_e(nm)	n_e	d_{ct}(nm)	n_{ct}
Methanol	12	1.2	10	0.72	2
Ethanol	12	1.2	7	0.72	1
Propanol	9	0.9	2	0.72	1
n-Butanol	10	1.0	2	0.72	1
2-Butanol	10	1.0	2	0.72	1

Above all, the measured cluster diameter of about 1 nm in Table 4.5 is consistent with the previously measured diffusion diameters of Po cluster in similar environments (Frey *et al.* 1981).

Thermodynamic analysis of $^{218}Po^{+}$ interaction with trace gases in Air

The "reaction" of $^{218}Po^{+}$ with trace gases can be characterized in terms of equilibrium reaction constant, K_{eq} because of the expectation that ^{218}Po clusters contain volatile components in a dynamic balance with the surrounding. On knowing K_{eq}, the chemical composition of the prevalent cluster aerosol can be estimated; and more importantly, the mechanism leading to the chemical and physical transformations of the radon progeny ions following their production will be better understood.

The mechanism of clustering of organic compound around a polonium ion in an environment containing water as well as organic compound was investigated. The organic molecule can either add to bare Po ion (association) or substitute a water molecule (switching) in an hydrated Po ion - See equation (4.11). The common believe is that Po ions become rapidly hydrated with water molecules and that the substitution of water molecule by organic molecule is possible. However, we observed earlier that "association" interaction seems to be more dominant

than the "switching" interaction. This is investigated further using 2-butanol.

If the switching reaction dominates, the interaction of polonium with 2-butanol in purified air (4%) should result in a reaction similar to (4.11). Therefore, replacing methanol in equation (4.11) with 2-butanol and assuming that the $[Po(H_2O)_x^+]$ remains constant with time, equal rates of formation and loss, it then follows from equation(4.11) that:

$$\frac{d[Po(H_2O)_x^+]}{dt} = -k_f[Po(H_2O)_x^+][C_4H_9OH]^y + k_r[Po(H_2O)_{x-y}(C_4H_9OH)_y][H_2O]^y \qquad (4.13)$$

where the bracket [] denotes concentration, k_f and k_r are the forward and reverse reaction rate constants. and t is the time.

Defining equilibrium constant, $K_{eq}=k_f/k_r$, and re-arranging equation (4.8) gives:

$$K_{eq} = \frac{k_f}{k_r} = \frac{[Po(H_2O)_{x-y}(C_4H_9OH)_y][H_2O]^y}{[Po(H_2O)_{x-y}][(C_4H_9OH)]^y} \qquad (4.14)$$

and a plot of $\ln([(Po(H_2O)_{x-y}(C_4H_9OH)]/[Po(H_2O)_{x-y}])$ against $\ln([C_4H_9OH]/[H_2O])$ should be a straight line with slope given by y and an intercept of K_{eq}. The plot is shown with the regression line in Figure 4.17. The values on the vertical axis is the ratio of the counts of Po-butanol cluster to the Po-water cluster while on the horizontal axis is the concentration ratio of the organic to that of water vapor (ppmv). The estimated water vapor concentration in the air used in this experiment is about 800ppmv. The regression coefficients, y and K_{eq} , are $2.196 \times 10^{-2} \pm 3.385 \times 10^{-2}$ and $1.936 \times 10^{-1} \pm 3.248 \times 10^{-1}$ with the correlation coefficient, R^2, of 0.564. Since y can only take on integer values, its value is approximated to zero which confirms that the switching reaction (equation 4.11) is unlikely. A similar analysis for methanol produced a y that is close to zero.

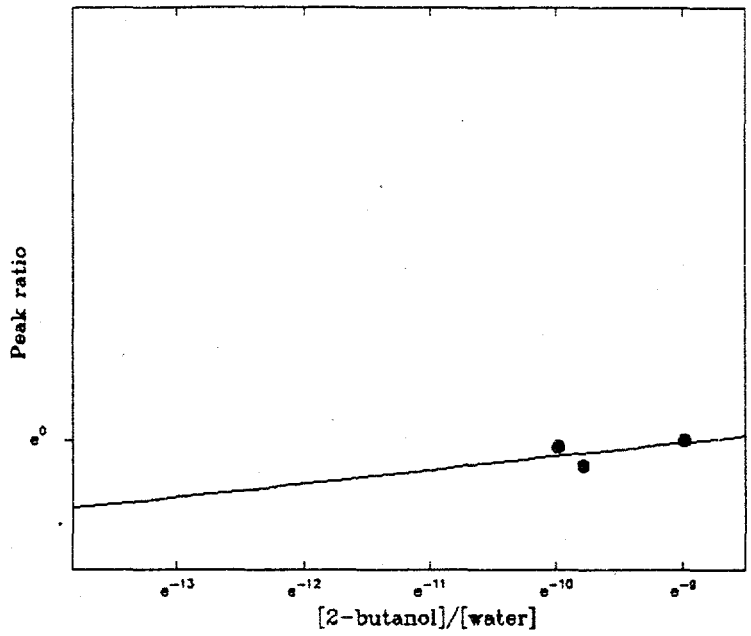

Figure 4.17: Plot of peak ratio against concentration ratio

4.4. Summary Remarks

The results obtained from the analysis of experimental data were presented and discussed in this chapter. In N_2 gas, it was observed that the size of the cluster aerosol formed in nitrogen gas is determined by the structural configuration of the trace volatile organic compound. In O_2, most of the charged particles are neutralized, thereby making clustering of contaminant species seemingly impossible. The cluster properties in Helium gas was found to be qualitatively the same as in N_2, despite the relatively high cluster-to-gas mass ratio in helium. However, in purified air with about 4% relative humidity, the particle size seems to be constant, irrespective of the structural configuration of the species and the increased neutralization observed in O_2 gas was conspicuously absent. The estimated cluster sizes in air with trace VOC species agreed fairly well with those from Thomson equation. However, the estimated cluster sizes in humid air did not agree with those from Thomson equation but they agreed with the results of Strydom *et al.* (1990). In support gases with trace VOC, the organic molecule will associate with a bare Po ion rather than substitute for water molecule in an hydrated Po ion.

Chapter
FIVE

FURTHER CHARACTERIZATION OF SYSTEM PERFORMANCE WITH TEST AEROSOL.

The reason(s) for the non-monotonic response of the system to the aerosol formed in the presence of volatile organic compounds (VOCs) need to be clarified. The clarification is necessary in order to determine whether the system response curve is always non-monotonic to polydispersed aerosol or it is only unique to VOC aerosol due to their volatility in the low pressure of the detector region.

To achieve this objective, particles that can be detected by existing particle size measuring devices were generated using a natural gas burner and the sizes distribution were measured by an electrostatic classifier(EC) and a ultrafine condensation particle counter(UCPC). The particles were made radioactive by mixing with radon progeny, and subsequently sampled with the impactor system.

Natural gas and propane are widely used as fuels for cooking and heating. Unlike cigarette smoke, particles from these two sources are in the < 30 nm range (Li and Hopke, 1993) and these particles are commonly found in non-smoking environment (Tu and Knutson, 1988) because cooking activities are closely related to our daily life.

5.1. Experimental System

The experimental system used here is as shown schematically in Figure 5.1. It is a modification of the one described in chapter 3. Therefore, only the modified parts will be described in detail in this section.

The test aerosol were generated by a gas burner placed at the bottom of a 55 gallon barrel. Part of the exiting aerosol from the chamber was subsequently sampled with a Scanning Mobility Particle Spectrometer (SMPS), tandem combination of EC and UCPC, in order to determine the particle size distribution. The rest of the aerosol was pumped into the attachment/radon chamber where the particles were mixed with the 200 cm^3 min^{-1} radon-laden

nitrogen gas and 1 liter min^{-1} of particle-free compressed air.

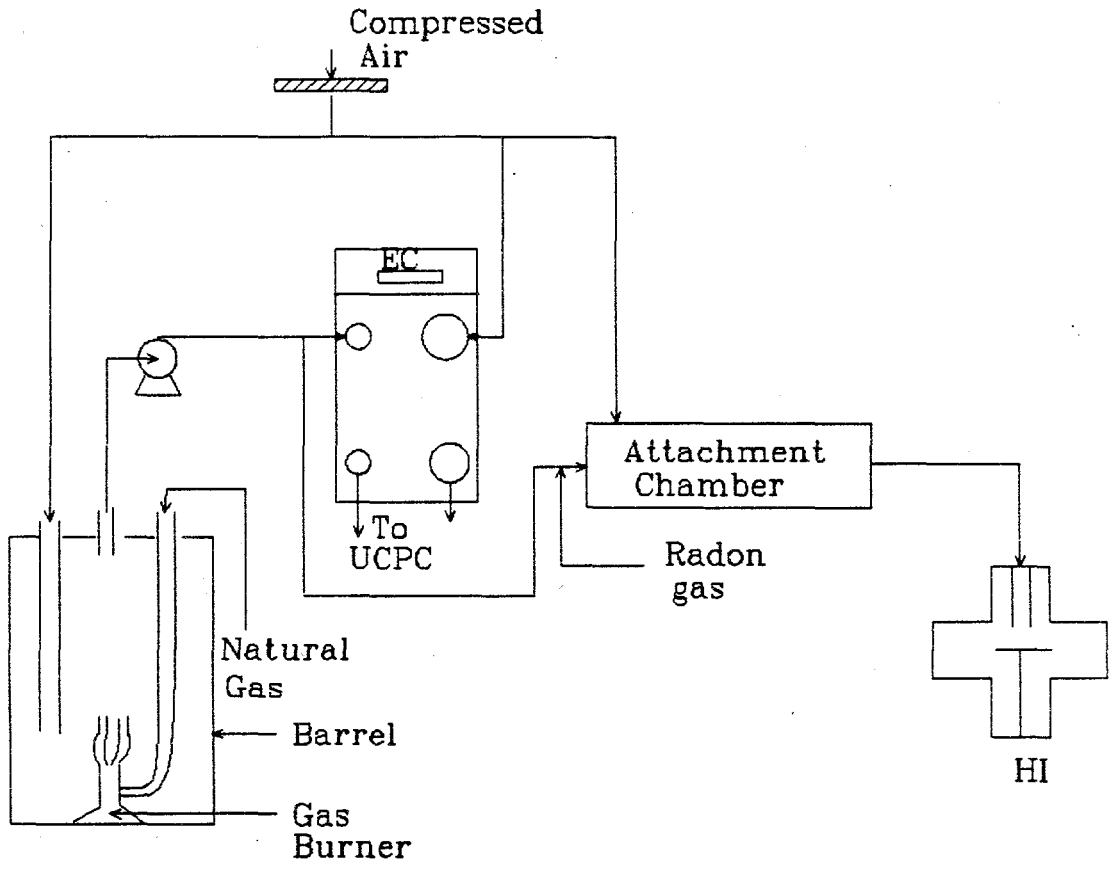

Figure 5.1: System for generating, radiolabeling, and sampling of gas burner particles.

In the chamber, the radon progeny attached to the gas burner particles as a result of the kinetic collisions between them. When a radon progeny travels in air containing aerosol particles, it has a chance to collide and stick onto the particle surface, thereby making the particle radioactive. The probability that the atom will stick on the surface of the particle, when kinetic collision occurs, is defined as the sticking coefficient. The attachment mechanism can be described either by diffusion or kinetic theory. For aerosol particles with diameter greater than 1

mm, the attachment is determined by pure diffusion while pure kinetic theory of gases controlled the attachment to particles with diameters less than 0.1 mm (Porstendörfer *et al.*, 1979). Consequently, the attachment coefficient/rate has been found to be linearly dependent on particle size distribution and particle concentration.

The radiolabeled particles were then sampled with both the HI system and UCPC for 2 minutes and the counting continued for 10 minutes thereafter. The sampling was repeated for various nozzle-to-plate distance, L and as usual, the plot of particle counts against L were made as presented in the section for results and discussion.

In order to prevent damage to the active surface of the PIPS detector of the HI by the impacting particles, the detector was covered with an aluminized mylar ($\sim$ 1 μm thick) and held in place with a cir-clips. By penetrating the mylar, the energy of the alpha particles emitted as a result of decay of ^{218}Po and ^{214}Pb attached to the collected particles is attenuated; thereby causing the ^{218}Po and ^{214}Pb peaks to shift and broaden to lower energies. This low energy tailing leads to certain amount of ^{214}Pb counts in the range of ^{218}Po peak. Because it takes about three hours to decay completely, a new mylar was used for every measurement in order to prevent ^{214}Pb tailing interference from previous measurement.

5.1.1 Differential Mobility Analyzer

The DMA used in this study is the TSI Model 3071 and it's design features are shown in Figure 5.2 It is a commercial unit based on the design of Knutson and Whitby (1975a & b). Polydisperse aerosol are first passed through a bipolar charging region produced by a 2 mCi ^{85}Kr source.

In the neutralizer, the particles quickly reach a state of equilibrium, in which the particles carry a bipolar charge distribution. Previously, the charge distribution was thought to be described by Boltzman equilibrium charge distribution. The Boltzmann charge distribution is symmetrical around zero; that is, the fraction of particles with n positive charges equals the fraction with n negative charges.

The charge distribution for submicrometer particles in air has been investigated by several authors (Hussin *et al.* 1983; Adachi *et al.* 1985). It was found that the deviations between the measured fractions and the calculated fractions obtained from Boltzman's law increased with decreasing particle diameters. This means that the fraction of positively charged particles is different from the fraction of negatively charged particles. Table 5.1 lists the fractions of

particles in air that carry +1, +2, +3, +4, +5 and +6 charge units.

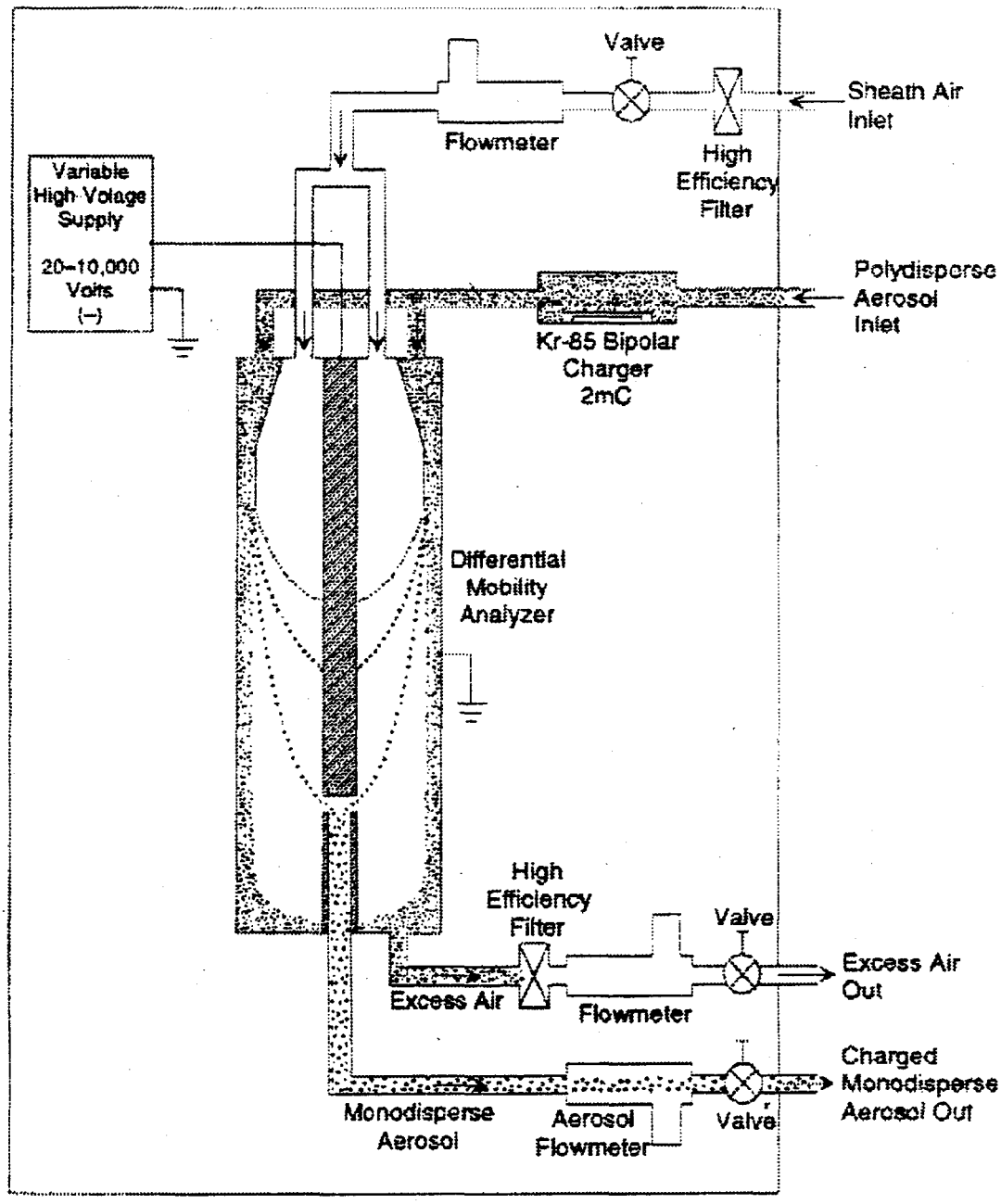

Figure 5.2: Flow Schematic for the Electrostatic Classifier

Table 5.1 Fraction of total particle concentration that carries +1, +2, +3, +4, +5 and +6 elementary charges.

Particle Diameter (μm)	Fraction of Total Particle Concentration That Carries This Number (1-6) of Positive Charges					
	+1	+2	+3	+4	+5	+6
0.010	0.0411	0.00	0.00	0.00	0.00	0.00
0.021	0.0866	0.00012	0.00	0.00	0.00	0.00
0.031	0.1241	0.0011	0.00	0.00	0.00	0.00
0.053	0.1748	0.0078	0.00	0.00	0.00	0.00
0.059	0.1841	0.0105	0.00	0.00	0.00	0.00
0.074	0.2000	0.0180	0.0005	0.00	0.00	0.00
0.083	0.2064	0.0225	0.00089	0.00	0.00	0.00
0.093	0.2113	0.0279	0.0016	0.00	0.00	0.00
0.104	0.2148	0.0339	0.0028	0.00	0.00	0.00
0.193	0.2059	0.0700	0.0200	0.0022	0.00014	0.00
0.291	0.1804	0.0871	0.0400	0.0088	0.0013	0.00013
0.391	0.1580	0.0910	0.0533	0.0168	0.0040	0.0007
0.457	0.1467	0.0902	0.0593	0.0217	0.0062	0.0014
0.535	0.1356	0.0879	0.0641	0.0266	0.0089	0.0024
0.631	0.1251	0.0844	0.0678	0.0315	0.0122	0.0040
0.746	0.1158	0.0806	0.0701	0.0360	0.0158	0.0060
0.886	0.1081	0.0770	0.0701	0.0400	0.0194	0.0084
1.056	0.1023	0.0749	0.0703	0.0422	0.0277	0.0110

To separate this charged aerosol into single particle size fractions, the aerosol is passed through the outer layer of the column from a small gap while particle-free sheath air enters the inner layer of the column. The aerosol surrounds the inner core of sheath air, and both streams flow laminarly down the annulus with no mixing of the two streams. The inner cylinder, the collector rod, is maintained at a controlled voltage, while the outer cylinder is electrically grounded. This creates an electric field between the two cylinders. As the voltage on the central electrode is increased, the positively charged particles of increasing mobility pass, under the influence of an electrical force, through an exit slit. Only those particles with electrical mobilities within a narrow range are able to follow exactly the critical trajectory and enter this exit slit, thereby providing an essentially monodisperse aerosol. Those particles with larger electrical mobilities will hit the central rod before the exit slit, and those with smaller electrical mobilities will miss the exit slit and come out with the excess air.

Although the exiting aerosol from DMA will be contaminated by multiply charged

particles for particles greater than 60 nm, useful particles can be produced in the range of 5 to 100 nm.

Aerosol Electrical Mobility

An aerosol particle in an electric field, E, carrying n electric charges experiences an electrical force, causing it to move through the gas in which it is suspended. It very quickly reaches its terminal velocity, v. The resulting drag force on the particle is given by Stokes law and can be equated to the electrical force to determine the electrical mobility of a particle. The electrical mobility, Z_p, is defined as follows:

$$Z_p = \frac{neC_c}{3\pi\mu d_p} \tag{5.1}$$

where n is the number of elementary charges on the particle; e is the elementary charge (1.6 x 10^{-19} Coulomb) and μ is the gas viscosity (dyne s cm^{-2}) poise. The other parameters are as previously defined.

The range of particle diameters removed from the electrostatic classifier depend also on the geometry and flowrates of the classifier. Knutson (1975) determined the relationship between the particle electrical mobility and the classifier parameters. The relationship is given as: :

$$Z_p = \frac{q_{sh}}{2\pi VL} \ln\left(\frac{r_2}{r_1}\right) \tag{5.2}$$

where q_{sh} is the sheath air flowrate (equal to excess air flowrate); r_2 is the outer radius of the annular space; r_1 is the inner radius of the annular space; V is the average voltage on the inner collector rod and L is the length between the exit slit and polydisperse aerosol inlet.

Combining equations (5.1) and (5.2) gives:

$$\frac{d_p}{C_c} = \frac{2neVL}{3\mu q_{sh} \ln\left(\frac{r_2}{r_1}\right)} \qquad (5.3)$$

This equation relates the particle diameter to collector rod voltage, number of charges on the particle, classifier flowrate and geometry.

5.2. Results and Discussion

The measured size distributions of the gas burner particles exiting the barrel is as shown in Figure 5.3.

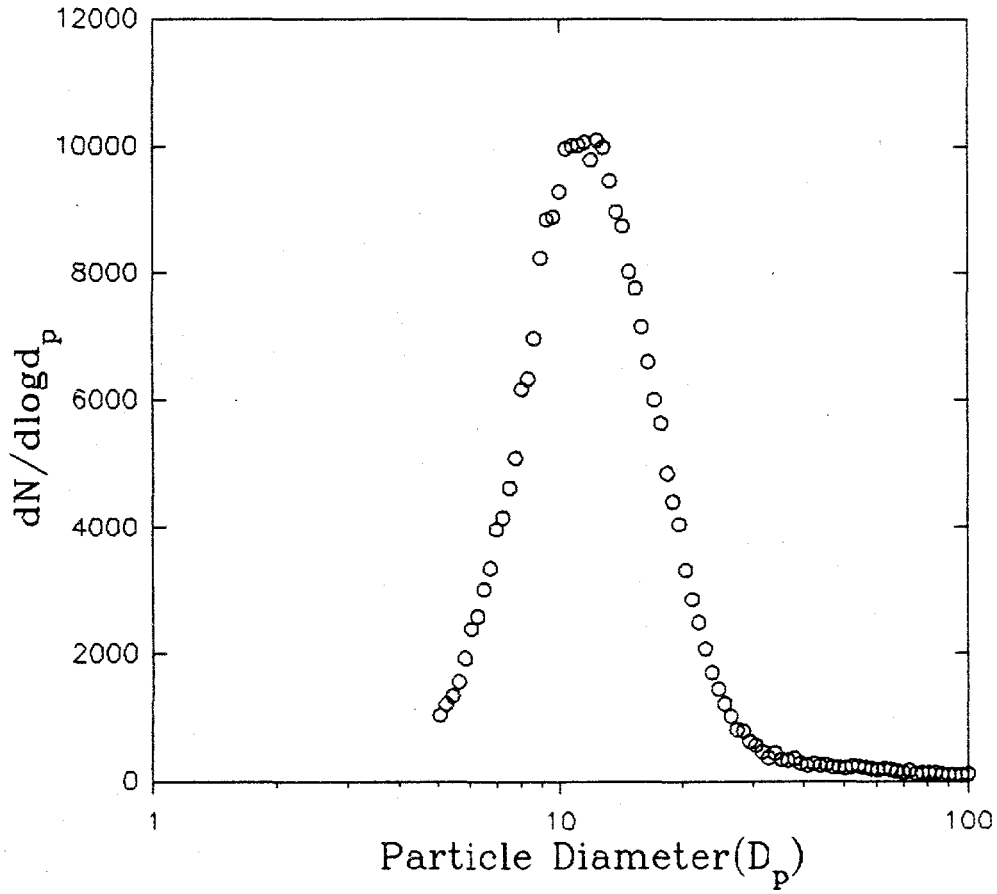

Figure 5.3: The size distribution of the gas burner particles

The distribution was measured with EC operated at 20 LPM for sheath and excess air and 2

LPM for monodisperse aerosol flow . In the figure, the number size distribution is in terms of fractional number per unit log d_p and It is lognormal with a geometric mean of about 13 nm and σ_g of 1.6.

Figure 5.4 show the impactor response curve to the aerosol which size distribution is shown in Figure 5.3.

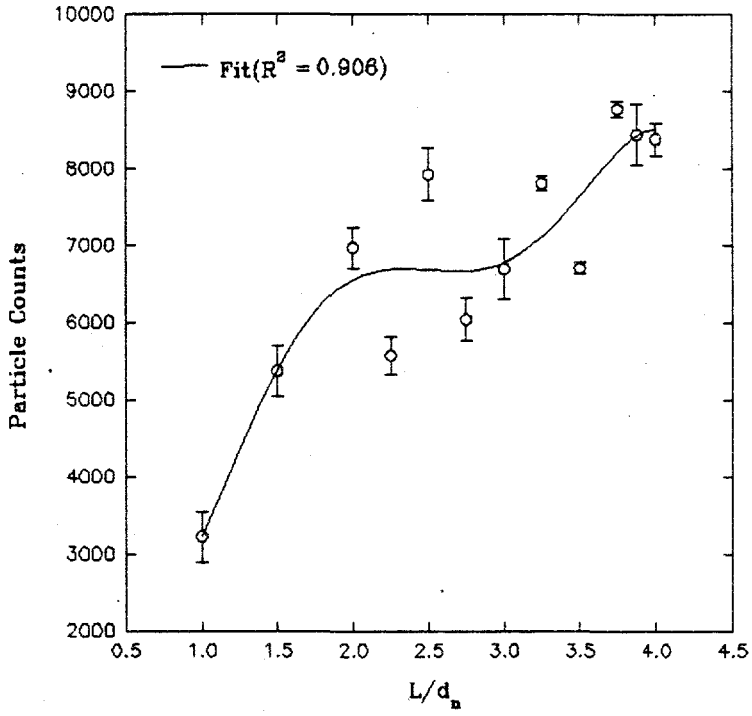

Figure 5.4: The fitted response curve to the experimental data points.

In Figure 5.4, there are two distinct broad step sizes. The steps are rather broad because of the broad nature of the distribution. The steps in the ranges $1.0 < L/d_n < 2$ and $3.0 < L/d_n < 4.0$ corresponds to particles with aerodynamic diameters of 18 nm and 7 nm, respectively. The 7 nm particles are the unattached radon progeny present in the sampled aerosol while the 18 nm particles are supposedly the gas burner particles. This clearly show that the aerosol present in the attachment chamber was bimodal. The impactor's monotonic response to these bimodal aerosol seems to confirm earlier conclusion regarding the bumps observed in the response curves for the aerosol in support gas with trace VOCs (Chapter 4). The non-monotonic response was adduced to the evaporation of the clustered VOCs in the low pressure region of the detector.

To determine the density of the soot, the mobility size of the same soot aerosol was measured with a modified form of circular electrical mobility spectrometer (Mesbah *et al.*,1993). The size was measured to be 13 nm. Using the relation between the aerodynamic and physical diameters discussed in chapter 3, the particle density was estimated to be 1.38 g cm^{-3}. It is good to note that this estimated density is inconsistent with the density of carbon of 2 g cm^{-3} because soot have a porosity. This will reduce the density considerably. A range of density values of 1.4 to 1.8, which are not well grounded, has been reported in the literature (Sarofim, 1995).

An attempt was also made to measure mono-mobility particle selected by a DMA. The DMA voltage was set to 0.082 V to select particles with diameter corresponding to the highest peak in the size distribution (Figure 5.3). However, the exiting particles concentration was about 200 particle/cm^3 which was too low to collect detectable number of particles over a reasonable period of time. For particles of this size, the attachment rate is low and thus, most are not attached to radon progeny, thereby making them undetectable. Despite the fact that the analysis of the particle deposit using Computer Controlled Scanning Electron Microscope (CCSEM) showed a highly concentrated deposit, there was little or no count at all. Consequently, the experiment was discontinued. For particles with size less than 10 nm, attachment of radon progeny seems to be not better than charging them, which further reinforces the fact that the system developed in this work is good only for the analysis of naturally radioactive aerosol particles and for aerosol having a high fraction of radiolabeled particles.

5.3. Summary Remarks

In this chapter, the impactor performance was tested with an aerosol that was a mixture of gas burner particles and radon progeny. The impactor was able to resolve the bimodal distribution. The stair step pattern was exhibited for these bimodal aerosol. Also, it was established that the system should be used for aerosol with sufficient fraction of radioactive particles in order to collect a measurable activity on the detector. This was found to be particularly important for the case when the aerosol particles has to undergo attachment process in order to detect the particles.

Chapter
SIX

CONCLUSIONS AND RECOMMENDATIONS

The growing importance of ultrafine particles in aerosol science has led to the development of several instrumentation for measuring their size distribution in a given aerosol. These existing instruments utilizes either the electrical or diffusive properties of the particle. Because of the inherent limitations of these method, the resolution of these instruments are limited. Therefore, a system for aerodynamically sizing sub-nanosize radioactive particles using supersonic jets have been developed and evaluated with radon particles generated under well controlled laboratory conditions. From the ensuing experimental results, the following conclusions can be drawn.

First and Foremost, the resolution of the system was found to be fairly good, despite the fact that there was considerable diffusional deposition of the sub-nanometer cluster and it was established that the radon progeny clusters would grow in an environment containing water and/or VOC.

In pure and inert gases, the initial properties of ^{218}Po were the same in helium, nitrogen and purified air, but a relatively high neutralization rate of the charged ion was observed in oxygen gas. As a result, the response curves for the cluster aerosol has the characteristic slanted -Z shape, a high tail end.

For support gases with water vapor, it was found that the radon cluster would grow from about 7 nm (RH~0%) to about 10 nm (RH~15%) and remained constant thereafter. The trend in the result also correspond with that obtained from Thomson equation.

For nitrogen gas with trace VOC, unlike the case for water vapor, the cluster aerosol was found to be bimodal. As a result, the response curves for this cluster aerosol should have a stair step pattern. However, the response curves with double humps were obtained. The presence of humps instead of stair step pattern was adduced to the evaporation of clustered species in the low pressure near the detector region which was supported by the results of the measurements made for gas burners particles. The stair step pattern was evident in the response curve for the

bimodal distribution of a combination of gas burner and radon progeny aerosols.

Regarding the cluster size, it increased with hydrocarbon chain length which is determined by the structural configuration. In purified air, however, the cluster size remained the same irrespective of the organic compound present and there was no noticeable neutralization of the charged ions by oxygen, which was the case in pure oxygen. This observation suggested the formation of $Po^{+}O_2^{-}$, a dipole, instead of PoO_2^{+} in air.

In the presence of both water vapor and VOCs in the support gas, the organic molecule will associate with a bare Po ion rather than substitute for water molecule in an hydrated Po ion. Thus, the interaction is by "association" rather than by "switching" as proposed by Chu and Hopke (1988). This was corroborated by the results of the thermodynamic analysis of the interaction of radon progeny with trace gases. Consequently, the relative number concentration of the dominant cluster sizes is determined by the relative VOC-water concentration.

For the system developed in this work to be used for more precise work two problems have to be addressed. First, an instrumentation for monitoring on-line the number of particles/cluster entering the particle during a given run has to be developed. This will allow the fraction of the entering particle that are collected to be computed. The existing particle counting instruments, UCPC and DMA, can not detect sub-nanometer particles. Secondly, a new method to generate particles/cluster of standard sizes has to be devised. The cluster of known sizes could then be used to calibrate the system.

Above all, the major disadvantage of the use of the HI system for sampling in real environment is the relatively long time it takes to do particle size spectroscopy of a given aerosol. Thus, it is impractical to use in an environment with a low particle concentration.

REFERENCES

Adachi, M., K. Okuyama and Kousaka, Y. (1985), Electrical Neutralization of Charged Aerosol Particles by Bipolar Ions, *Journal of Chemical Engineering*, Japan, 16:229.

Anselm, A., Gebhart, J., Heyder, J. and Ferron, G. (1986) Human Inhalation of Hygroscopic Particles in the Respiratory Tract, Aerosols: Formation and Reactivity, G. Isreal ed., Pergamon Press Ltd., Oxford, 252-255.

Ashenas, H. and Sherman, F. S. (1966) Rarefied Gas Dynamics (Edited by de Leeuw, J. H.), Vol. II, p. 84. Academic Press. New York.

Baron, P. A. and Willeke, K. (1993), Aerosol Measurement: Principles Techniques and Applications, Van Nostrand Reinhold, New York.

Berglund, B. (1986), Assessment of Discomfort and Irritation from the Indoor Air. Proceedings IAQ' 86: Managing Indoor Air for Health and Energy Conservation, ASHRAE, Atlanta, GA., pp. 138-149.

Berglund. B., Berglund, U., and Lindvall, T. (1986). In Proceedings IAQ '86: Managing Indoor Air for Health and Energy Conservation, ASHRAE, Atlanta, GA, pp 138-149.

Beylich, A. E. (1981) Rarefied Gas Dynamics (Edited by Fisher, S. S.), Part II, p. 710 AIAA, New York.

Birchall, A and James, A. C., *Radiat. Protect. Dosimetry*, 53: 1-4, 133-140.

Biswas P and Flagan, R. E. (1984), High Velocity Inertial Impactors, *Envir. Sci. and Technol.*, 18:611-616

Brown S. K., Sim, M. R., Abramson, M. J. and C. N. Gray. (1994) Concentrations of Volatile Organic Compounds in Indoor air - a review, *Indoor Air*, 4: 123-134

Brun, R. J., Lewis, W., Perkins, P. J., and Serafini, J.S. (1955). NACA Rep. 1215

Busigin, A., Van der Vooren, A. W. and Phillips, C. R. (1980) A Technique for Calculation of Aerosol Particle Size Distributions from Indirect Measurements, *J. Aerosol Sci.* 11:359-366

Castleman, A. W. Jr, (1982). Experimental Studies of Ion Clustering Relationship to Aerosol Formation Processes and some Atmospheric Implications. *J. Aerosol Sci.* 13, 73.

Castleman, A. W. (1991), Consideration of the Chemistry of Radon Progeny, *Environ. Sci. and Technol.*, 25, 730-735.

Castleman, A. W. and Tang, I. N. (1972), Role of Small Clusters in Nucleation about Ions, *J. Chem. Phys.* 57: 3629.

Chamberlain, A. C., and Dyson, E. D. (1956). The Dose to the Trachea and Bronchii from the Decay Products of Radon and Thoron. *Brit. J. radiol.* 29: 317-325.

Chan, T. L. and Lippmann, M. (1980), Experimental Measurements and Empirical Modeling of Regional Deposition of Inhaled Particles in Humans, *Amer. Ind. Hyg. Assoc. J.* 41:399-409.

Chan, L. Y. and Mohnen, V. A. (1980). Ion Nucleation Theory, *J. Atmos. Sci.* 37:2323-2331

Chang, P. S., Brock, J. R. and Trachtenberg, I.,(1993) A Theoretical Investigation of Low Pressure Particle Impaction in a Highly Underexpanded Sonic Impinging Slit Jet, *J. Aerosol Sci.*, 24: 31-44.

Chen, Y. L. (1988) Aerosol Jet Etching, Ph.D. dissertation. University of Texas at Austin

Chen, Y. L., Brock, J. R. and Trachtenberg, I. (1987) *Appl. Phys. Lett.* 51, 2203.

Chu, K. D., and Hopke, P. K. (1988), Neutralization Kinetics for Polonium-218, *Environ. Sci. and Technol.* 22: 711-717.

Courant, R., and Friedrichs, K. O. (1957), Superosnic Flow and Shock Waves, Interscience, New York, 1957.

CRC Handbook of chemistry and Physics, 70th ed. (1989). R. C. Weast, D. R. Lide, M. J. Astle, and W. H. Beyer, eds. CRC Press, Inc., Boca Raton, FL.

Crowe, C. T. (1967), Drag Coefficient of Particles in a Rocket, *AIAA Journal*, 5:1021-1022

Daisey, J. M. and Hopke, P. K.,(1993) Potential for Ion-induced Nucleation of Volatile Organic Compounds by Radon Decay in Indoor Environments, *Aerosol Sci. and Technol.* 19: 80-93

Davies, C. N. (1945) Definitive Equations for the Fluid Resistance of Spheres, *Proc. Phys. Soc.* 57(4):259-270

Davies, C. N. and Aylward, M. (1951), The Trajectories of Heavy, Solid Particles in a Jet of Ideal Fluid Impinging on a Plate. *Proc. Phys. Soc.* (Lond.) B64:689

de la Mora, J., Rao, N. and McMurry, P. H. (1990b), Inertia Impaction of Fine Particles at Moderate Reynolds Numbers and in the Transonic Regime with a Thin Plate Orifice Nozzle. *J. Aerosol Sci.* 21: 889.

de la Mora, J., Hering, S. V., Rao, N. and McMurry, P. H.(1990a), Hypersonic Impaction of Ultrafine Particles, *J. Aerosol Sci.* 21, 169

Dorsch, R. G., Super, P. G., and Kadlow, C. F. (1955) NACA Tech. Note 3587.

Dupeyrat, G. (1981) Rarefied Gas Dynamics (Edited by Fisher, S. S.), Part II, p. 812. AIAA, New York.

Dupeyrat, G. and Devillers, J. F. (1978) C. R. Acad. Sc. Paris 287, 101

Egan, M. J. and Nixon, W. (1989) On the Relationship Between Experimental Data for Total Deposition and Model Calculations - Part II: Application to fine Particle Deposition in the Respiratory Tract, *J. Aerosol Sci.* 20: 149-156.

Environmental Protection Agency (EPA), 1992, Technical Support Document for 1992 Citizen's Guide to Radon, Report No. EPA 400-R-92-001, U. S. Environmental Protection Agency, Washington, DC.

Ferron, G. A. (1977), The Size of Soluble Aerosol Particles as a Function of the Humidity of the Air: Application to the Human Respiratory Tract, *J. Aerosol Sci.*, 8: 251-267.

Flagan, R. E (1982), Compressible Flow Inertia Impactors, *J. Colloid Interface Sci.*, 87:291-299.

Forney, L. J. and McGregor, W. K. (1987), Partcle Sampling in Supersonic Streams with a Thin Walled Cylindrical Probe. *AIAA j.* 25: 1100-1104

Frey G., Hopke, P. K. and Stukel, J. J. (1981), The Effects of Trace Gases and Water Vapor on the Diffusion Coefficient of Po-218. *Science.* 211: 480-481.

Friedlander, S. K.(1977), Smoke, Dust and Haze, John Wiley and Sons, Inc., New York.

Fukushima, K., Yamada, I. and Takagi, T. (1985), Characteristics of TiO_2 Films Deposited by a Reactive Ionized Beam, *J. appl. Phys.* 58, 4146

Goldstein, S. D. and Hopke, P. K. (1985), Environmental Neutralization Po-218., *Environ Sci. and Technol.*, 19:146-150.

Hammon, H. G., Ernat, K., Gaskill, J. R., Newton, J. C., and Morris, C. J. (1975). Report No. UCRL-51818, TID-4500, UC-41, May 29, 1975, Lawrence Livermore Laboratory, Livermore Laboratory, Livermore, CA.

Hawrynski, M. J. (1984), The Theory of Clusters. In H. Stoker (ed.) Proc. Int. Conf. and occupational radiation and safety in mining, Canadian nuclear assoc. Toronto, Canada p. 56.

He F. and Hopke, P. K. (1995), Ion-induced Binary Nucleation of Sulphuric Acid and Water, *Aerosol Sci. and Tech.*(in press)

Hering, S. V. and Stolzenburg, M. R.(1995), On-line Determination of Particle Size and Density in the Nanometer Size Range, *Aerosol Sci. and Technol.*, (in press).

Hering, S. V. and Friedlander, S. K., Collins, J. J. and Richards, L. W. (1979), Design and Evaluation of a New Low-pressure Impactors, *Environ. Sci. Technol.* 13: 184-188

Hopper, R., Levy, R. A., Rankin, R. C., Boyd, M. A. (1991). In: National ambient radon study. Proceedings of the 1991 International symposium on Radon and Radon reduction technology. Research Triangle Park, NC.

Hussein, A. H. G. Schcibel, K. H. Becker, and J. Porstendorfer (1983), Bipolar Diffusion Charging of Aerosol Particles 1: Experimental results within the diameter range of 4 - 30 nm., *J. Aerosol Sci.*, 14: 671.

Ishii, R., Umeda, Y. and Yuhi, M. (1989), Numerical Analysis of Gas-Particle Flows, *J. Fluid Mech.* 203: 473.

Isreal, R. and Rosner, D. E. (1983), Use of a Generalized Stokes Number to Determine the Aerodynamic Capture Efficiency of non-Stokesian Particles from a Compressible Gas Flow, *Aerosol Sci. and Tech.*, 2:45-51.

Jurcik, B. J., Brook, J. R., and Trachtemberg, I. (1989), A Study of Low Pressure Particle Impaction Processes, *Aerosol Sci and Technol.* 20: 707-711.

Kalghtgi, G. T. and Hünt, B. L. (1976), Aeronaut. Q. 27, 169.

Kauppinen, E. I. and and Hillamo, R. E. (1989), Modification of the University of Washington in-Stack Impactor, *J. Aerosol Sci.* 20: 813-827.

Keese, R. G., and Castleman, A. W. Jr. (1989), The Properties of Organic Compounds in Molecular Clusters, *Aerosol Sci. and Technol.*, 10: 352-357

Knutson, E. O. and Whitby, K. T.(1975a), Aerosol Classification by Electric Mobility: Apparatus, Theory and Applications *J. Aerosol Sci.* 6: 443 - 450.

Knutson, E. O. and Whitby, K. T. (1975b), Accurate Measurement of Aerosol Electric Mobility Moments, *J. Aerosol Sci.* 6: 453-460

Koga J. Yamada H. and Matsumoto, S. (1989), FLow in Low Pressure Impactor and Collection Efficiency of Particless, *J. of Nuclear Sci. and Tech.* 26, 10, 973-976.

Leipmann, H. W., and Roshko, A. (1957) Elements of Gasdynamics. John Wiley, New York.

Leong, K. H., Hopke, P. K., Stukel, J. J., and Wang, H. C., (1983), Radiolytic Condensation Nuclei in Aerosol Neutralizer. *J. Aerosol Sci.* 14: 23-27.

Li, W. and Hopke, P. K. (1993), Initial Size Distribution and Hygroscopicity of Indoor Combustion Aerosol Particles, *Aerosol Sci. and Technol.*, 19: 305-316.

Lind, S. C. (1961). Radiation Chemistry of Gases. American Chemical Society Monograph Series, Reinhold Publishing, New York.

Lodge, J. P. and Chan, T. L. (1986), Cascade Impactor Sampling and Data Analysis, A publication of the American Industrial Hygiene Association.

Lohner R., Morgan, K. Peraire, J. and Vahdati, M. (1987), Finite Element Flux-corrected Transport (FEM-FCT) for the Euler and Navier-Stokes Equations. *Int. J. Num. Meth. Fluids* 7, 1093.

Maple, V. A. and Liu, B. Y. H. (1974), Characteristics of Laminar Jets Impactors, *Environ. Sci. Technol.* 3: 648-654.

Maple, V. A., and Willeke, K. (1979), Inertial Impactor: In Aerosol Measurement (ed. D.A. Lundgren et al.), pp. 90-106, Univ. of Florida, Gainsville.

Marcinowski, F., Lugas, R. and Yeager, W. M.(1993), National and Regional Distribution of Airborne Radon Concentration in US homes., *Health Physics*, 66(6): 699-706.

Marple, V. A., Liu, B. Y. H. and Whitby, K. T. (1974), Fluid Mechanics of the laminar flow Aerosol Impactors, *J. Aerosol Sci.* 5:1-16.

Martonen, T. B., K. A. Bell, R. F. Phalen, Wilson,A. F. and Ho, A. (1982), Growth Rate Measurements and Deposition Modeling of Hygroscopic Particle Behavior in Human Tracheobrochial Models, Ann. Occup. Hyg. 26:93-108

May, K. T. (1945) The cascade impactor: an instrument for sampling coarse aerosols, *J. Sci. Instr.*, 22: 187-195

Mercer, T. T. and Stafford, R. G. (1969), Impaction from Round Jets, *Ann Occup. Hyg.*, 12:41-48.

Mesbah B., Bouland D., Pourprix M. and Renoux, A. (1993), Circular Electrical Mobility Spectrometer, *J. Aerosol Sci.* 24: S219.

Miguel, A. H. and Natusch, F. S. (1975). Diffusion cell for the preparation of dilute vapor concentrations. *Analytical Chemistry*. 47, 1705.

Nazaroff, W. W. and Nero, Jr. A. V. (1988), Radon and Its Decay Products in Indoor Air, John Wiley & Sons., New York.

Oh, J. J. and Kim, S. S.(1994), Particle deposition on a truncated cylinder in a supersonic flow at low pressure, *Aerosol Sci. and Technol.* 20: 375-384.

Olawoyin, O. O., Raunemaa, T. A. and Hopke, P. K. (1995), A system for aerodynamically sizing ultrafine particles, *Aerosol Sci. and Technol.*, 23: 121-129

Ounis H., Ahmadi G. and McLaughlin, B. (1990), Brownian Diffusion of Submicrometer particles in the viscous layer, *J. of Colloid and Interface Science* 143, 1:266-276.

Papoulis, A. (1965) Probability, Random variables and Stochastic processes, McGraw-Hill, New York.

Perrin, M., Margne, J. P., and Madeline, G. J. (1978). *J. Aerosol Sci.* 9: 429-433.

Porstendörfer, J. (1979), Experimental Determination of the Attachment Coefficients of Atoms and Ions on Monodisperse Aerosols, *J. Aerosol Sci.* 25: 219 - 263.

Porstendörfer, J. (1994), Properties and Behavior of Radon and Thoron and their Decay Products in the Air - Tutorial/Review, *J. Aerosol Sci.* 25: 219 - 263.

Raabe, O. G. (1969), Concerning the interactions that occur between radon decay products and aerosols, *Health Phys.* 17: 177-186.

Rader, D. J. (1990), Momentum Slip Correction Factor for Small Particles in Nine Common Gases, *J. Aerosol Sci.*, 21: 161-168

Raes, F. (1985), Description of the Properties of Unattached ^{218}Po and ^{212}Pb Particles by means of the Classical Theory of Cluster Formation, *Health Phys.*, 49: 1177-1187.

Ramamurthi, M., Strydom, R., and Hopke, P. K. (1993), Nanometer and Ultrafine Aerosols from Radon Analysis, *J. Aerosol Sci.* 11:333-337.

Ranz, W. E. and Wong, J. B. (1952), Impaction of Dust and Smoke Particles, *Ind. Eng. Chem.*, 44, 1371.

Richtmeyer, R. D. and Morton, K. W. (1967), Difference Methods in Initial Value Problems, Interscience, New York, 1967.

Sarofim, A. (1995) Personal communication

Sasse, A. G., Gadgil, A. J., and Nazaroff, W. W. (1994), On the Measurement of ^{218}Po Diffusivity using the Two-Filter Method. *J. Aerosol Sci.* 25: 689-697.

Schlesinger, R. B. and Lippmann, M. (1972) Particle Deposition in Casts of the Human Upper Tracheobrochial Tree, *Am. Ind. Hyg. Assoc.* J. 33:237-251

Serafini, J. S. (1954), Impingement of Water Droplets on Wedges and Double-Wedge Airfoils at Supersonic Speeds, NACA Reports 1159.

Shapiro, A. S. (1957) The Dynamics and Thermodynamics of Compressible Fluid Flow, Vol. I. Ronald Press, New York.

Sinnaeve, J. (1984), Opening Address, *Rad. Prot. Dos.* 7:13-14

Strydom, R., Leuschner, A. H. and Stoker, P. H. (1990)., A Mobility Spectrometer for Measurement of Initial Properties of ^{218}Po, *J. Aerosol Sci.* 21:859-873.

Su, Y. F., Cheng, Y. S., Newton, G. J., and Yeh, H. C. (1988). Experimental Measurements of Diffusion Coefficients and Calculated Sizes of ^{212}Pb Particles. *J. Aerosol Sci.* 19: 767-770.

Teshima, K. (1987) *Phys. Fluids* 30, 1899.

Thomas, J. W. and LeClare, P. C. (1970), A Study of the Two Filter Method for Radon-222 *Health Physics*. 18, 113.

Thomson, J. J. (1888). Application of Dynamics to Physics and Chemistry. Ist ed. Cambridge University Press.

Tu, K. W. and Knutson, E. O. (1988) Indoor-Outdoor Aerosol Measurement for two Residential buildings in New Jersey, *Aerosol Sci. and Technol.*, 9:71-82.

Vohra, K. G., Subba Ramu, M. C. and Muraleedharan, T. S. (1984)., An Experimental Study of the Role of Radon and its Daughter Product in the Conversion of Sulphur into Aerosol Particles in the Atmosphere. *Atmos. Environ*. 18: 1653-1656

Wang, H. C. and John, W. (1988) Characteristics of the Berner Impactor for Sampling Organic Ion, *Aerosol Sci. and Technol.*, 8: 157

Wilson, N. K. (1987) Indoor Air Level of Polynuclear Aromatic Hydrocarbons and related Compounds in Eight-Home Pilot Study. In proceedings of the 11th international symposium on polynuclear aromatic hydrocarbons, Gaithersburg, MD, 1987.

Yoon, S. C.(1992), Measurement of the Indoor Atmospheric Trace Gas on the ^{218}Po Mobility Spectrum by Alpha-Track Detector, Ph.D. Thesis, College Station, TX: Texas A&M University.

Yoon, S. C., Marlow, W. H. and Hopke, P. K. (1992), Measurement of SO_2 Effects on the ^{218}Po ion Mobility Spectrum by Alpha-Track Detection. *Health Phys*. 62(1): 57-57.

Appendix A

Relation between the d_{ae} and d_p in the free molecule regime

For a given particle the settling velocity, v_s, is:

$$v_s = \frac{\rho_p g d_p^2 C_c(d_p)}{18\mu} \qquad \textbf{(A-1)}$$

where g is the acceleration due to gravity and the other variables are as previously defined .

Similarly, for a unit density sphere having the same settling and aerodynamic properties as the given particle:

$$v_s = \frac{g d_{ae}^2 C(d_{ae})}{18\mu} \qquad \textbf{(A-2)}$$

where d_{ae} is the aerodynamic diameter

Equating (A-1) and (A-2) gives:

$$\rho_p = \frac{d_{ae}^2 C(d_{ae})}{d_p^2 C(d_p)} \qquad \textbf{(A-3)}$$

In the free molecule regime, it follows from equation 2.2 that:

$$\frac{C(d_{ae})}{C(d_p)} = \frac{d_p}{d_{ae}} \qquad \textbf{(A-4)}$$

Substituting equation A-4 in equation A-3 results:

$$d_{ae} = \rho_p d_p \qquad \textbf{(A-5)}$$